Chapter 4. 円盤銀河と楕円銀河の形成

4.1 円盤構造の形成

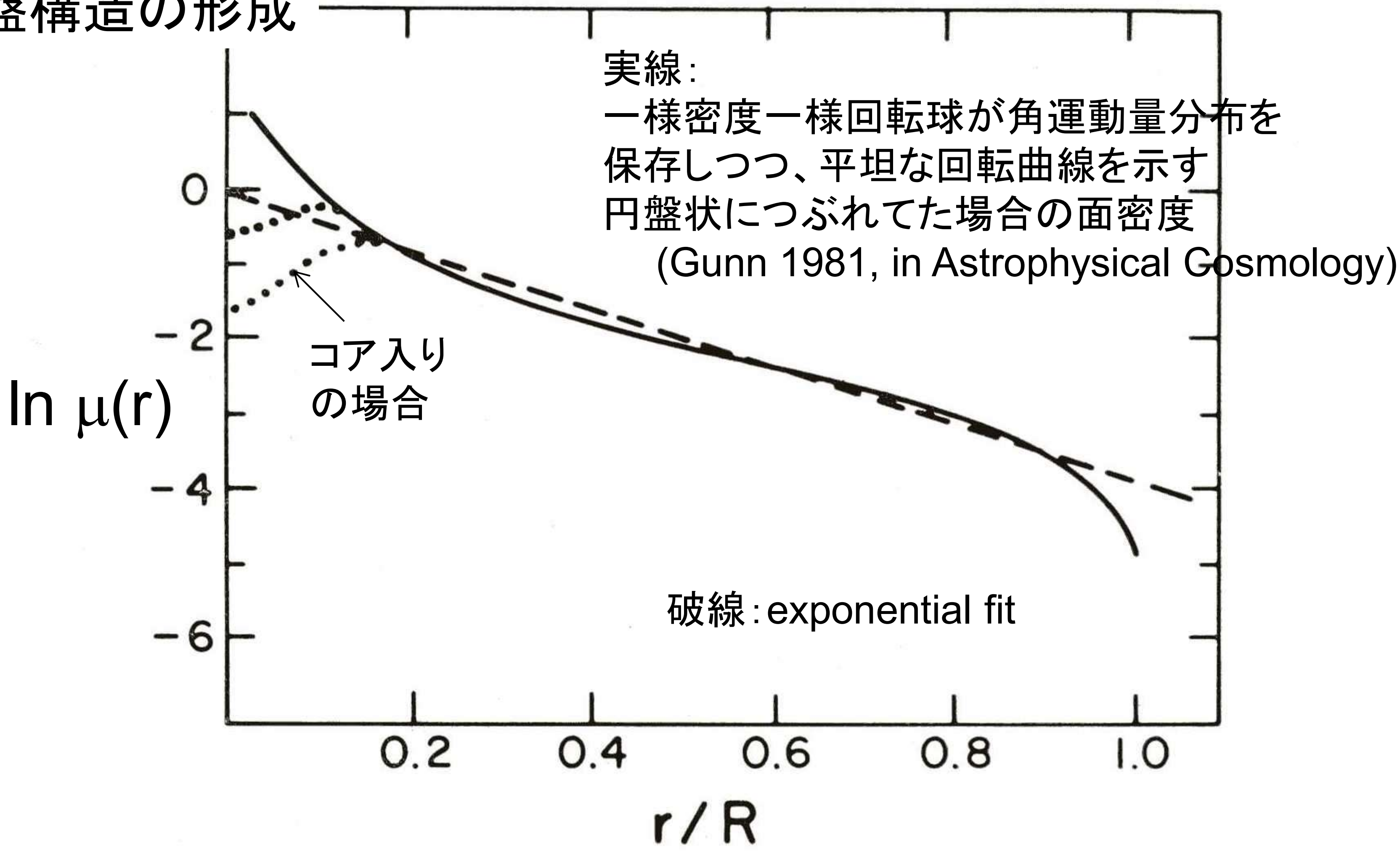

FIG. 7. The surface-density-radius relation for the angular momentum distribution of a uniformly rotating uniform sphere which rotates with constant circular velocity after collapse (solid line) and the same except for a small constant angular velocity core of radii 0.5 and 0.8 scale lengths (dotted lines). The dashed line is an exponential surface density distribution, and the fit is quite good over about three and a half scale lengths.

各銀河の水素ガスとHαの面密度間の関係
Star formation law
(Kennicutt 1989, ApJ, 344, 685)

Hαの平均面光度

$$SFR \propto \Sigma_{gas}^{N}$$

$\boxed{N=1.3}$

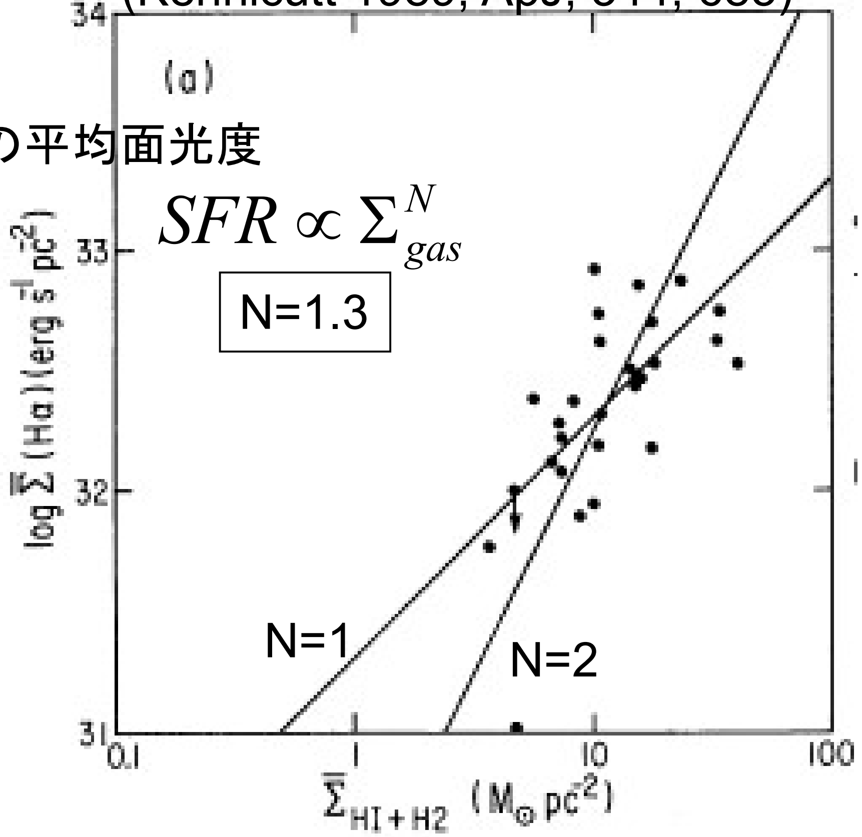

水素ガスの平均面密度

円盤銀河内の各半径における
水素ガスとHαの面密度の関係

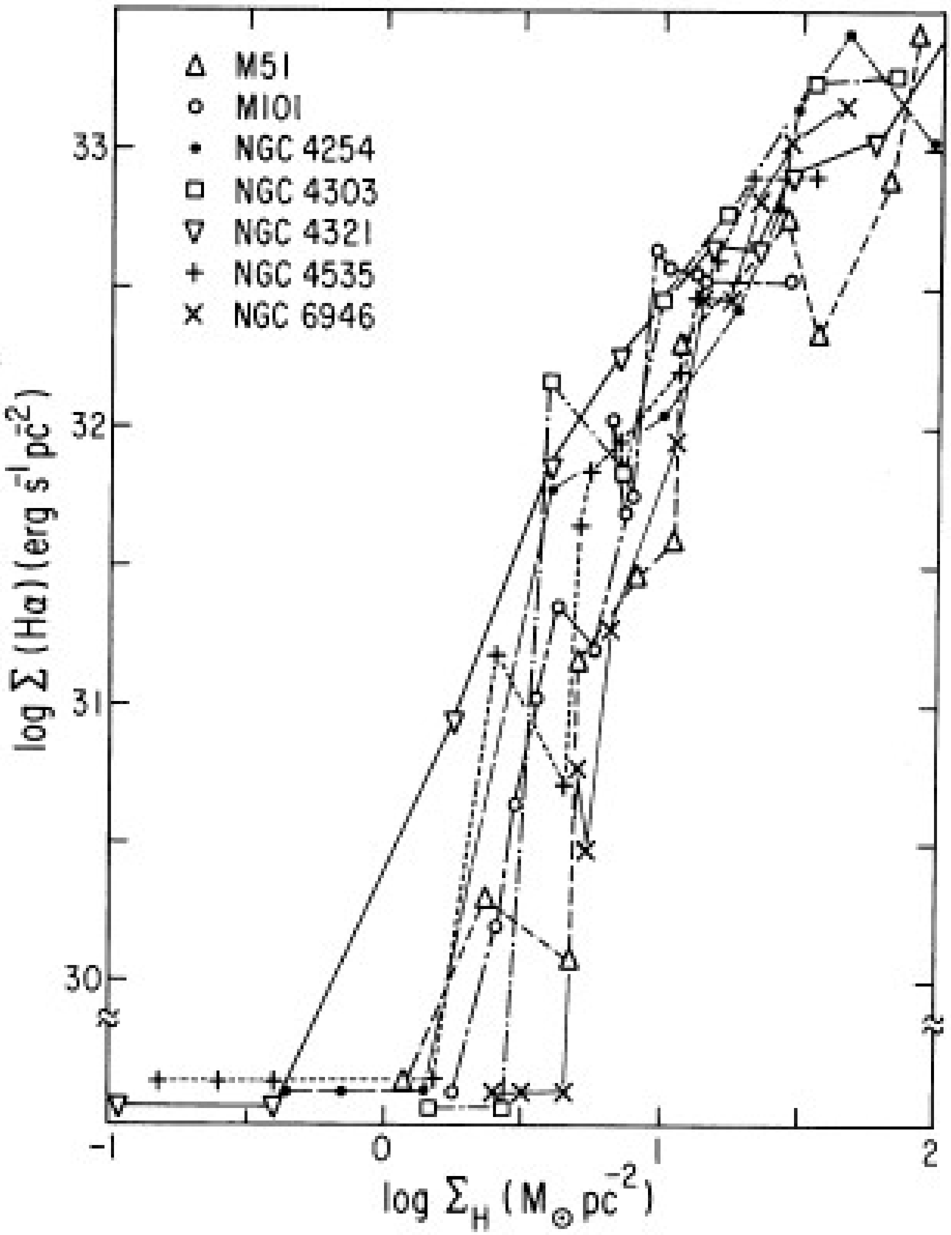

SFR law for 61 disk galaxies and 36 starburst galaxies

Kennicutt 1998,
ApJ, 498, 541

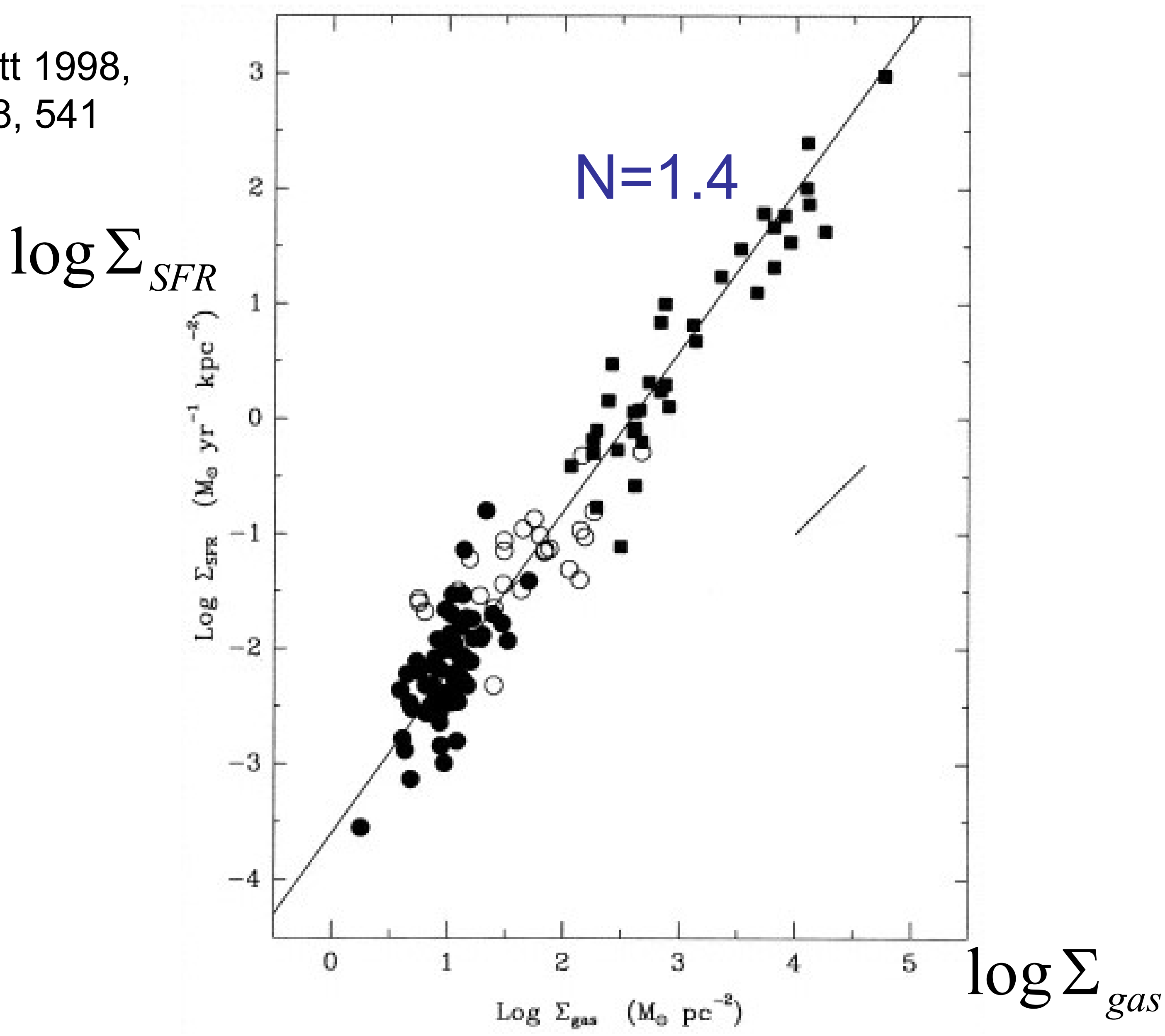

Initial Mass Function

$\phi(m) \propto m^{-\alpha}$ $(\int m\,\phi(m)dm = 1M_{sun})$

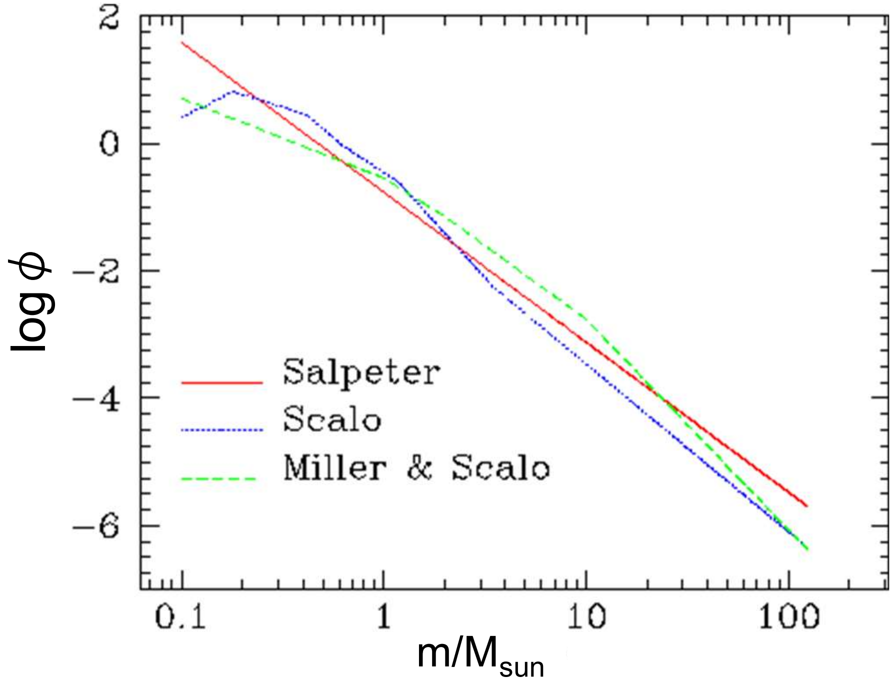

- Salpeter (1955)

  α = 2.35 for $1M_{sun}$ < m

- Miller and Scalo (1979), Scalo (1986)

  $\alpha \rightarrow 0$ for m < $1M_{sun}$

- Kroupa (2002)

  α = 0.3 for m < $0.08M_{sun}$

  1.3 for 0.08 < m < $0.5M_{sun}$

  2.3 for $0.5M_{sun}$ < m

Kroupa (2002)

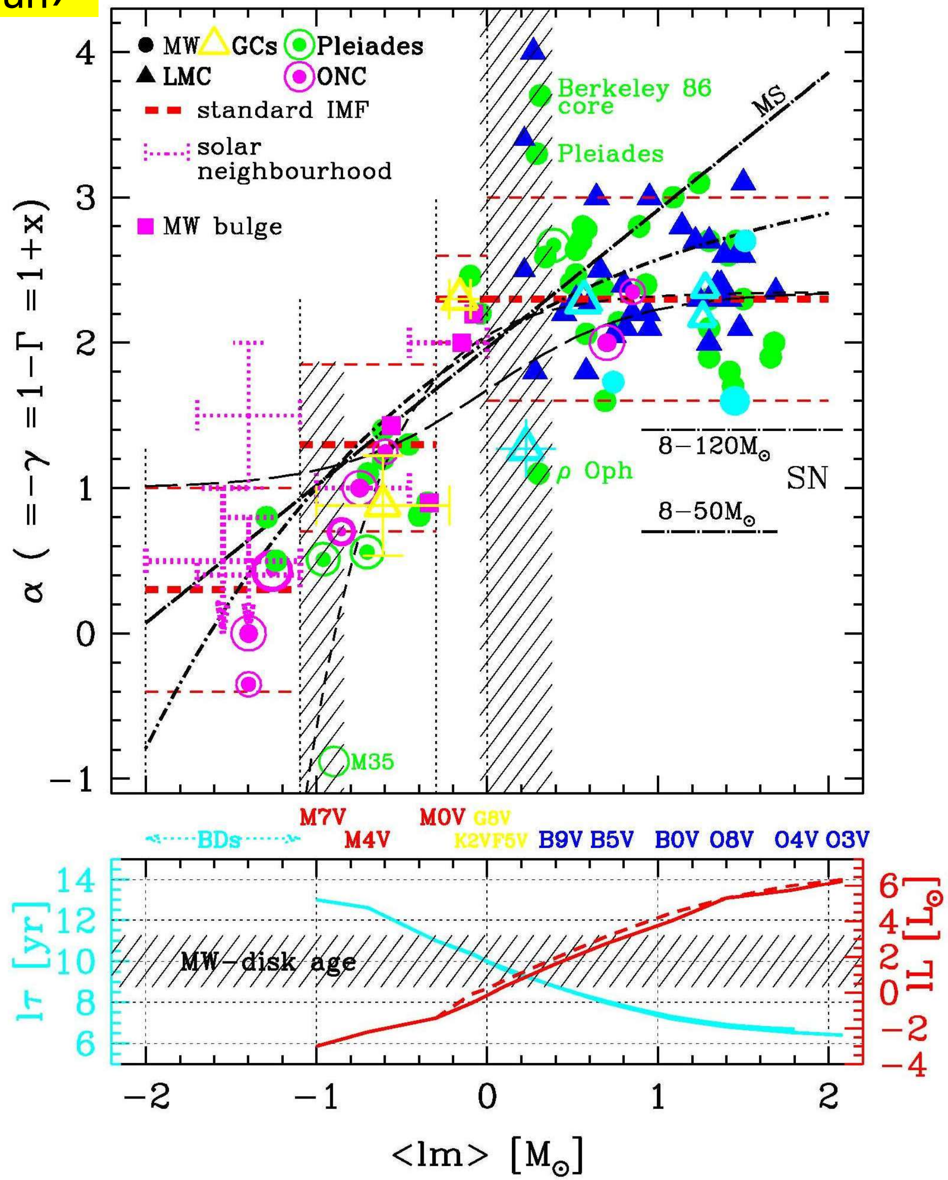

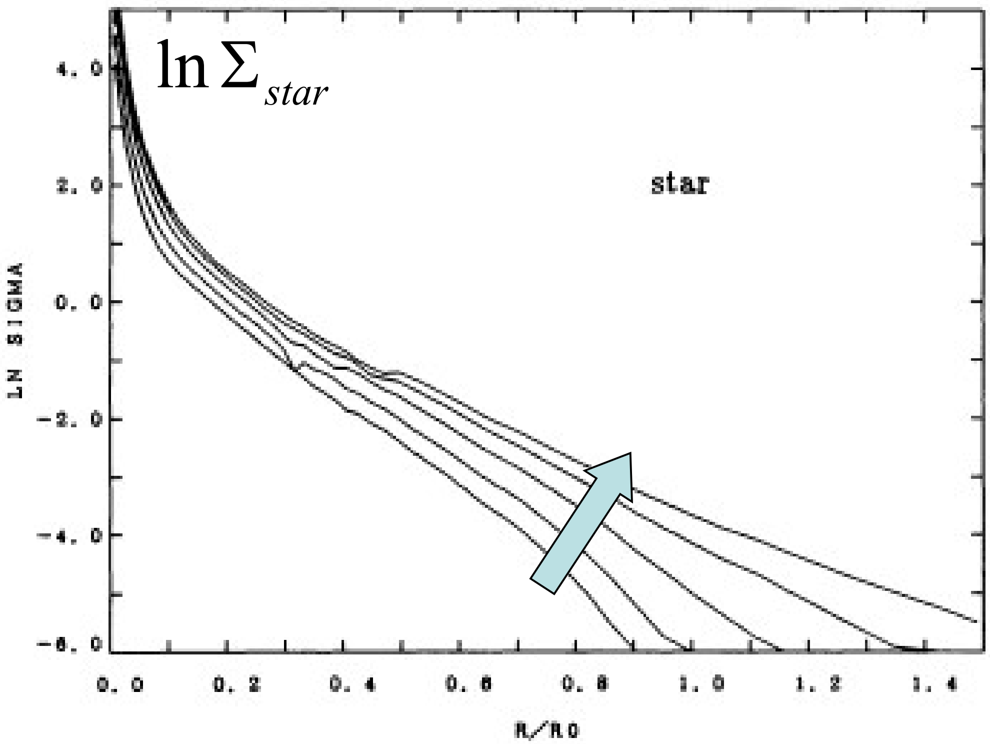

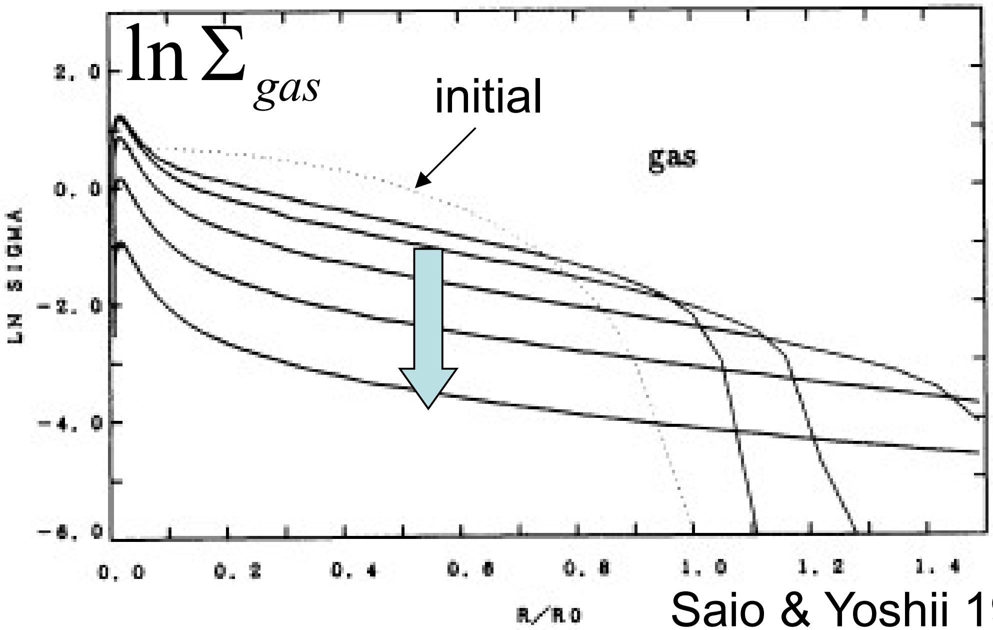

円盤内の各Rにおける星形成タイムスケール（t_{SF}）
重力粘性のタイムスケール（t_{vis}）がほぼ同じ場合の
星とガスの面密度の進化
Yoshii & Sommer-Larsen 1989,MNRAS, 236,77

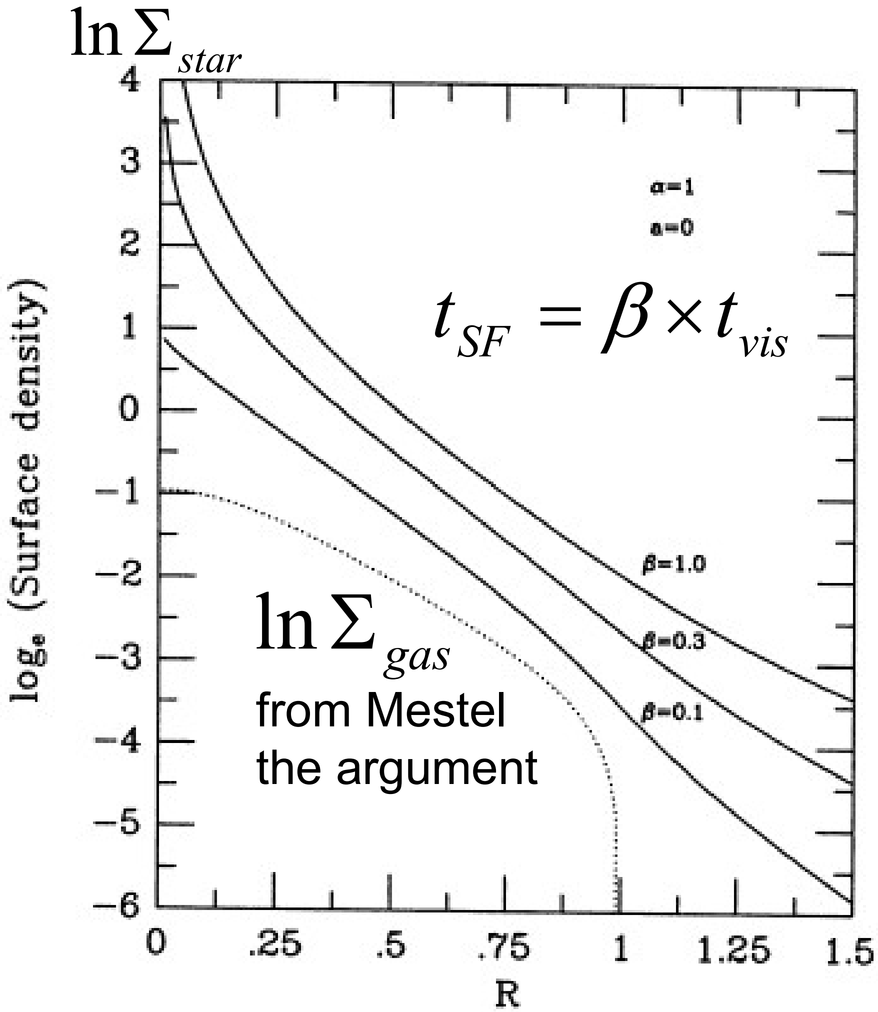

Saio & Yoshii 1990, ApJ, 363, 40

階層的合体による円盤構造の形成
左図：ダークマター粒子とガス粒子の発展

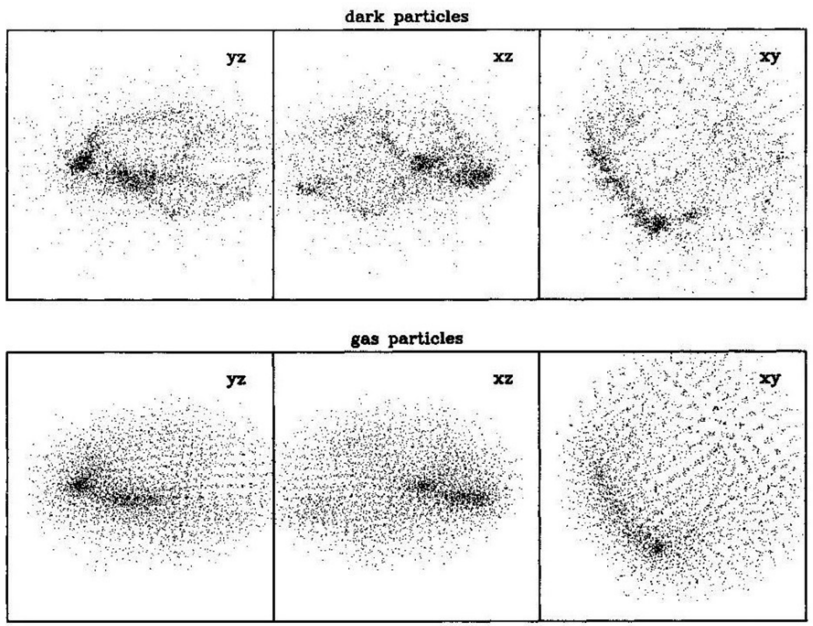

z = 2.70

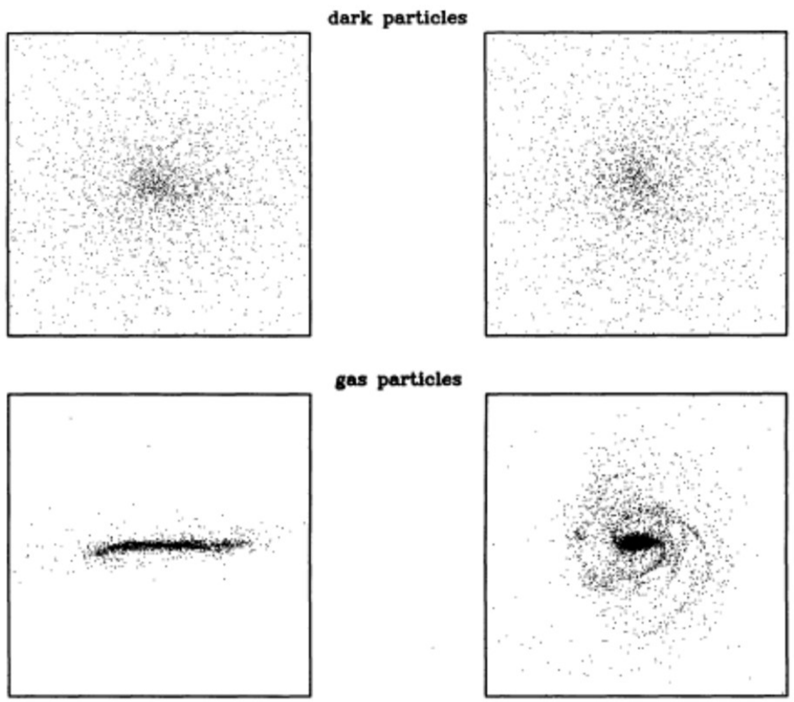

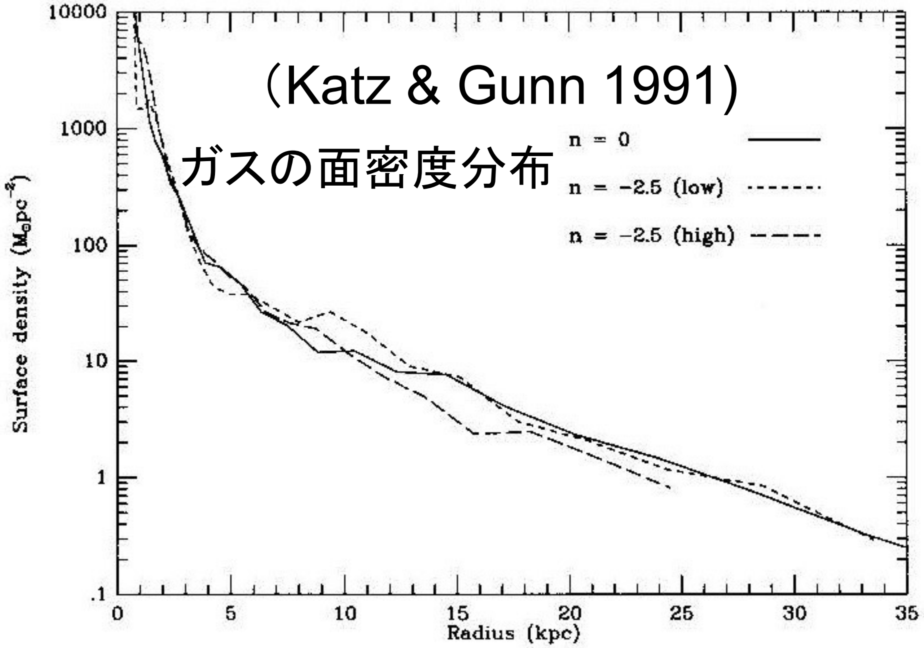

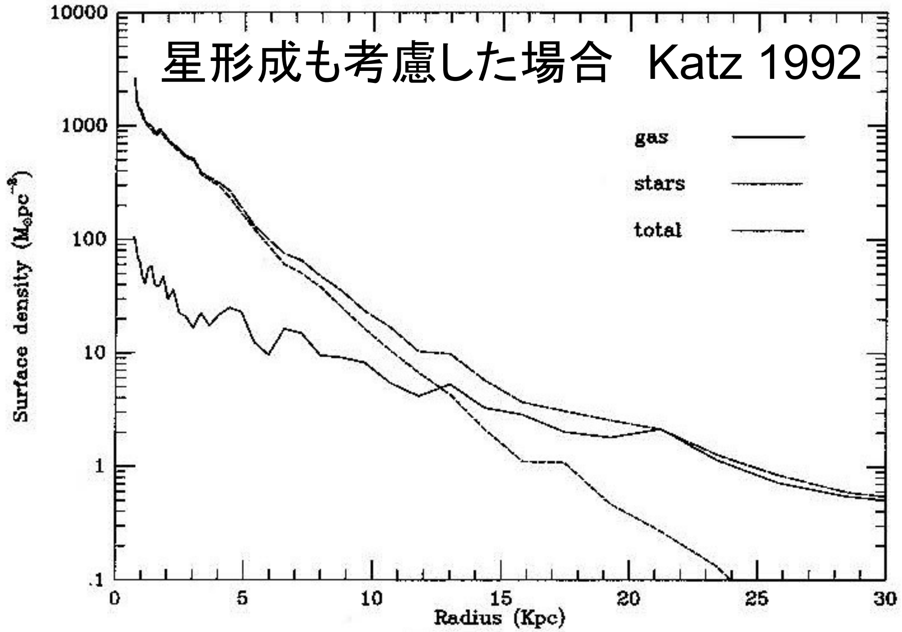

Cosmological simulation: Auriga

Iza+2022

$\dot{M}_{out}/\dot{M}_{in} \approx 0.75$ $\quad$ SFR$/\dot{M}_{in} \approx 0.1\sim0.3$

30 MW-like galaxies

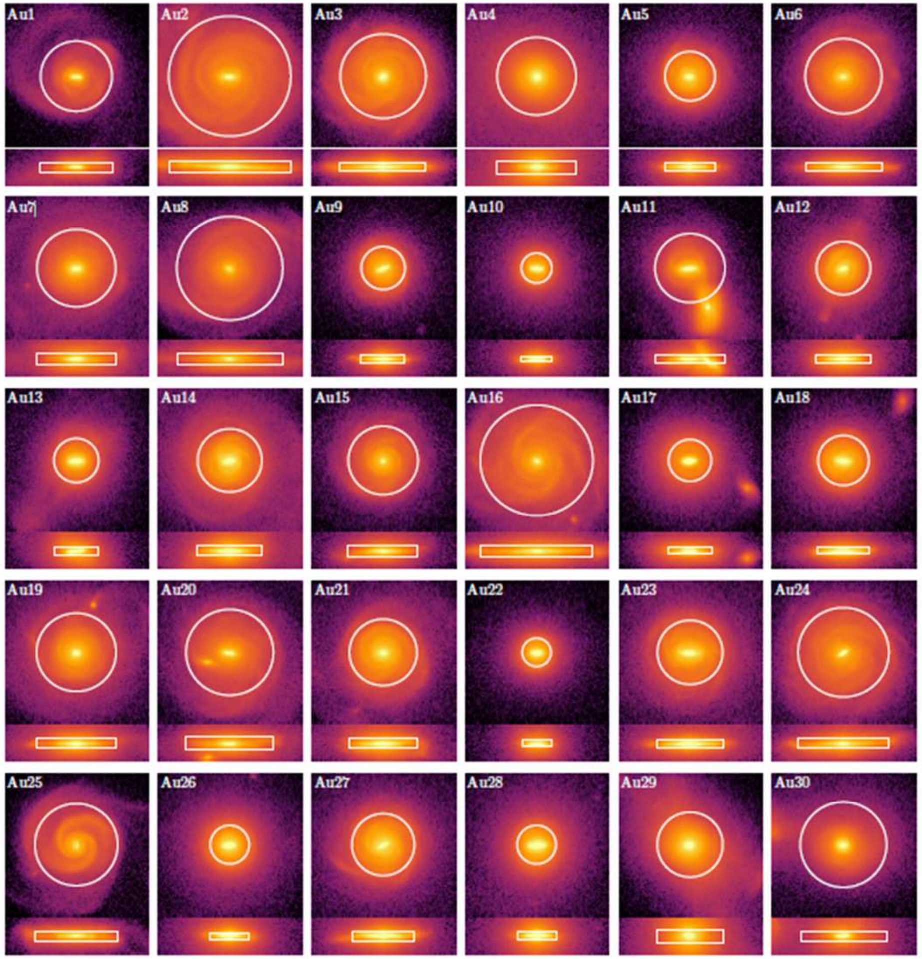

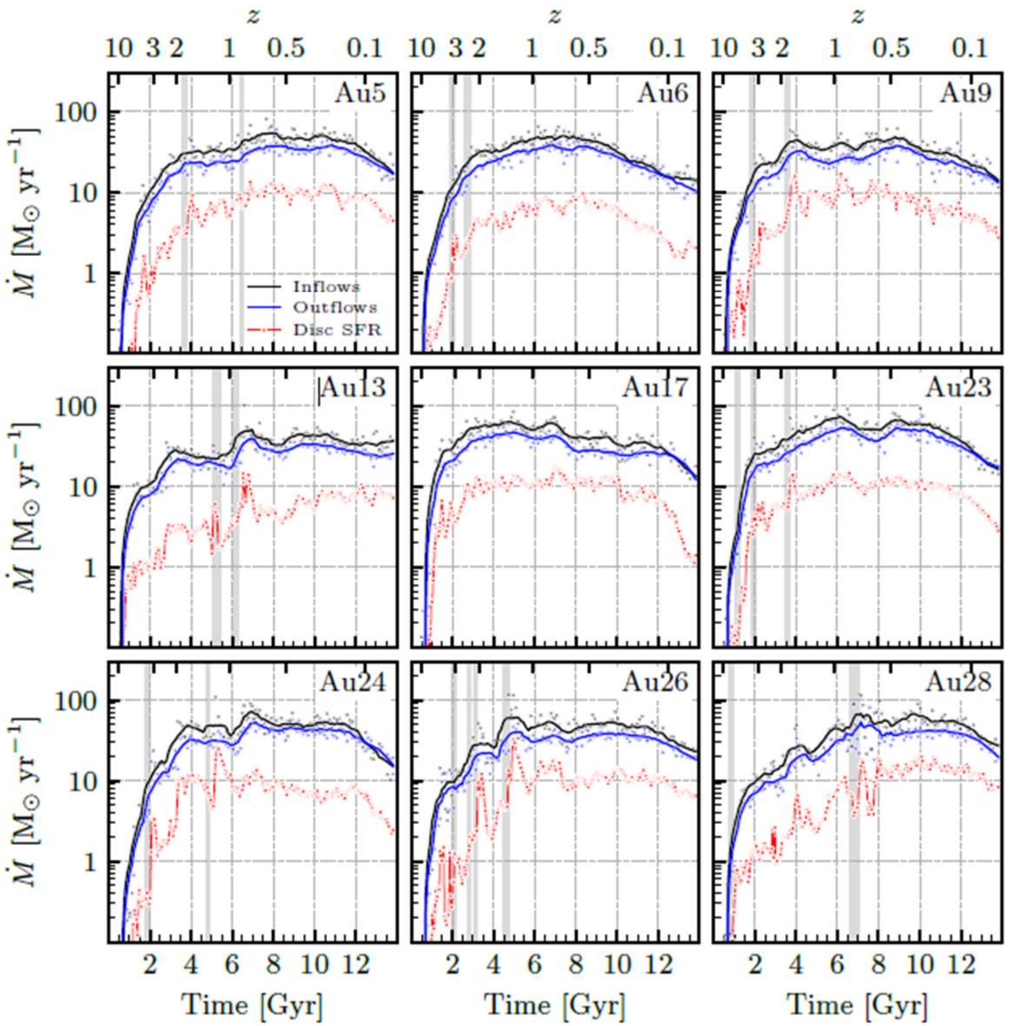

Figure 6. Inflow (black) and outflow (blue) rates calculated with tracer particles for the galaxies that have been re-simulated; lines show the trend and dots the raw data. We also indicate the evolution of the SFR in the disc region (red dots). Background shading indicates times when there is a satellite inside R_{200} with $f_{sat} = \frac{M_{sat}}{M_{cen}} > 0.1$. In general, rates show a rapid increase before reaching a maximum and then decrease to present-day values in the range 10–40 $M_\odot\ yr^{-1}$. Also note that all rates (inflow, outflow and star-formation) follow roughly the same behaviour.

遠方星形成銀河

Milky Way-like galaxiesの進化： van Dokkum et al. 2013

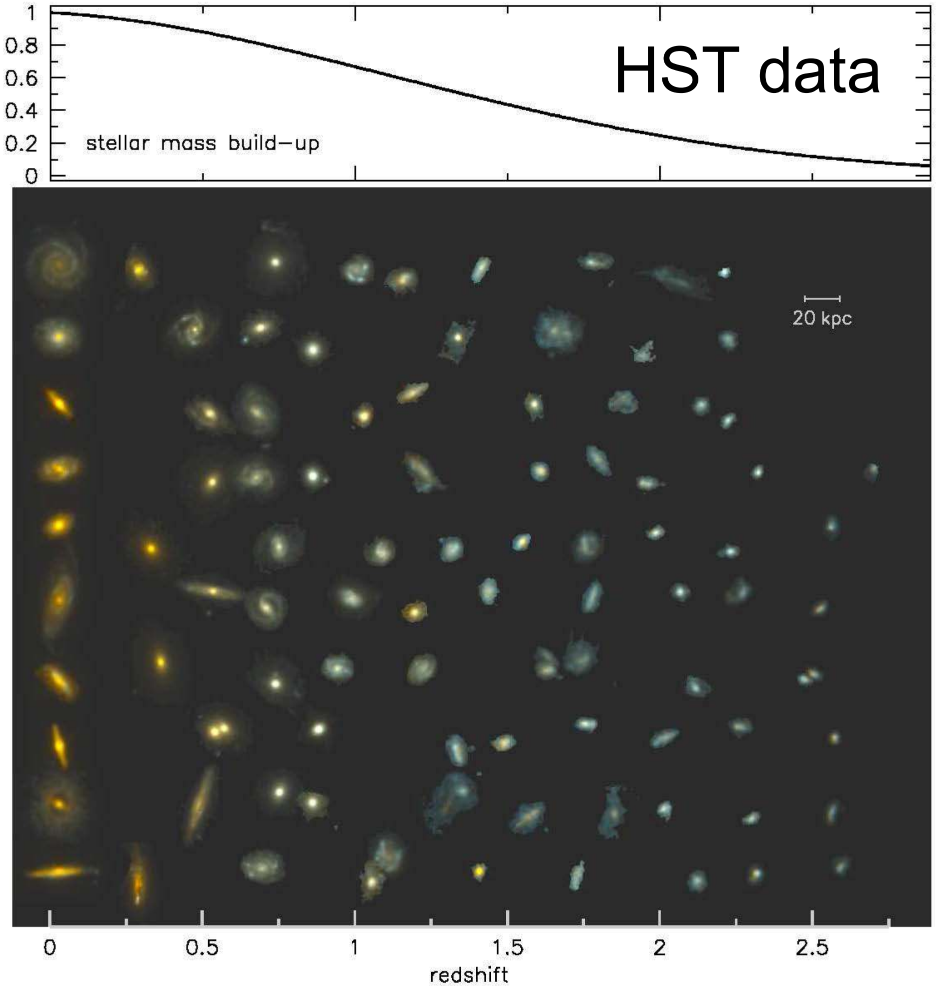

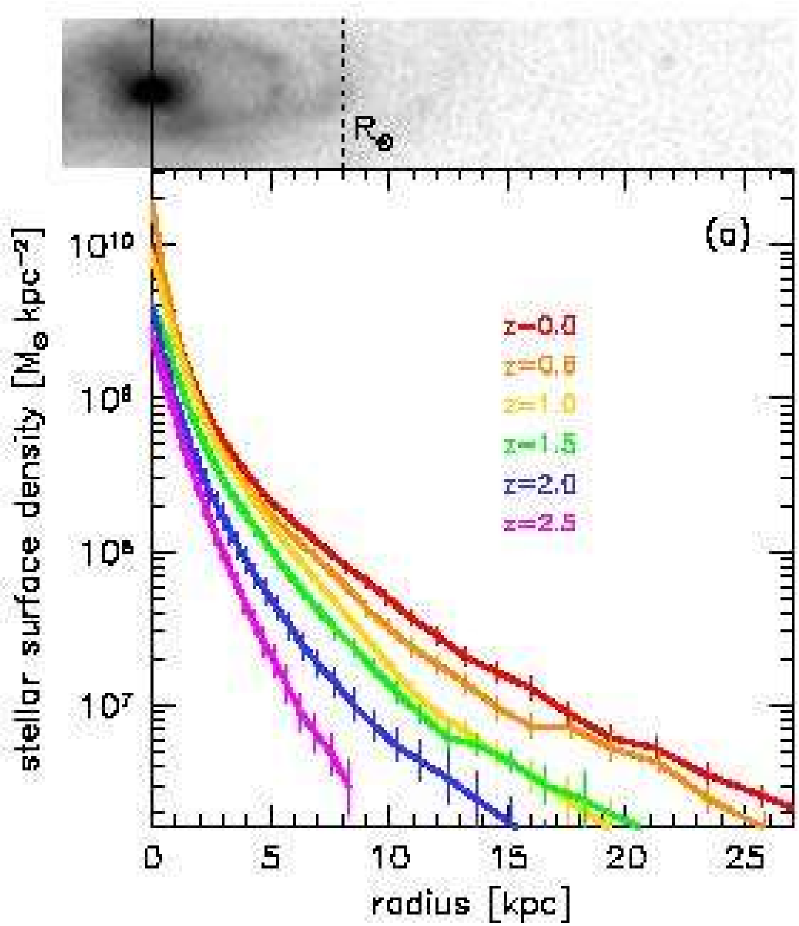

円盤形成に伴うダークハロー質量分布の変化

Barnes 1987 in Nearly Normal Galaxies

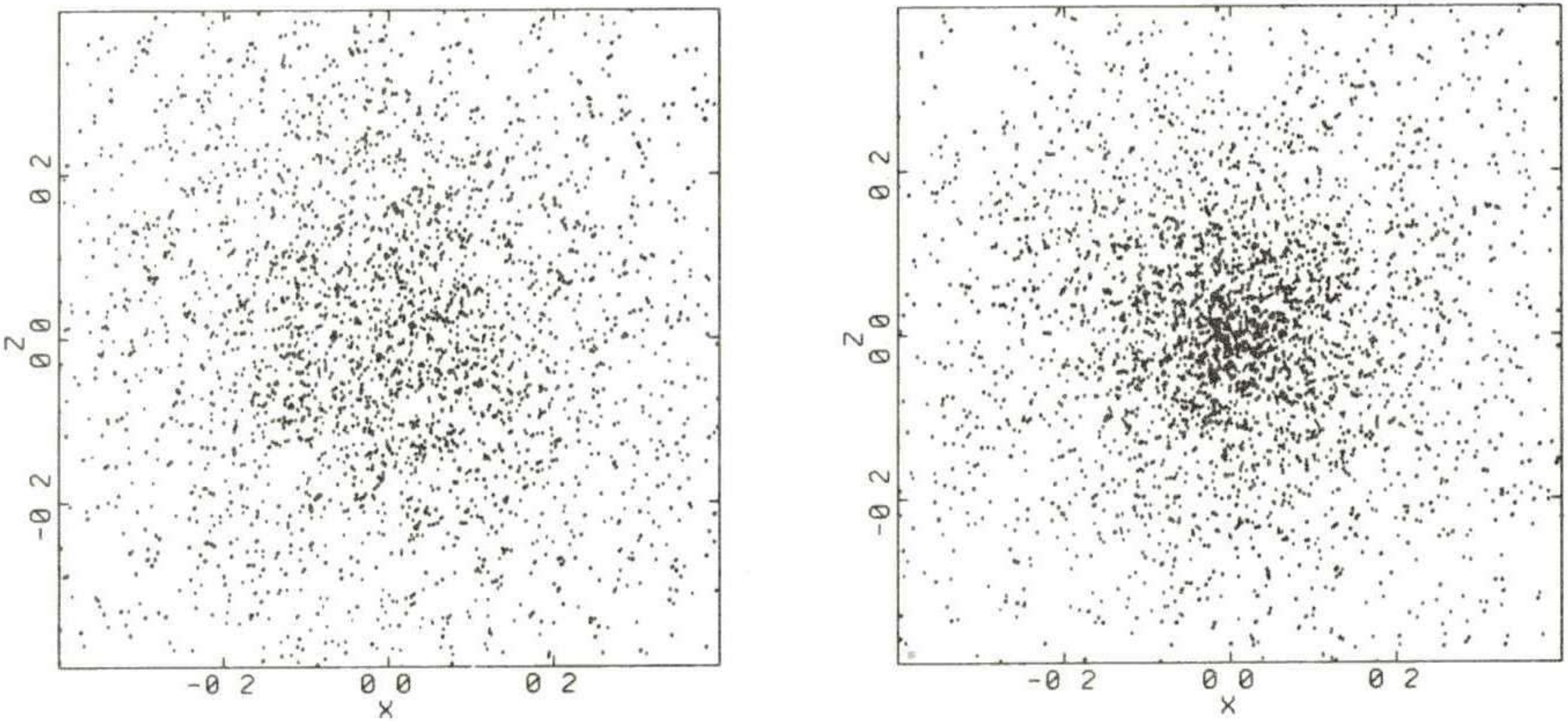

Figure 1. Galactic halo shown before (left) and after (right) the imposition of a disk with mass $M_d = 0.1 M_h$ and scale $\alpha^{-1} = 0.025 R_V \simeq r_c^0/8.2$. The disk is perpendicular to the **z** axis; note lack of halo flattening.

銀河の断熱的収縮にともなう回転曲線の変化

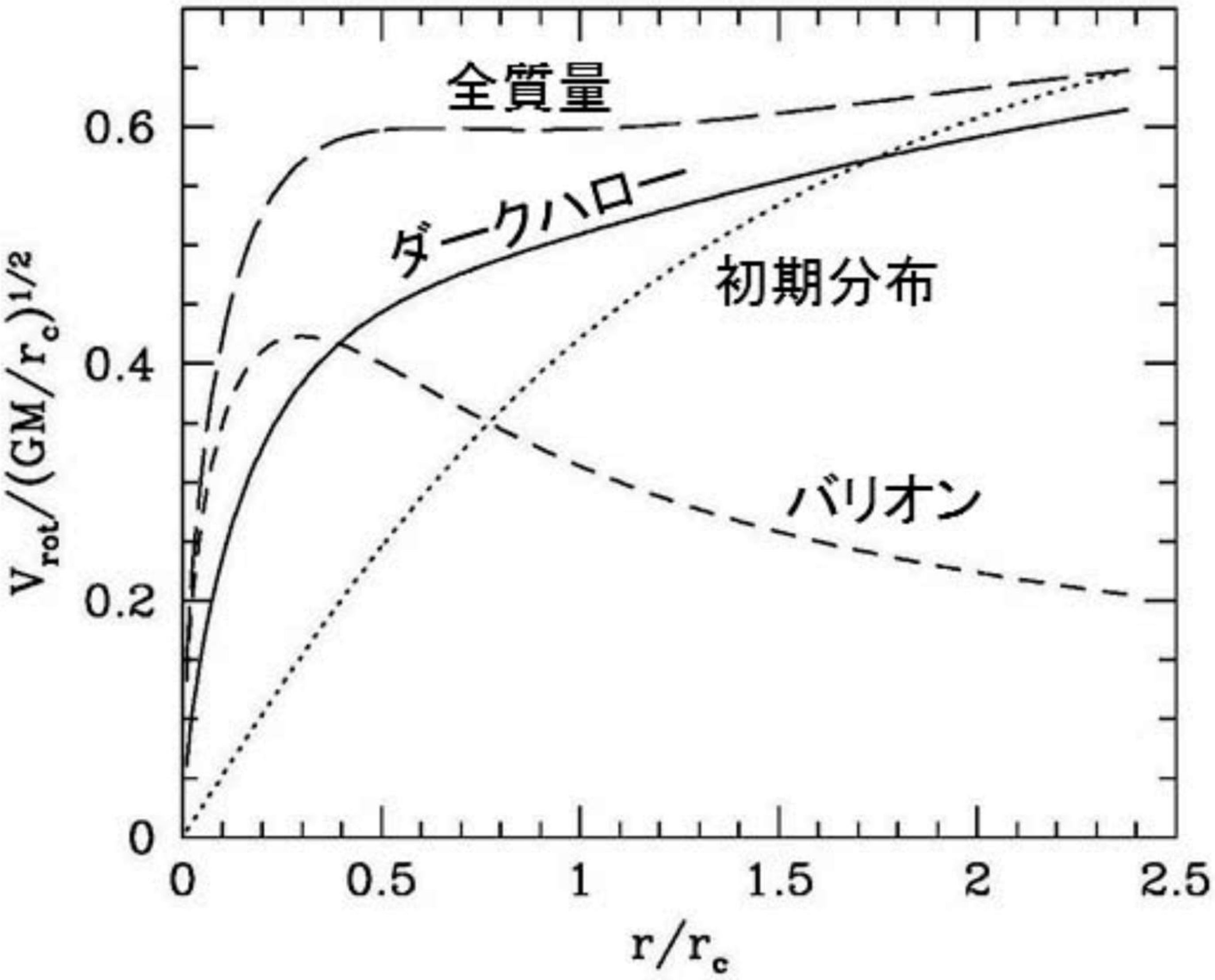

太陽近傍にある薄い円盤星

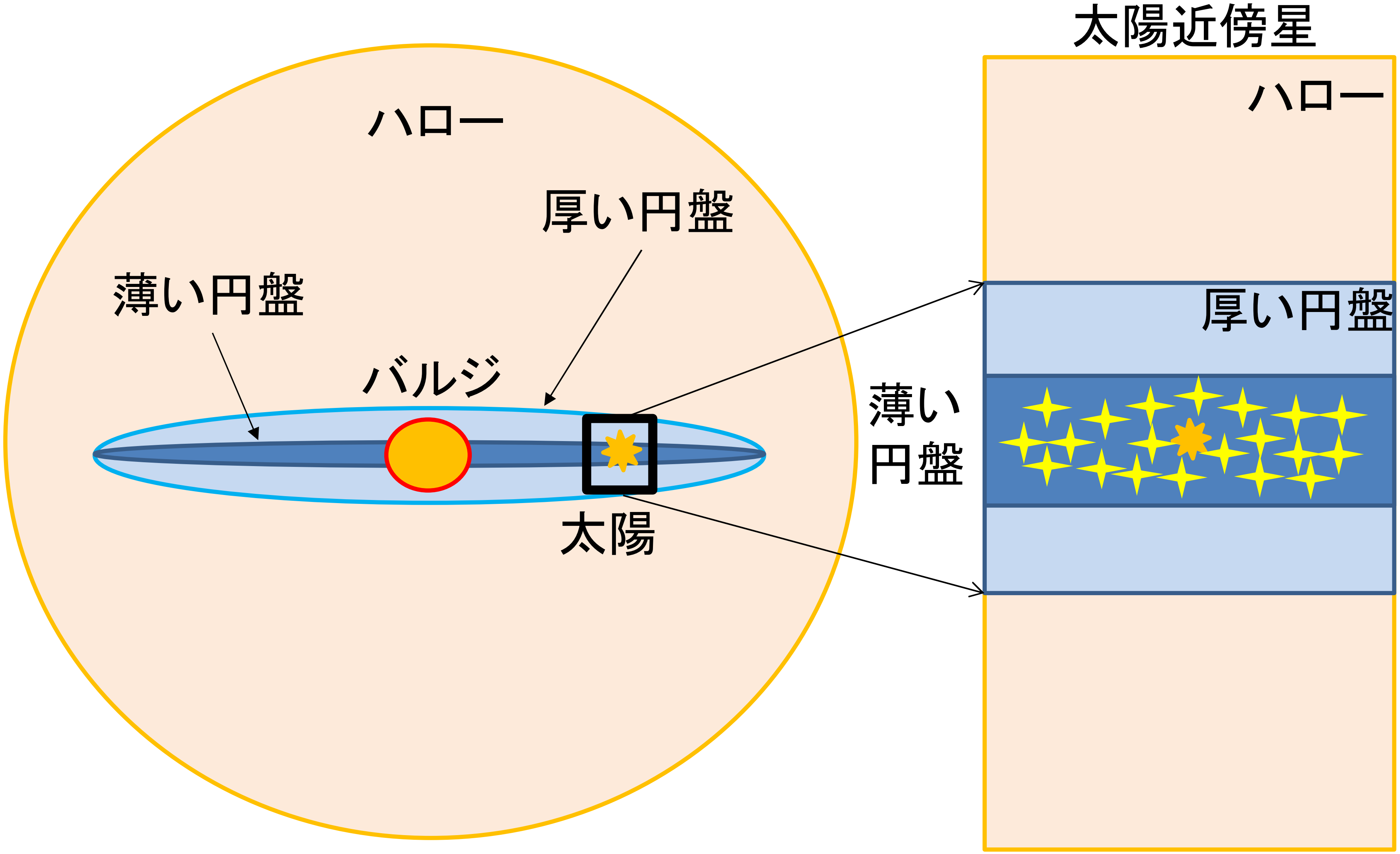

太陽近傍の化学進化(I)

- シンプルモデル:最も簡単なケース

  Closed box: ガス質量＋星質量=一定

  inflow/outflowなし

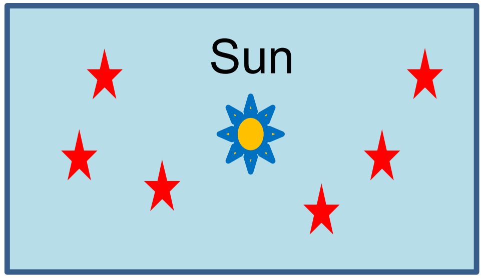

Metal-free gasを最初に置いてスタート

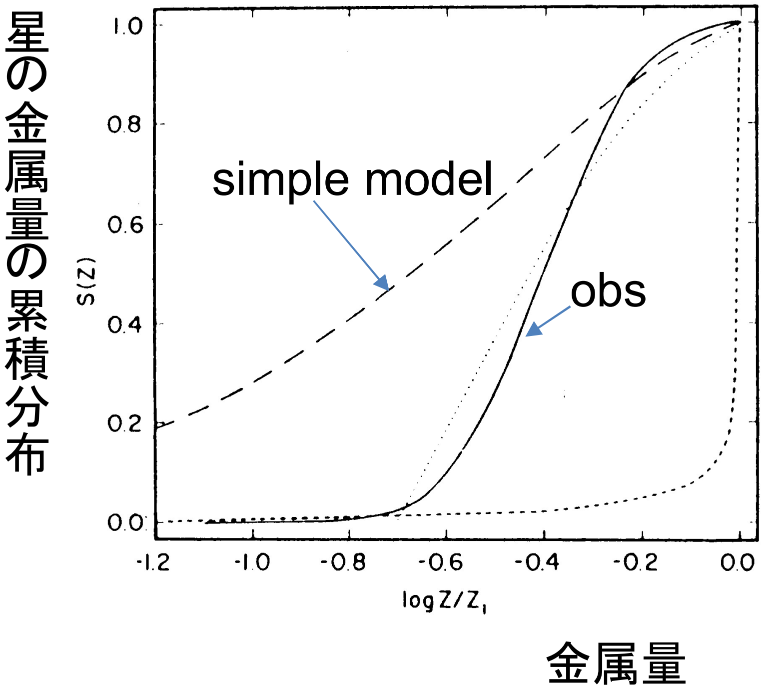

しかし、、、

Obs: 太陽近傍のG型矮星の金属量分布

シンプルモデルは金属欠乏星を作りすぎ

⇒ G-dwarf problem

Tinsley 1980, FCPs, 5, 287

太陽近傍の化学進化(II)

- G-dwarf問題を解決するには？

ハローから落ちてきたガスから円盤形成

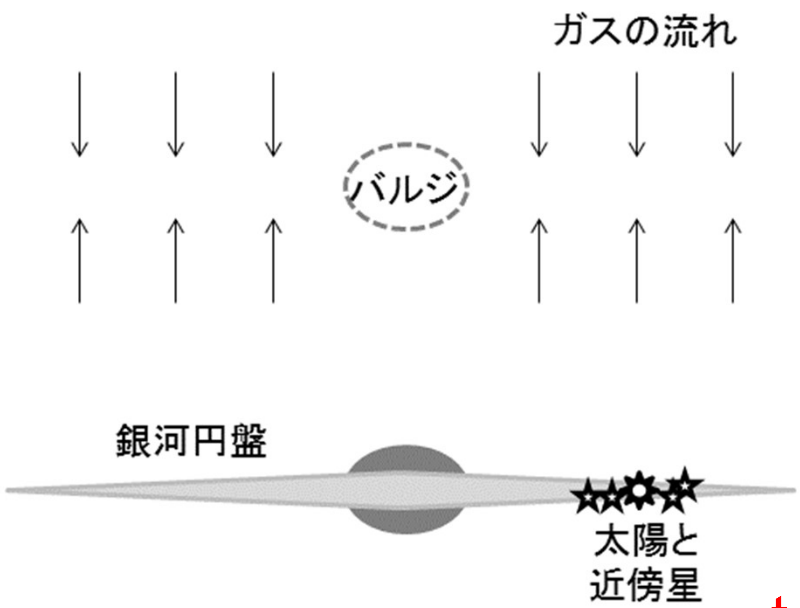

Sommer-Larsen & Yoshii 1990

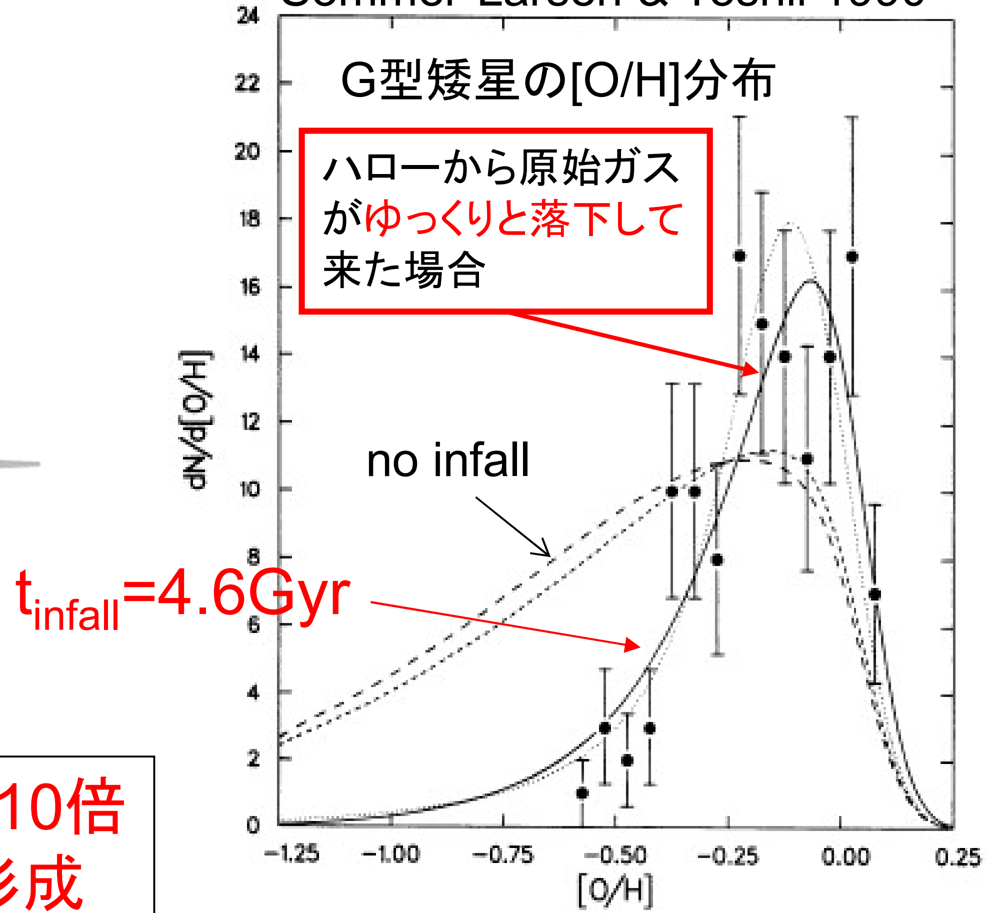

$d\Sigma_{gas}/dt \propto \exp(-t / t_{infall})$

t_{infall}~4-5 Gyr が必要

銀河系円盤は力学時間の10倍以上のゆっくりと時間で形成

薄い円盤（天の川部分）の形成

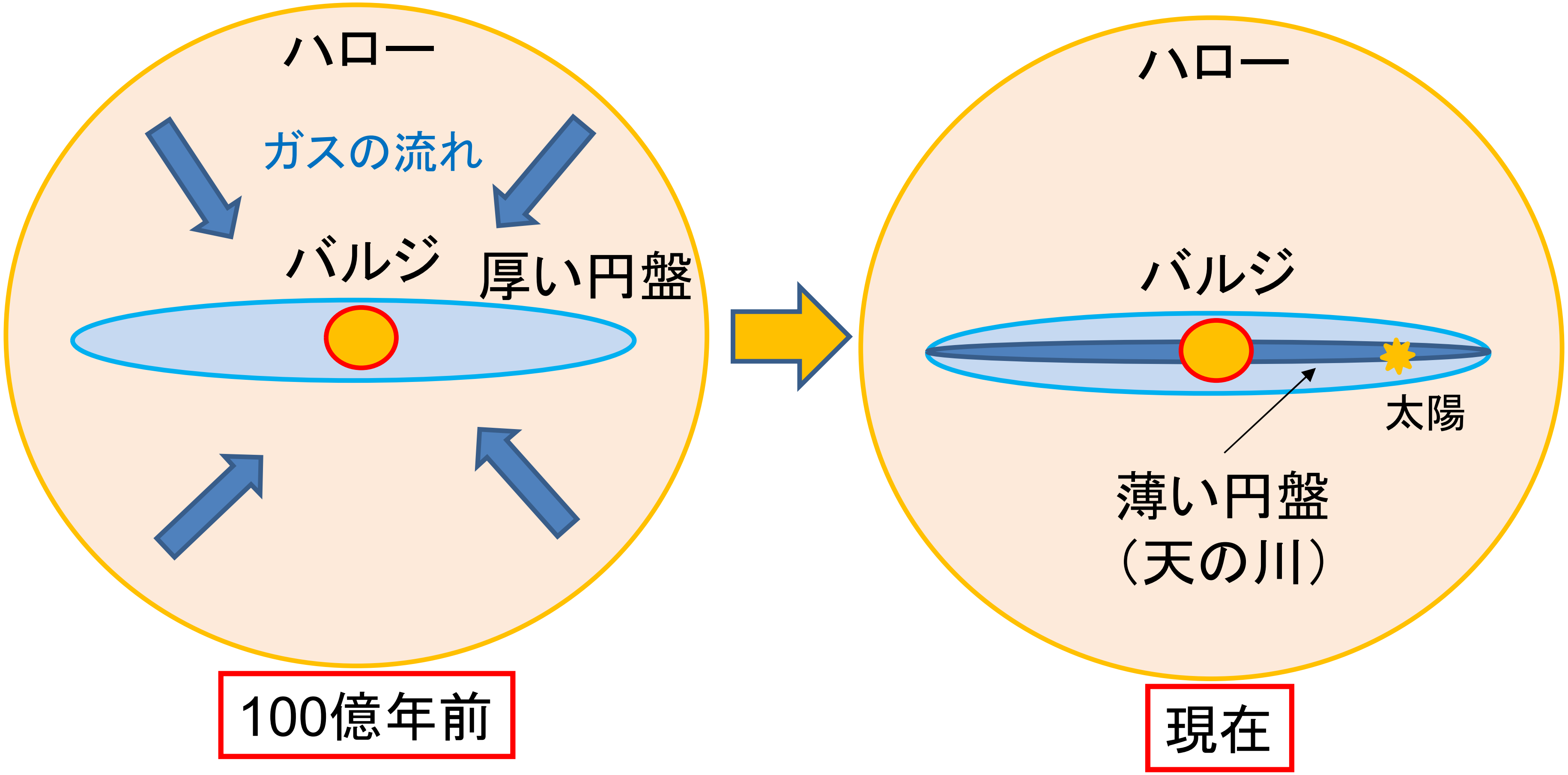

薄い円盤はハローからゆっくりと数十億年の時間をかけて落ちてきたガスから形成された

円盤のでき方

Toyouchi & Chiba 2014

[Fe/H]

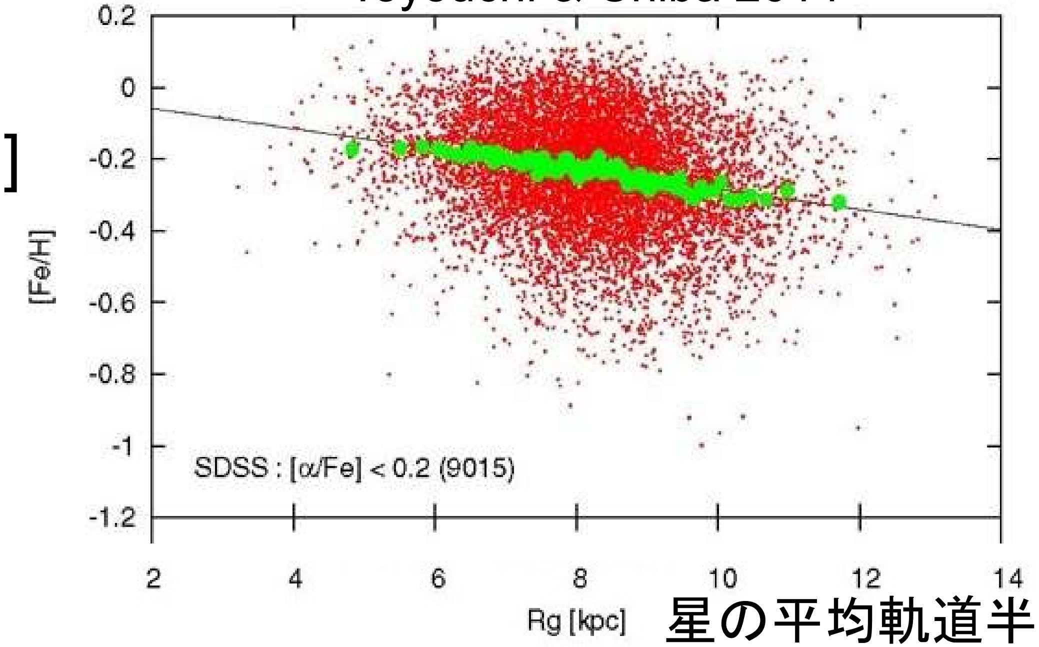

星の平均軌道半径(kpc)

内側ほど金属量多い

↓

内側ほど星形成が進んできた

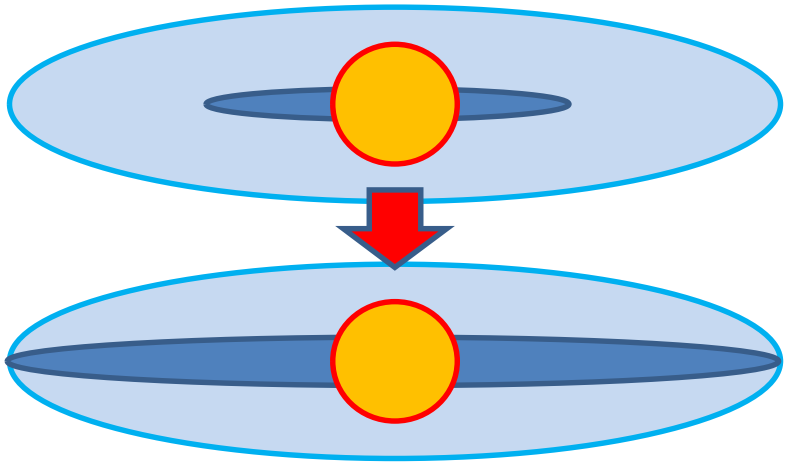

内側から外側にかけて薄い円盤が形成された
Inside-out formation

太陽近傍の若い星の金属量分布との比較

Feltzing & Chiba (2013)
using Nieva and Przybilla (2012) data

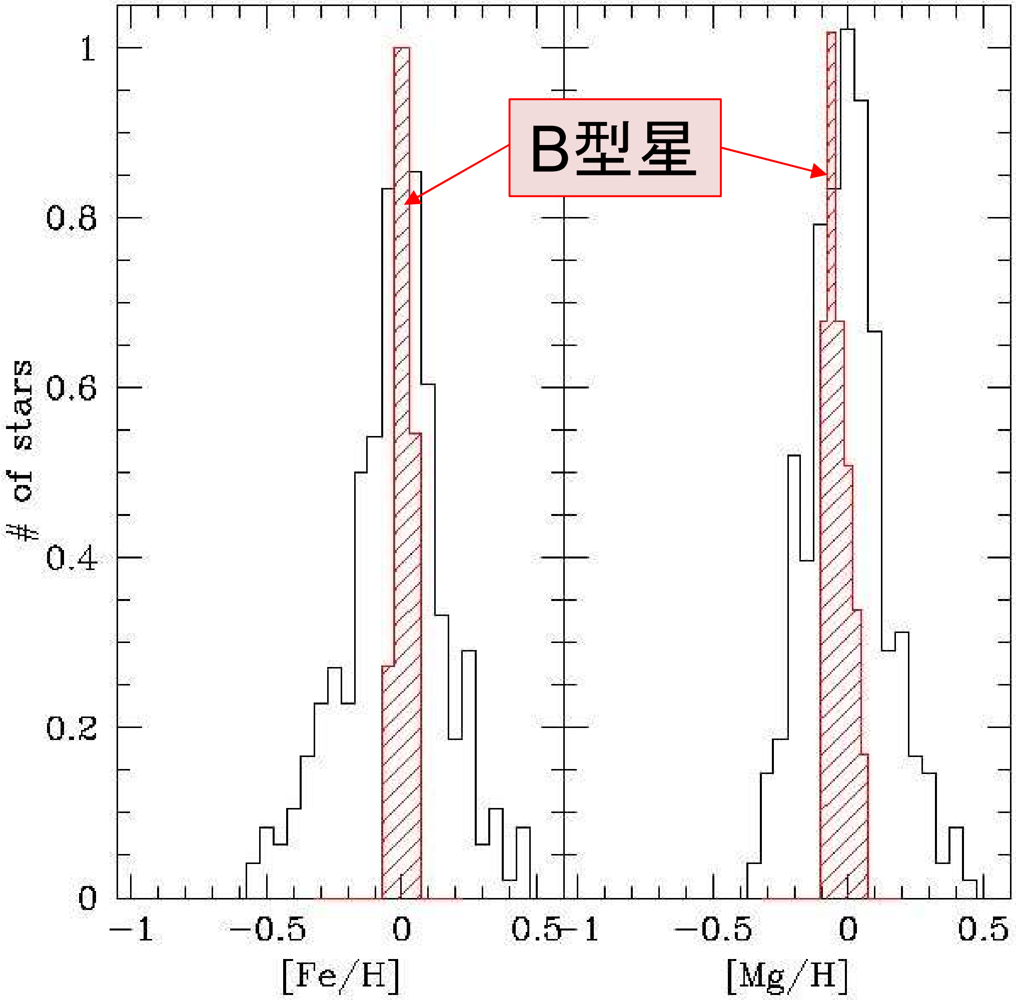

B型星の金属量分布
は星間媒質の金属量
を反映

[Fe/H] > + 0.2のような
very metal-rich starsは
太陽近傍で作れない。

銀河系円盤の化学進化

星が誕生した銀河動径 R_f での金属量分布の理論予想
（Toyouchi & Chiba 2018）

[Fe/H]>+0.2の高金属量の太陽近傍星は
銀河円盤内側（R= 3～6 kpc）で生まれている

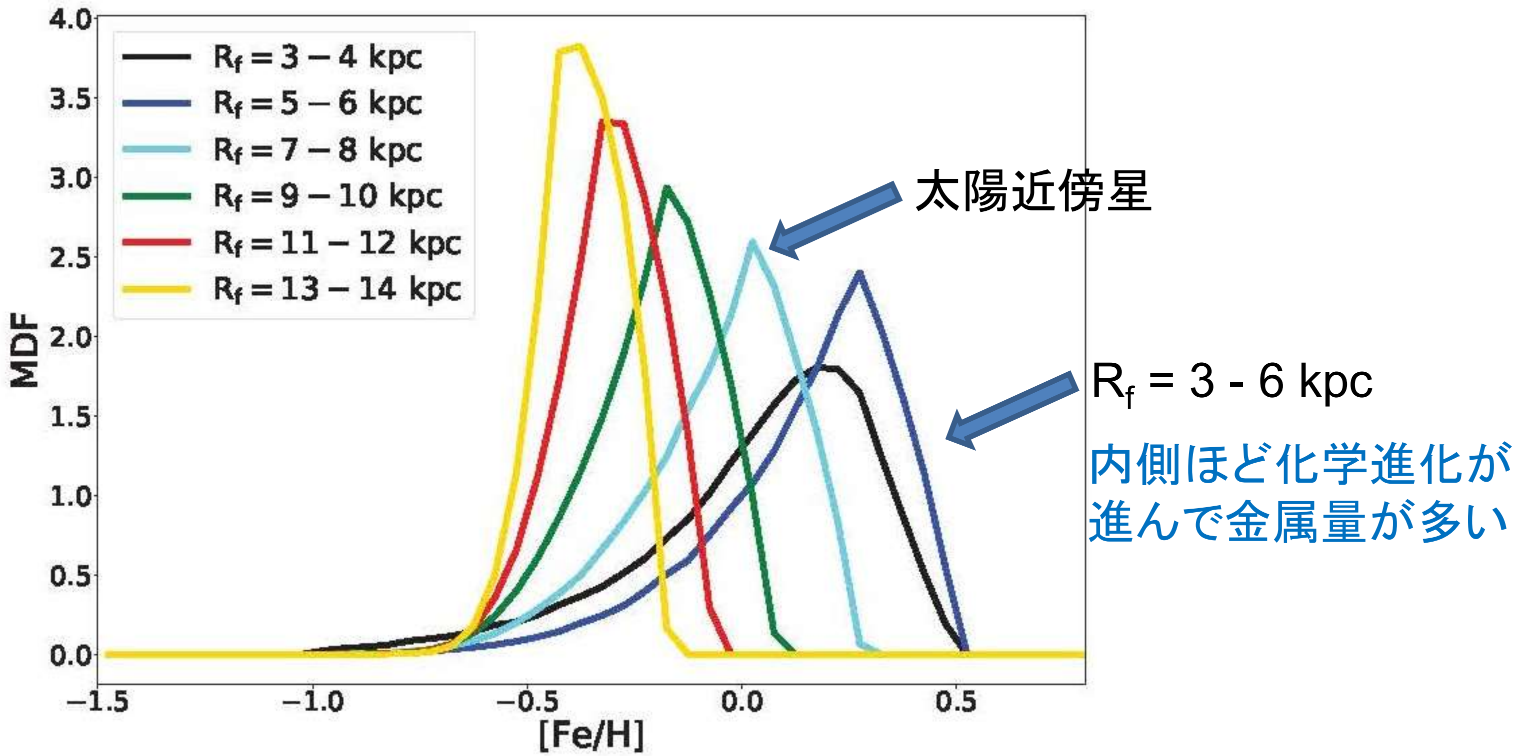

星の金属量 （太陽値との相対比の対数）

Radial migration

Sellwood & Binney 2002, Schoenrich & Binney 2009

内側で円軌道にある星で
・摂動をうけたもの
・角運動量を得たもの

外側で円軌道にある星で
・摂動をうけたもの
・角運動量を失ったもの

transient spiral arms & bar
あるいはsatellite merging
などのイベントが引き金で、
別の半径で生まれた星が
移動してくる

Metal-rich stars

Metal-poor stars

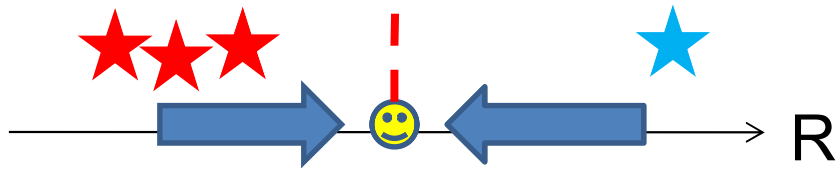

太陽近傍

L_z～一定から、
内側から移動してきた星：V_Φが周囲星より小
外側から移動してきた星：V_Φが周囲星より大

Radial migration の間接証拠

太陽近傍円盤星の元素組成比

Bensby+ 2014

[α元素/Fe]

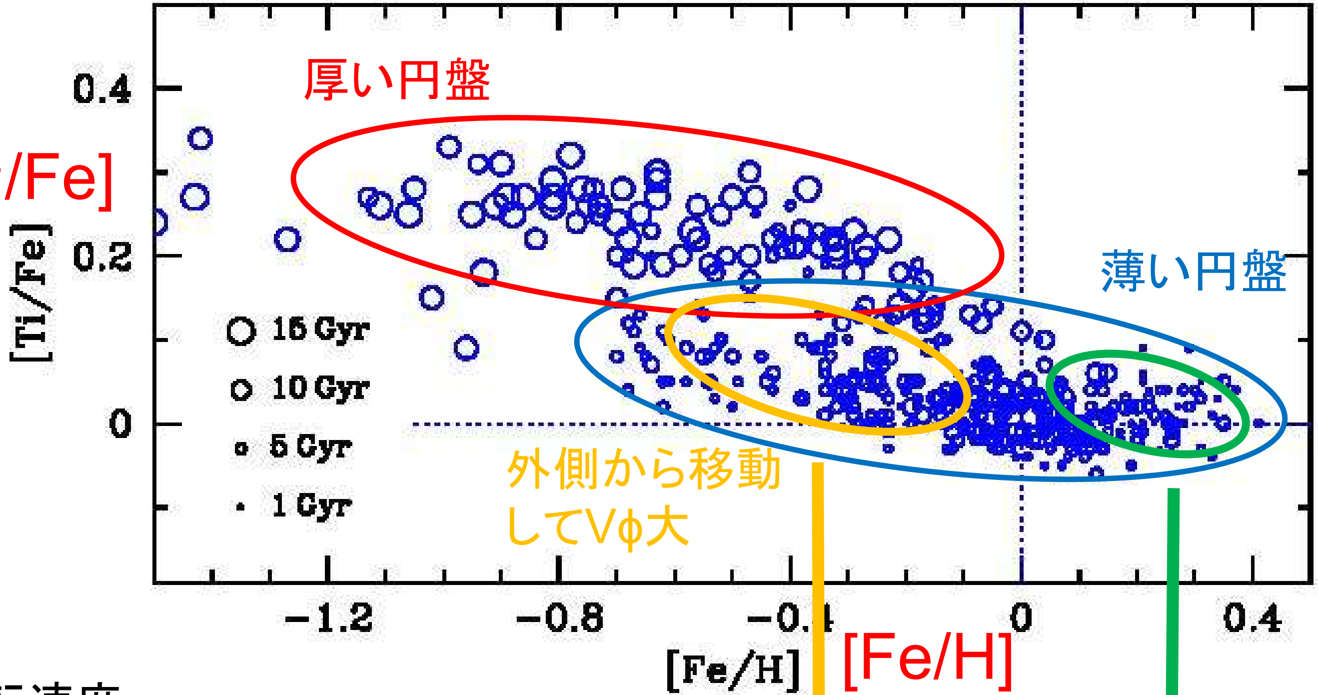

[Fe/H]

内側から移動
してVϕ小

平均回転速度
<Vϕ>
(km/s)

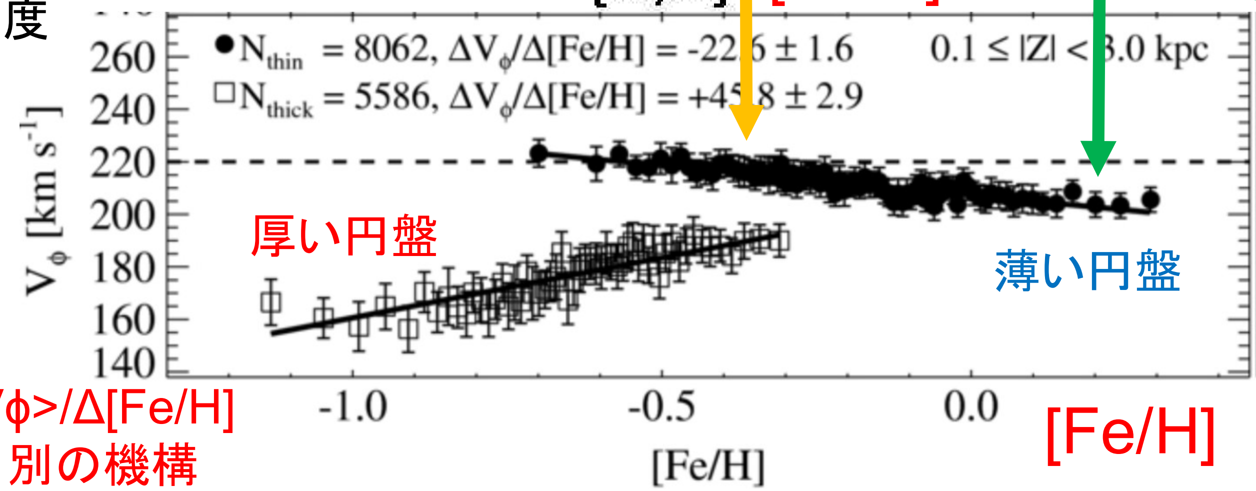

Δ<Vϕ>/Δ[Fe/H]
< 0: migration

Lee et al. 2011

Δ<Vϕ>/Δ[Fe/H]
> 0: 別の機構

[Fe/H]

惑星を持つ恒星の金属量依存性

Johnson et al. 2010

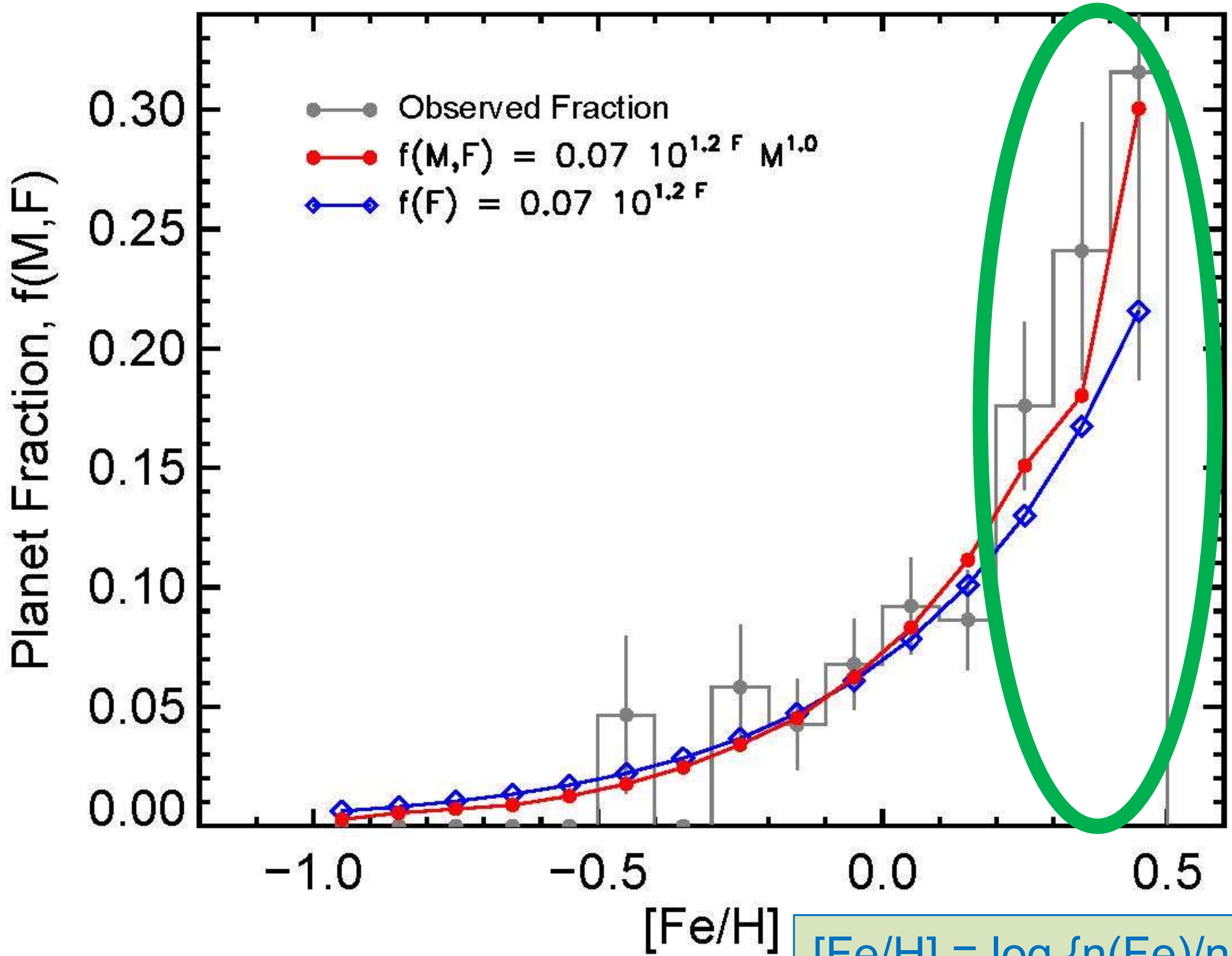

これらの星
（[Fe/H]>+0.2）は
どこでどうやって
できたのか？

（太陽近傍では
このような星は
できない。）

[Fe/H] = log {n(Fe)/n(H)}_星 – log {}_太陽
例：　[Fe/H] = -1:　太陽金属量の10^{-1}

<u>Gaseous</u> Oxygen abundance in M81
Garnett & Shields 1987, ApJ, 317, 82

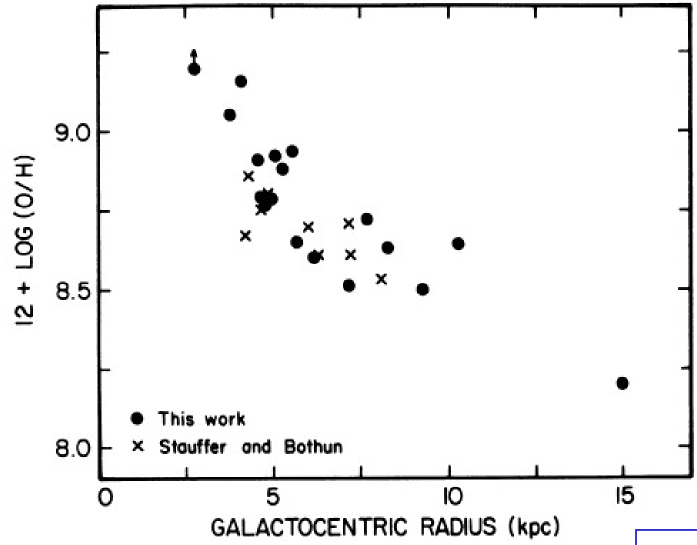

Gaseous Oxygen in various galaxies

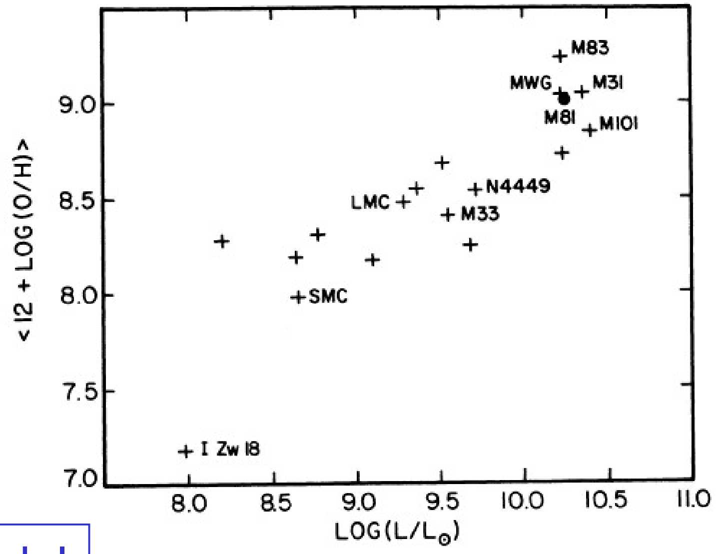

Simple model

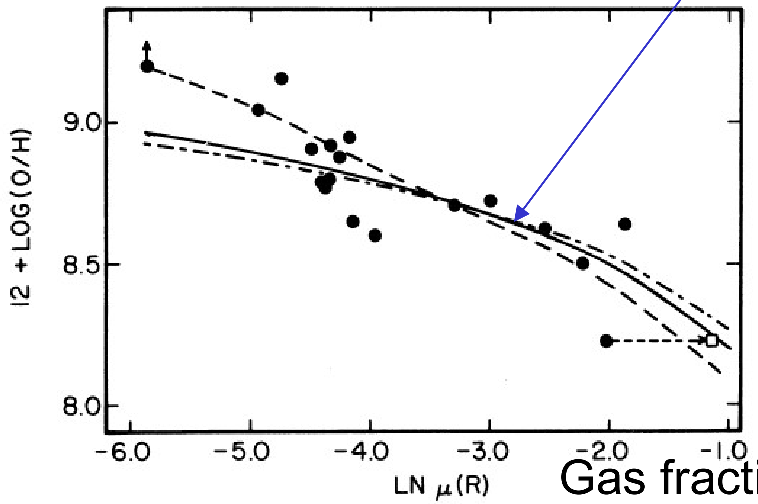

Gas fraction (HI)

FIG. 9.—O/H vs. the log of the H I gas fraction for H II regions in M81. The solid line represents the results from the "simple" chemical evolution model with yield $y = 0.004$; the dot-dash line gives $Z^*(\mu)$ from Clayton (1986) with $y = 0.0055$, while the dashed line shows the predictions from the variable-yield model of Edmunds and Pagel (1984). The square marks the position of Münch 1 if the surface density is computed from an extrapolation of the exponential disk.

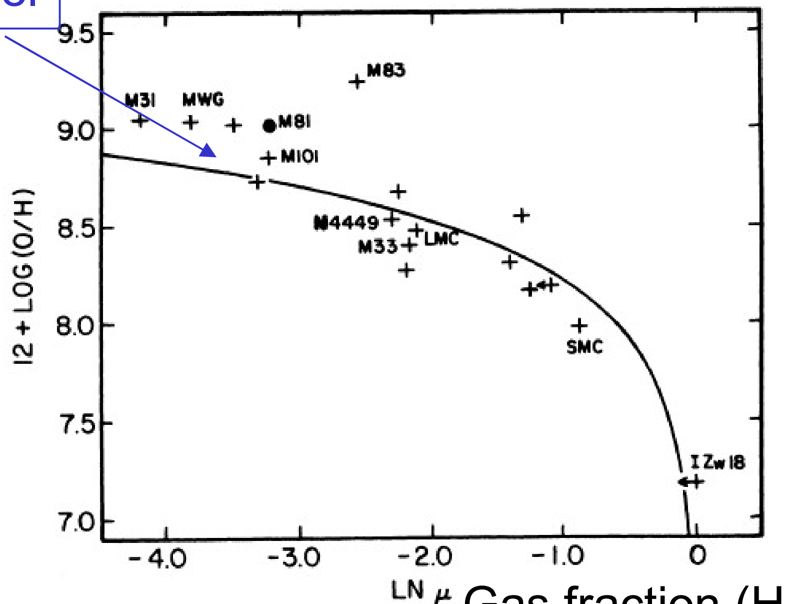

Gas fraction (HI)

SFH of disk stars within 2kpc from the Sun

Ruiz-Lara et al. 2020 Nature Astronomy

Using Gaia DR2

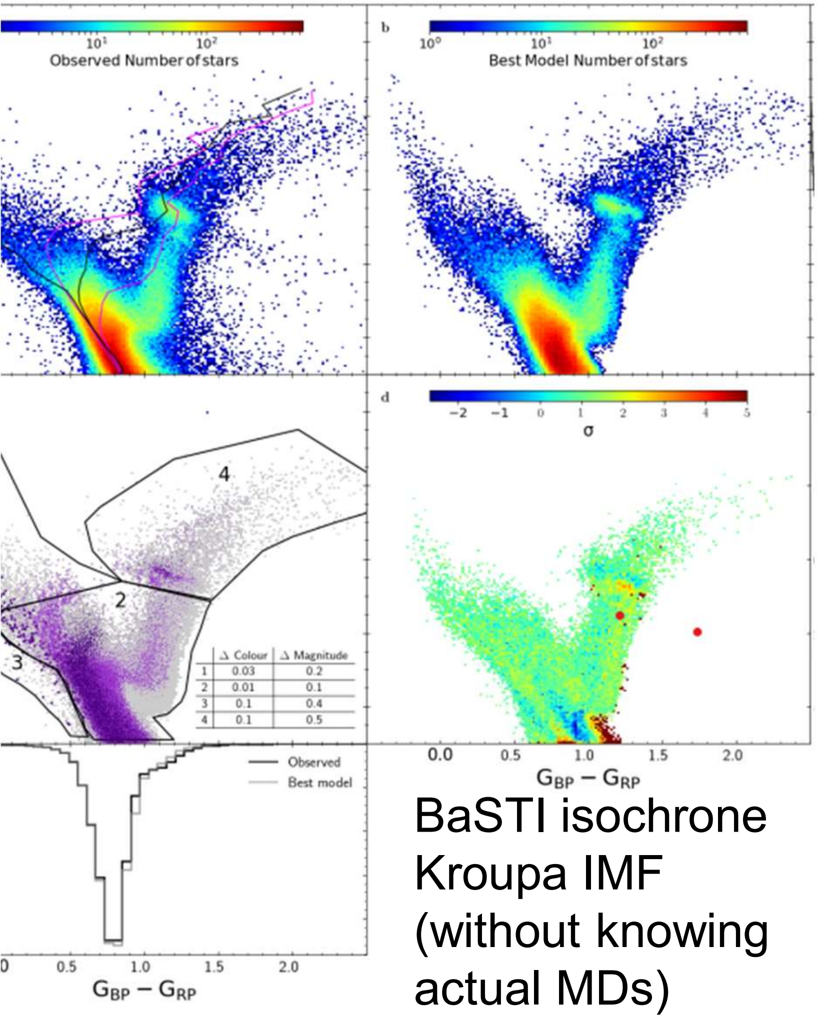

BaSTI isochrone
Kroupa IMF
(without knowing actual MDs)

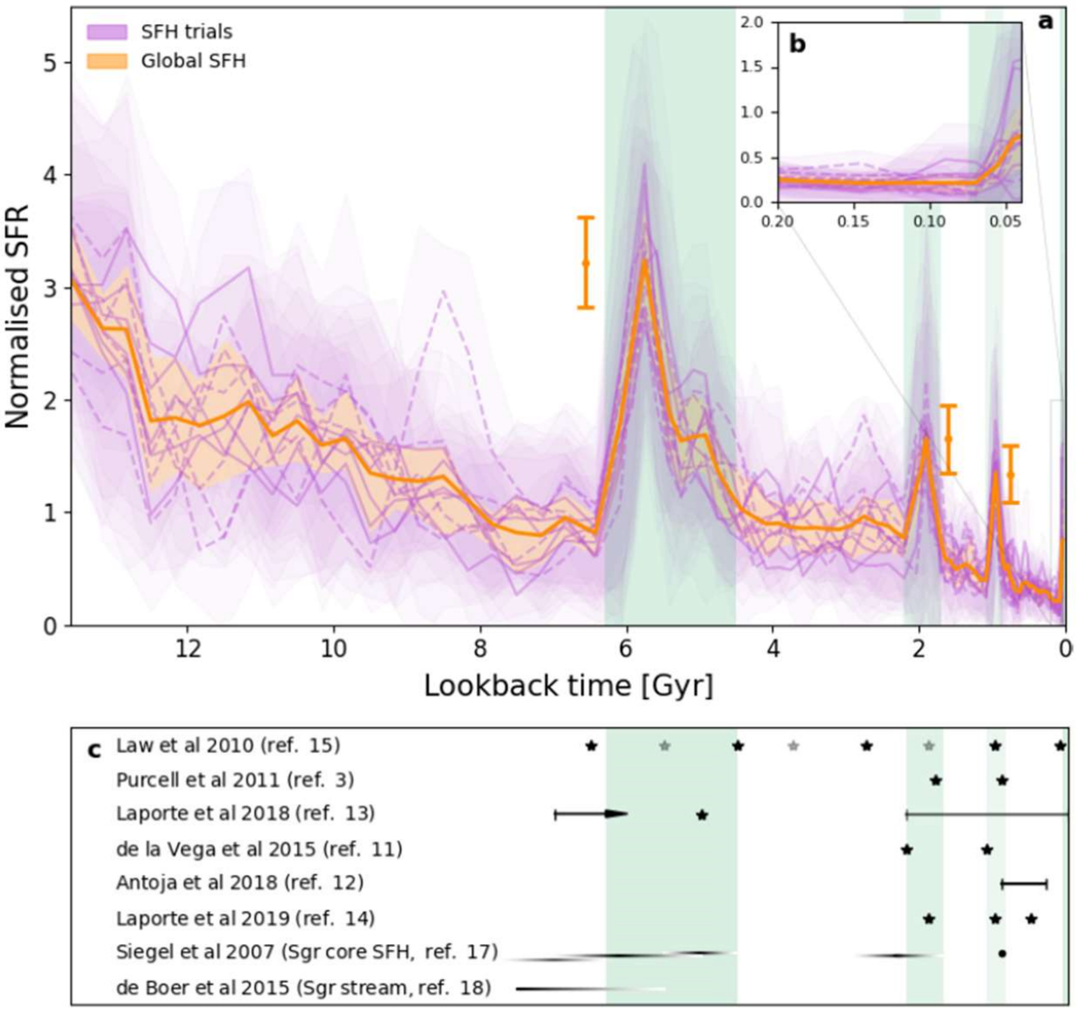

Peaks of SF
at lookback t
・5.7 Gyr
(incl. Sun format
・1.9 Gyr
・1.0 Gyr

The peaks ove
with the timings
pericentric pass
of Sgr dwarf

The orbit of Sgr dwarf

$M_{tot} \sim 2.5 \times 10^{10}\ M_{sun}$

Ruiz-Lara et al. 2020

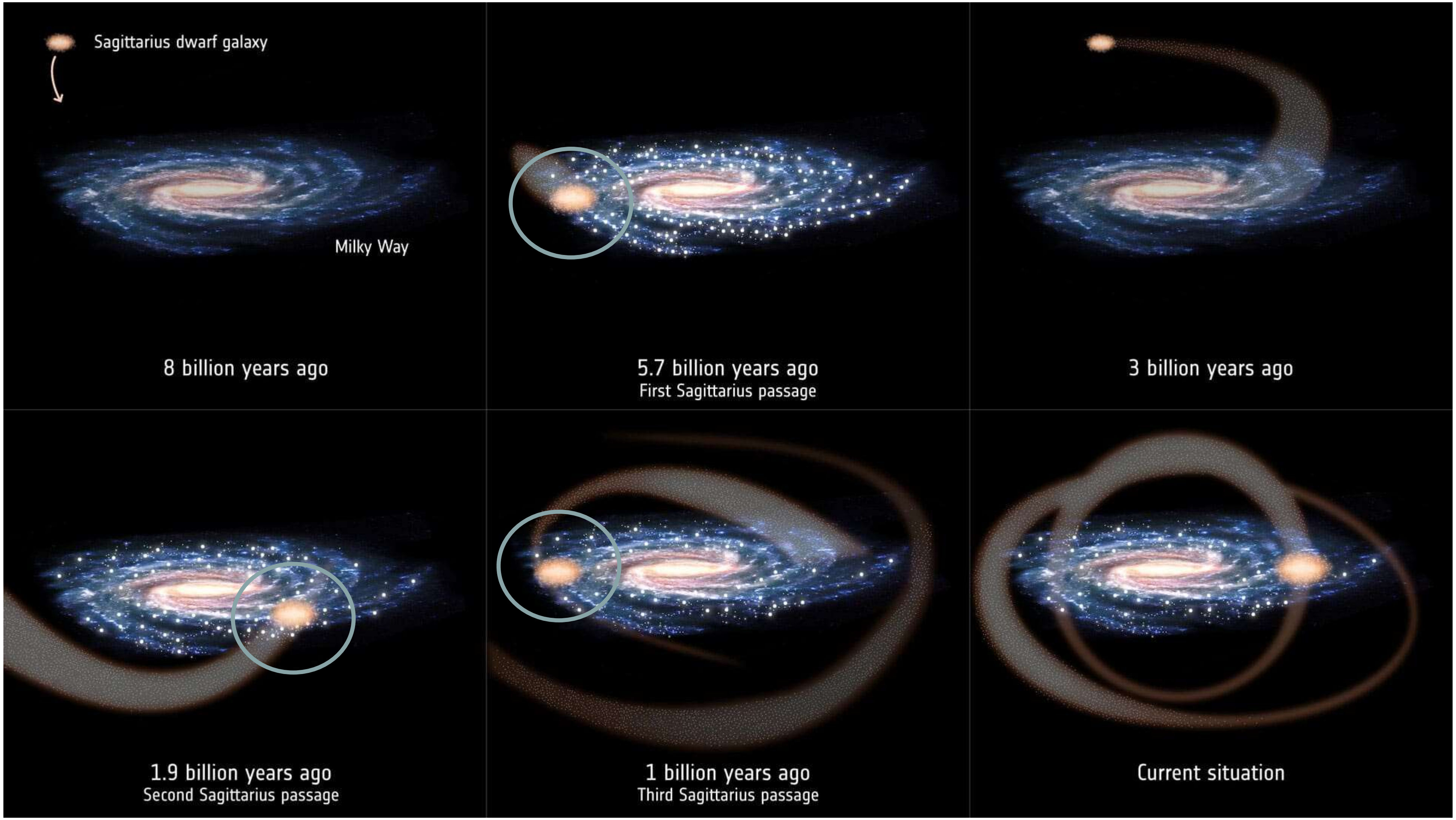

恒星系ハローのサブ構造
～階層的合体による形成の証拠～

（Belokurov et al. 2006）

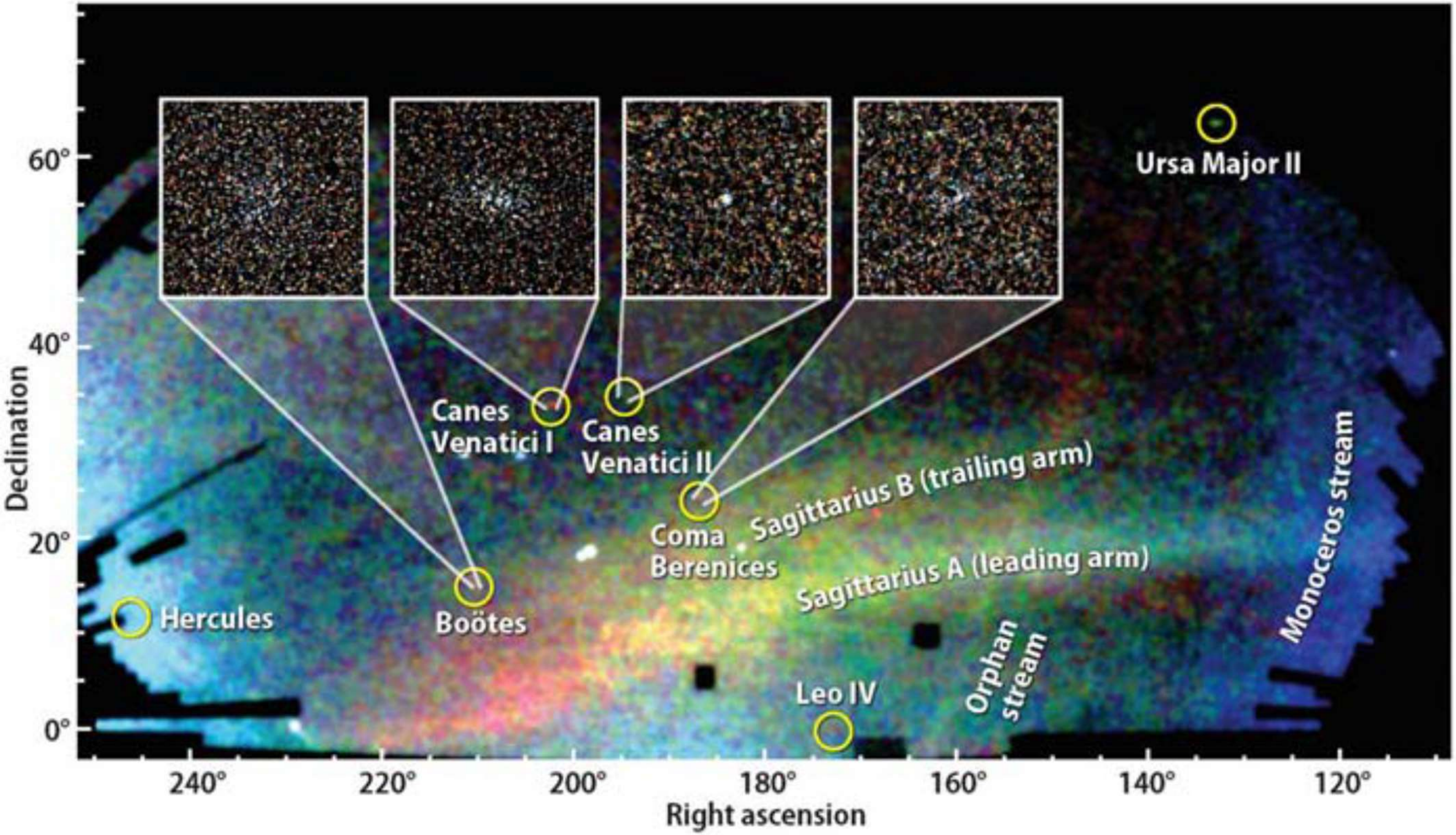

天の川と恒星ストリーム

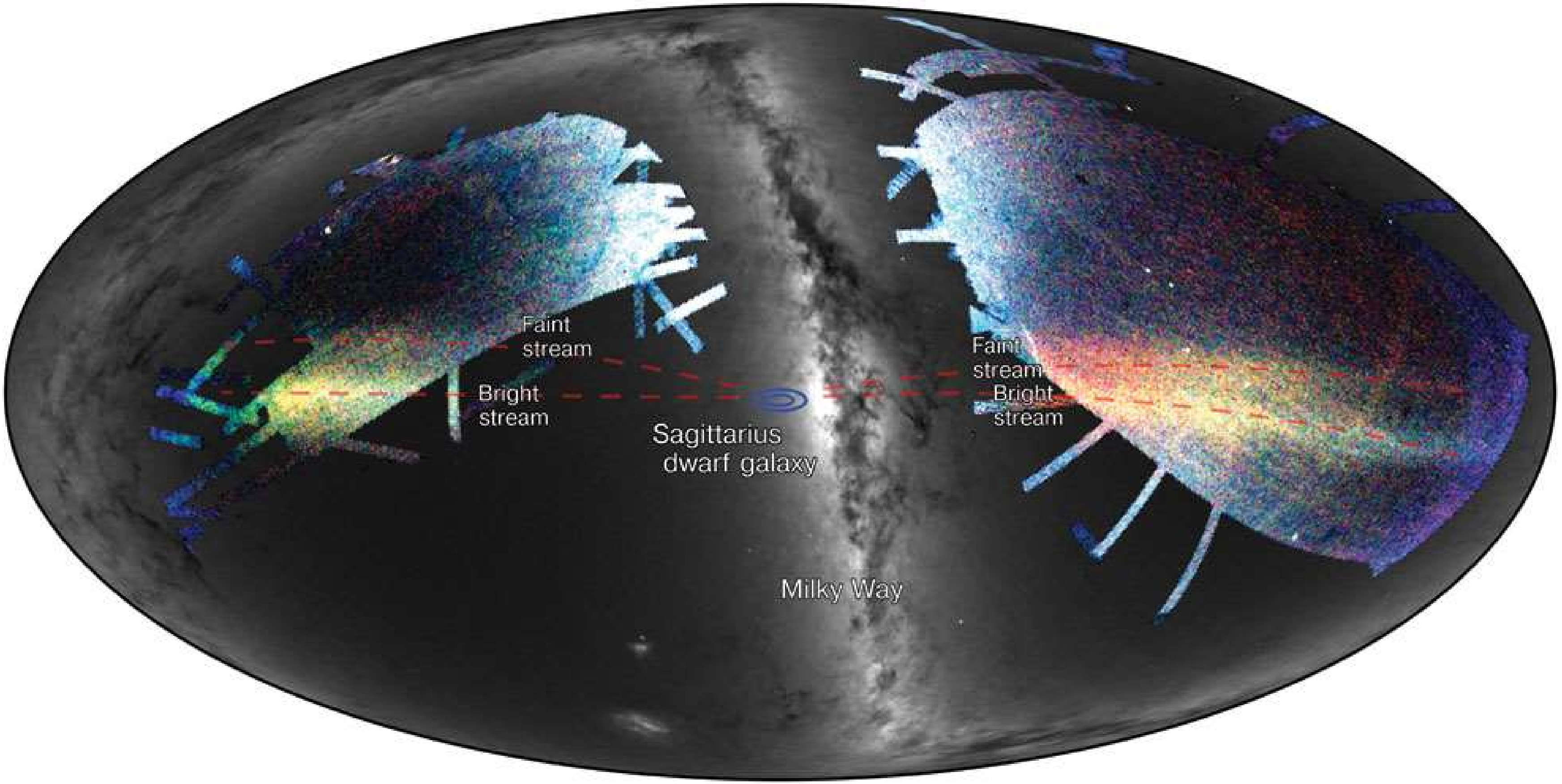

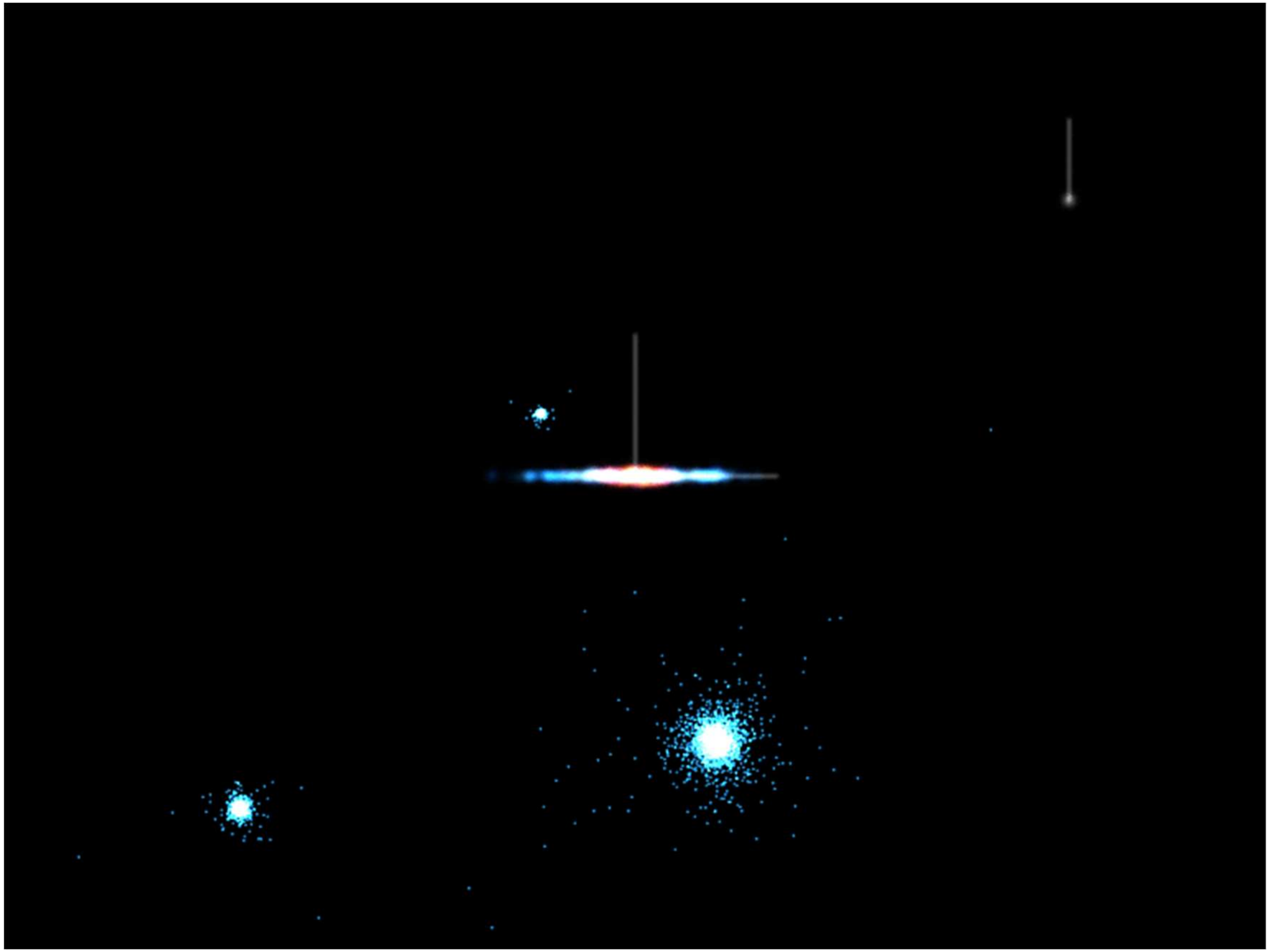

Credit: Rensselaer/Benjamin A. Willett

小銀河の潮汐崩壊と残骸分布

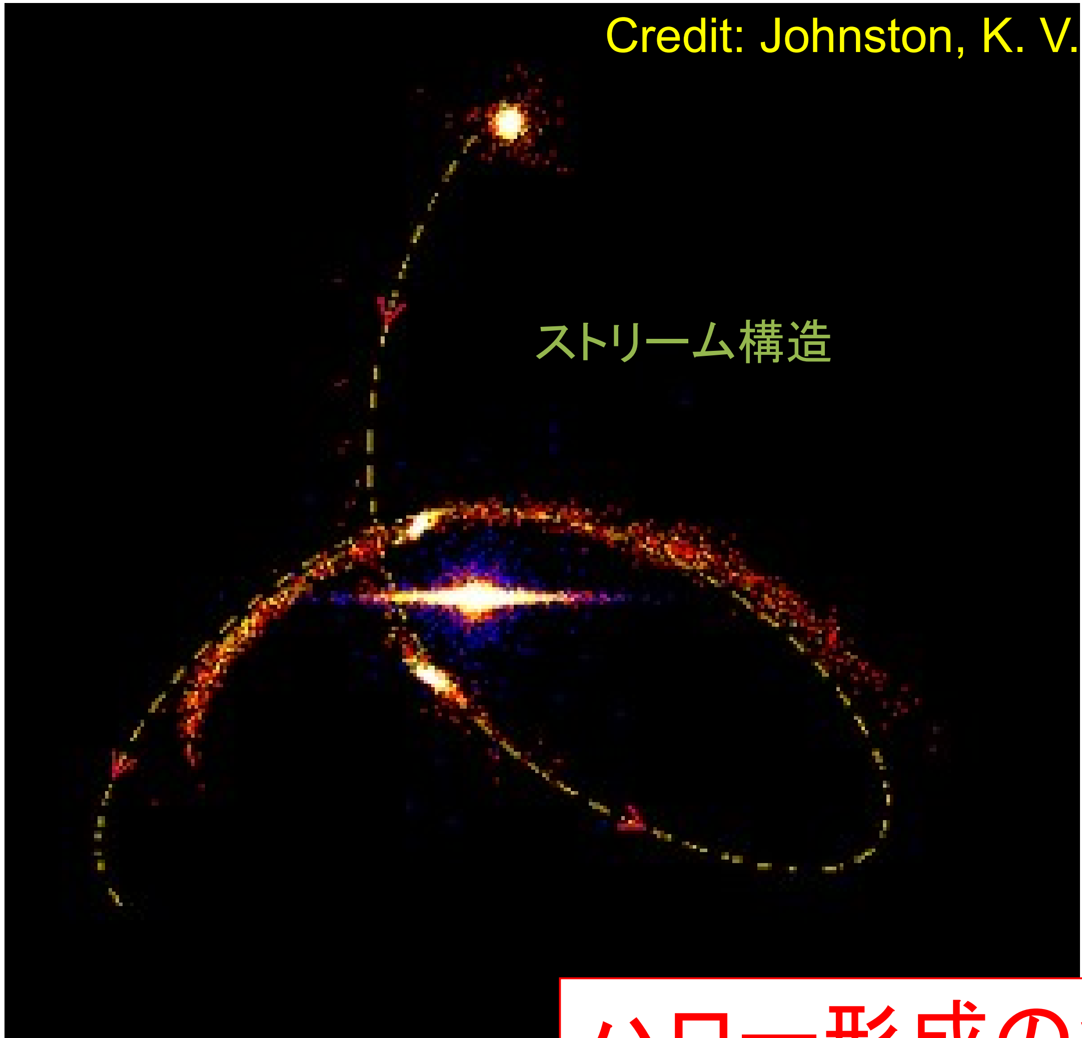

ハロー形成の痕跡

銀河形成シミュレーションによる
恒星系ハローの空間分布

～ハロー合体史の違い～

Cooper et al. 2010

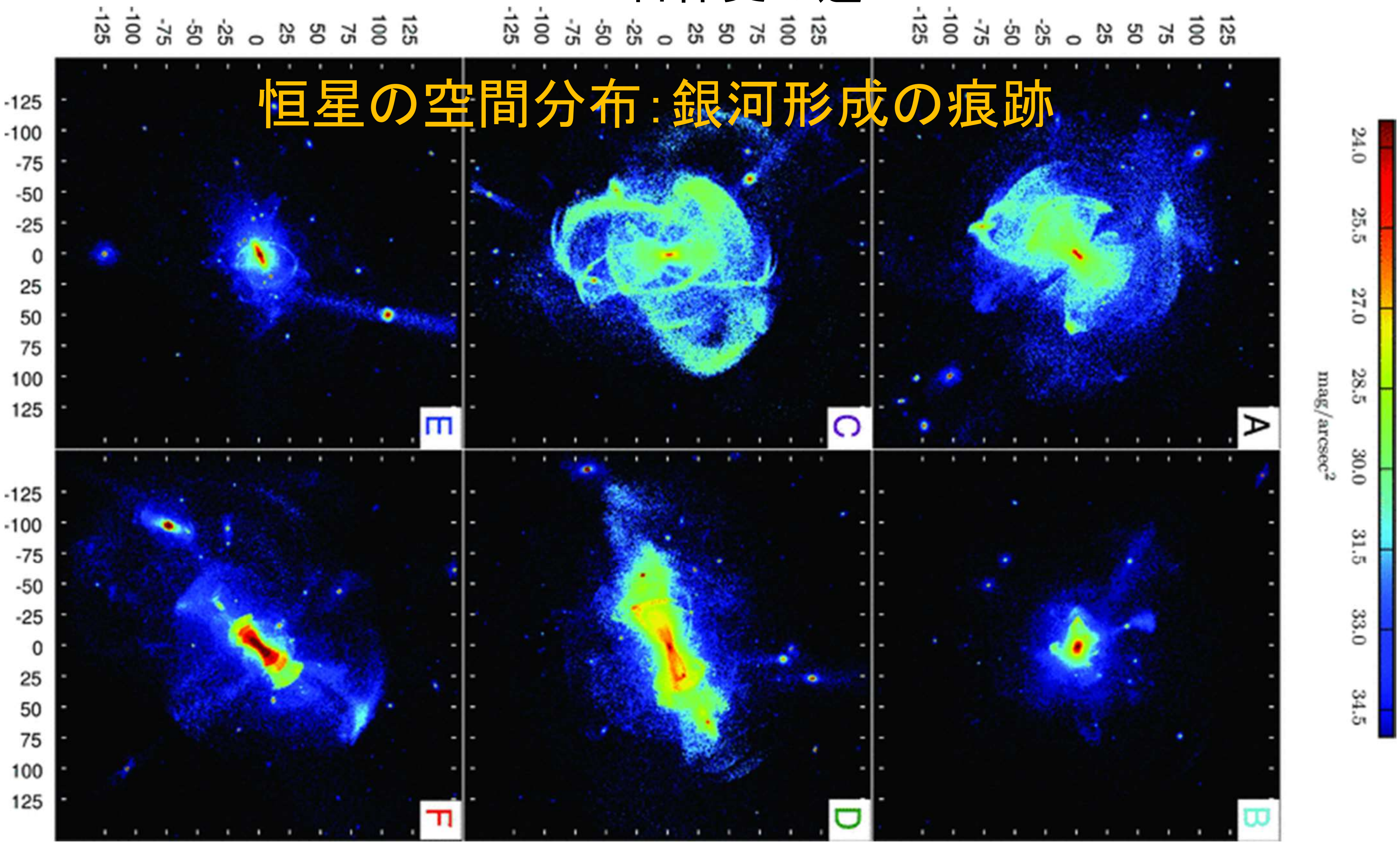

マゼラン雲に関する新展開

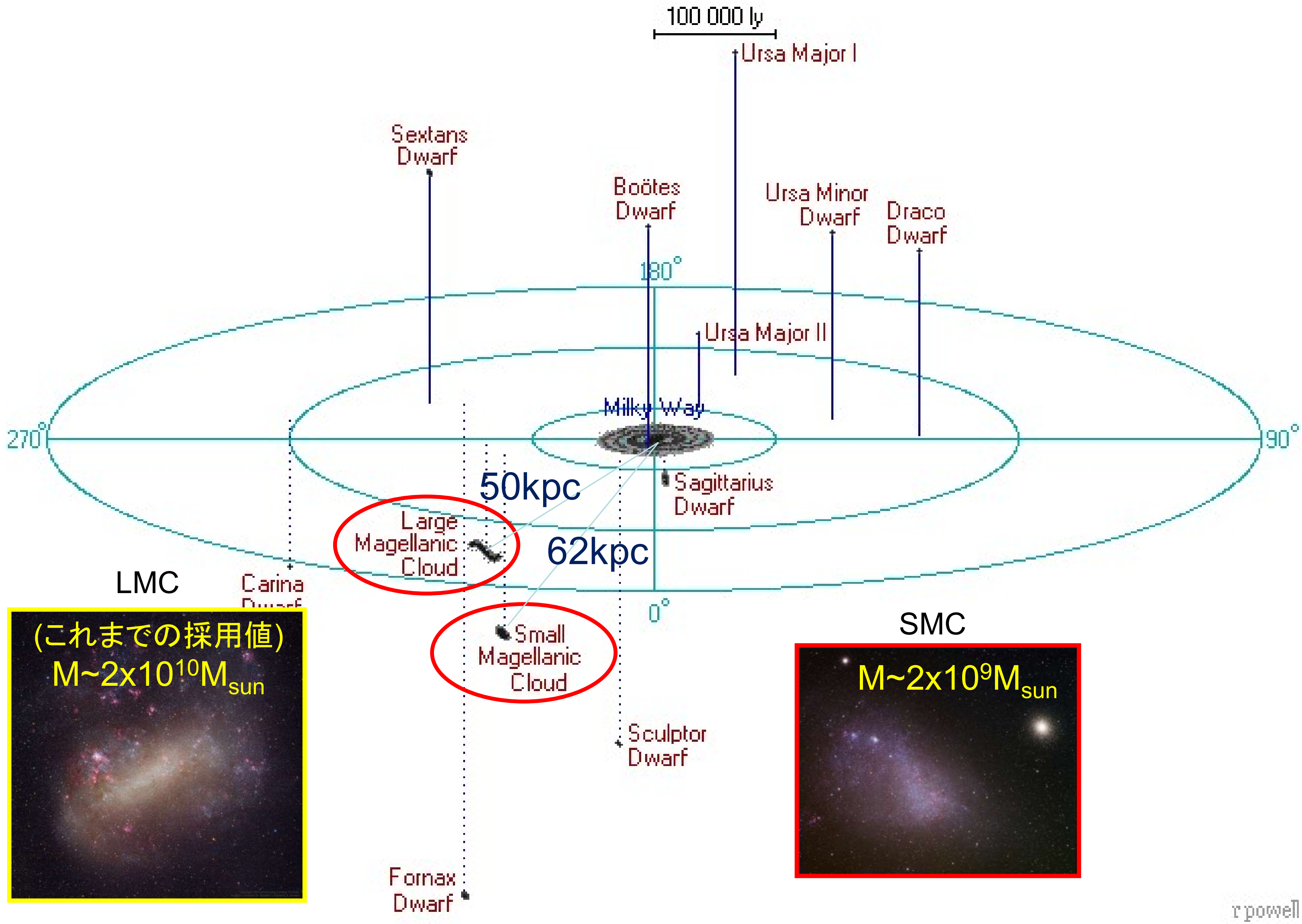

LMC/SMC's orbit

Recent several works (Gaia, HST) suggest
the first infall of LMC/SMC

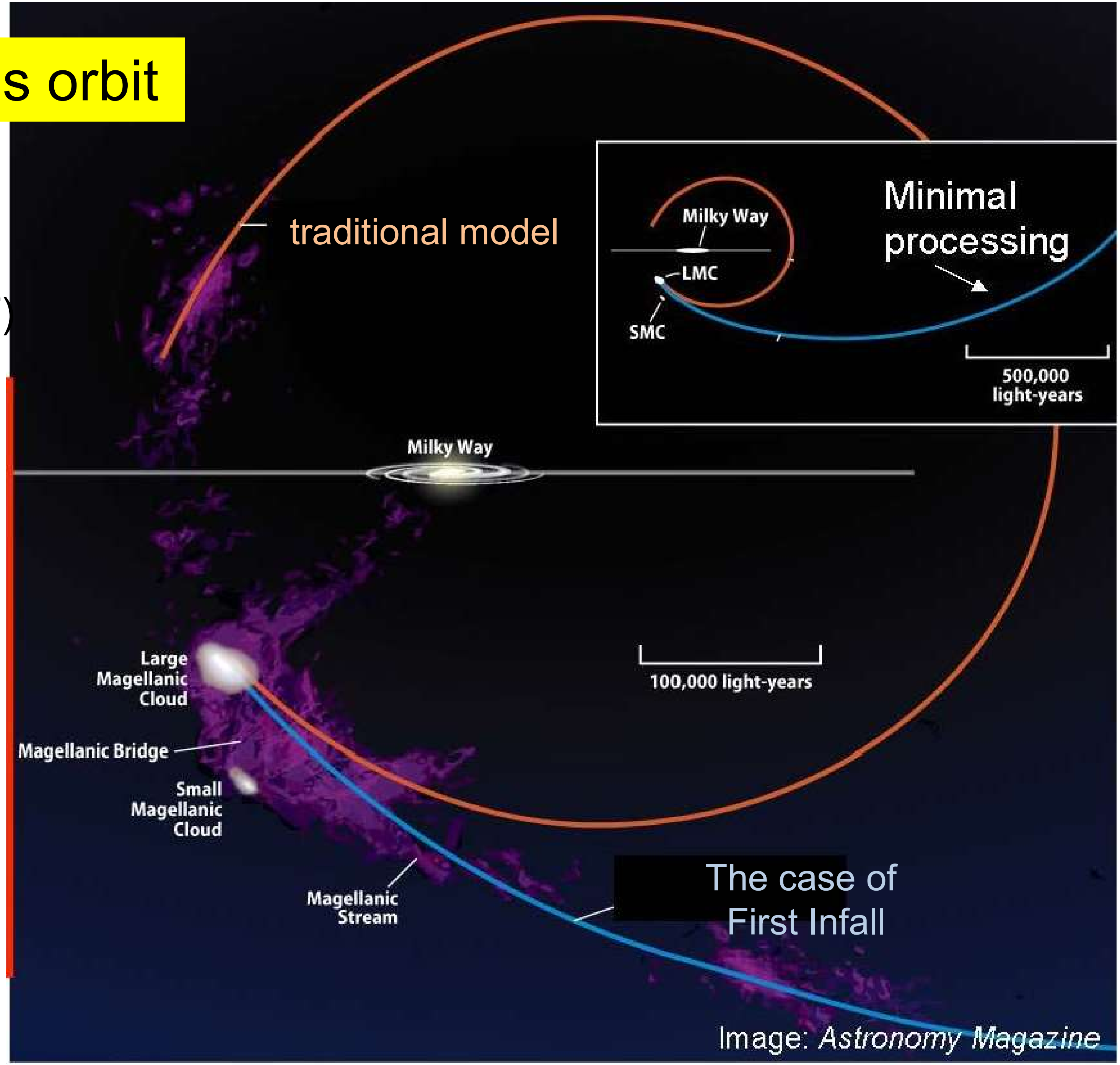

Besla+ 2010

Misaligned Orphan Stream
~effect of the very massive LMC?~

Erkal et al. 2019 (using Gaia DR2 PMs)

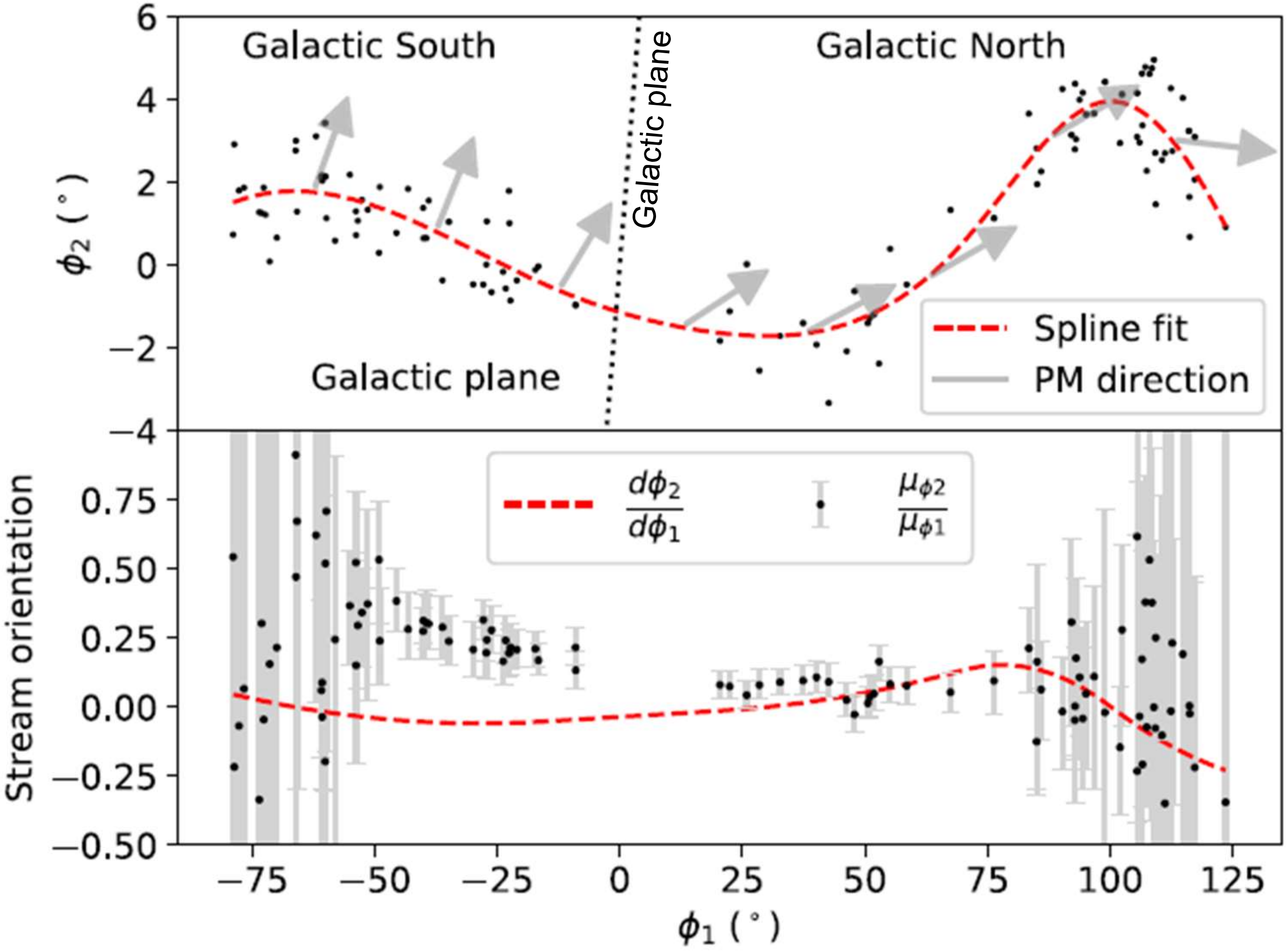

Points:
RR Lyrae
along OS

Misaligned Orphan Stream ~effect of the very massive LMC?~

Erkal et al. 2019 (using Gaia DR2 PMs)

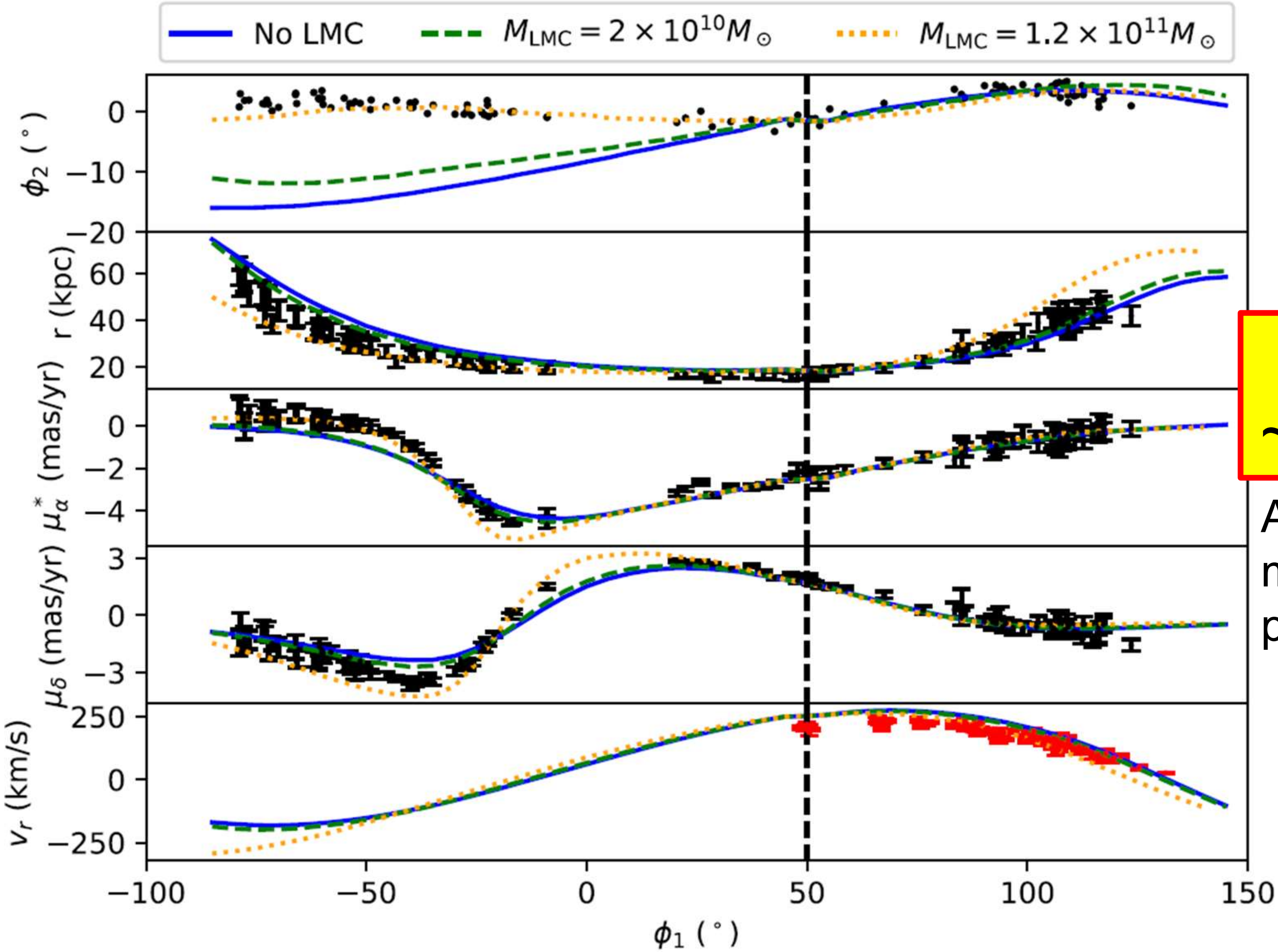

Best fit M_{LMC} ~ 1.38×10^{11} M_{sun}

An order of magnitude more massive than previously thought!

もしもLMCの質量が銀河系の総質量の1/10もあったら

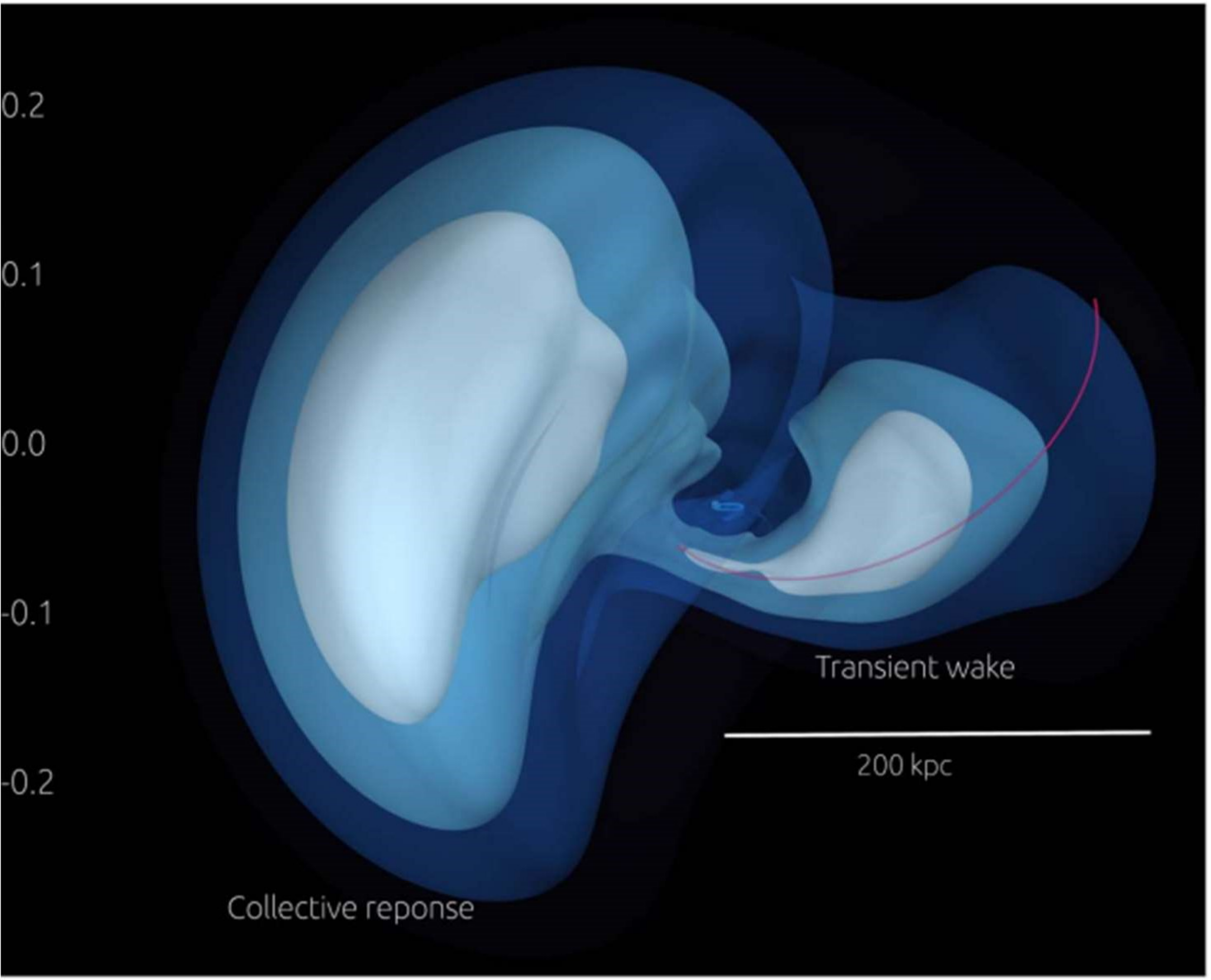

LMC-induced DM dynamical friction wake and collective response in the MW DM halo at the present day, in the Galactocentric YZ plane. The density computed using the BFE for the MW's DM halo. The color bar shows the density contrast as defined in Equation (6). White contours represent the while the darker blue contours show the underdensities. The dynamical friction wake is a large-scale structure ranging from ~50 kpc, near the LMC (red the edge of the halo. The Collective Response is the larger overdensity that appears predominantly north of the MW disk (the latter is marked by the llipse). The Collective Response also appears to the south of the MW disk, at large distances. The red line marks the past passage of the LMC, which tion of the dynamical friction wake. A 3D animated rendering of the density field of the MW illustrating the halo response to the LMC's passage, can be neo https://vimeo.com/5462071170 and in the online Journal. The animated rendering rotates around the YZ plane, which is perpendicular to the (XY).

銀河系暗黒物質の分布が大きくゆがむ

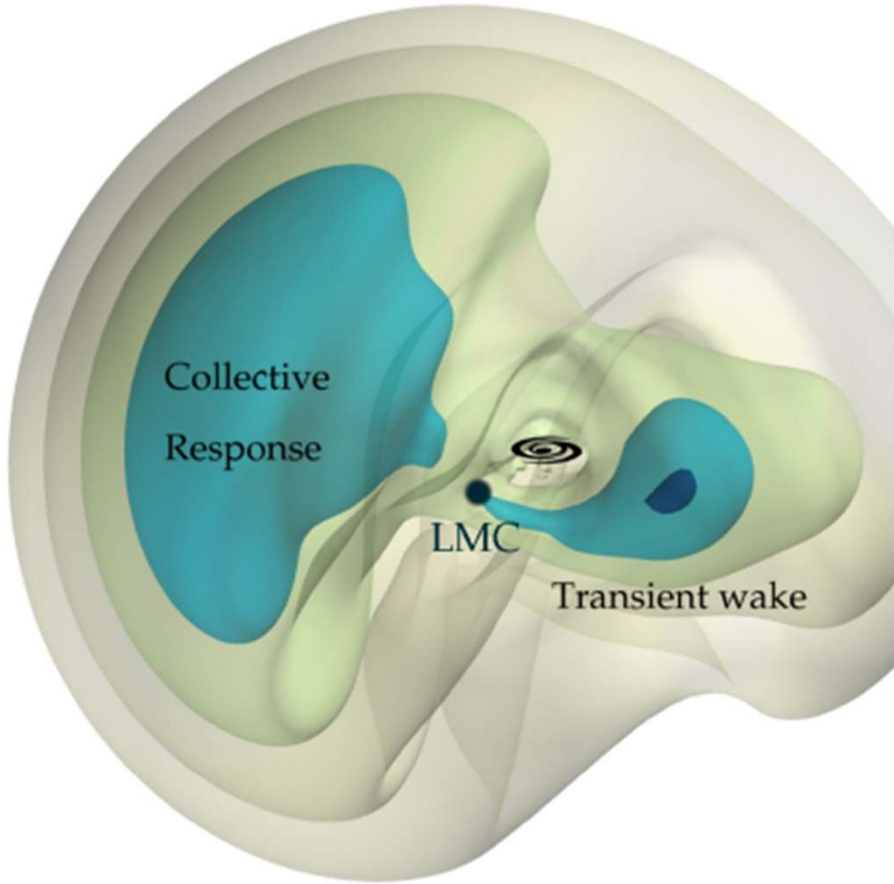

Garavito-Camargo et al. 2021

4.3 楕円銀河の光度･色進化

Stellar Population Model
Worthey 1994, ApJS, 95, 107

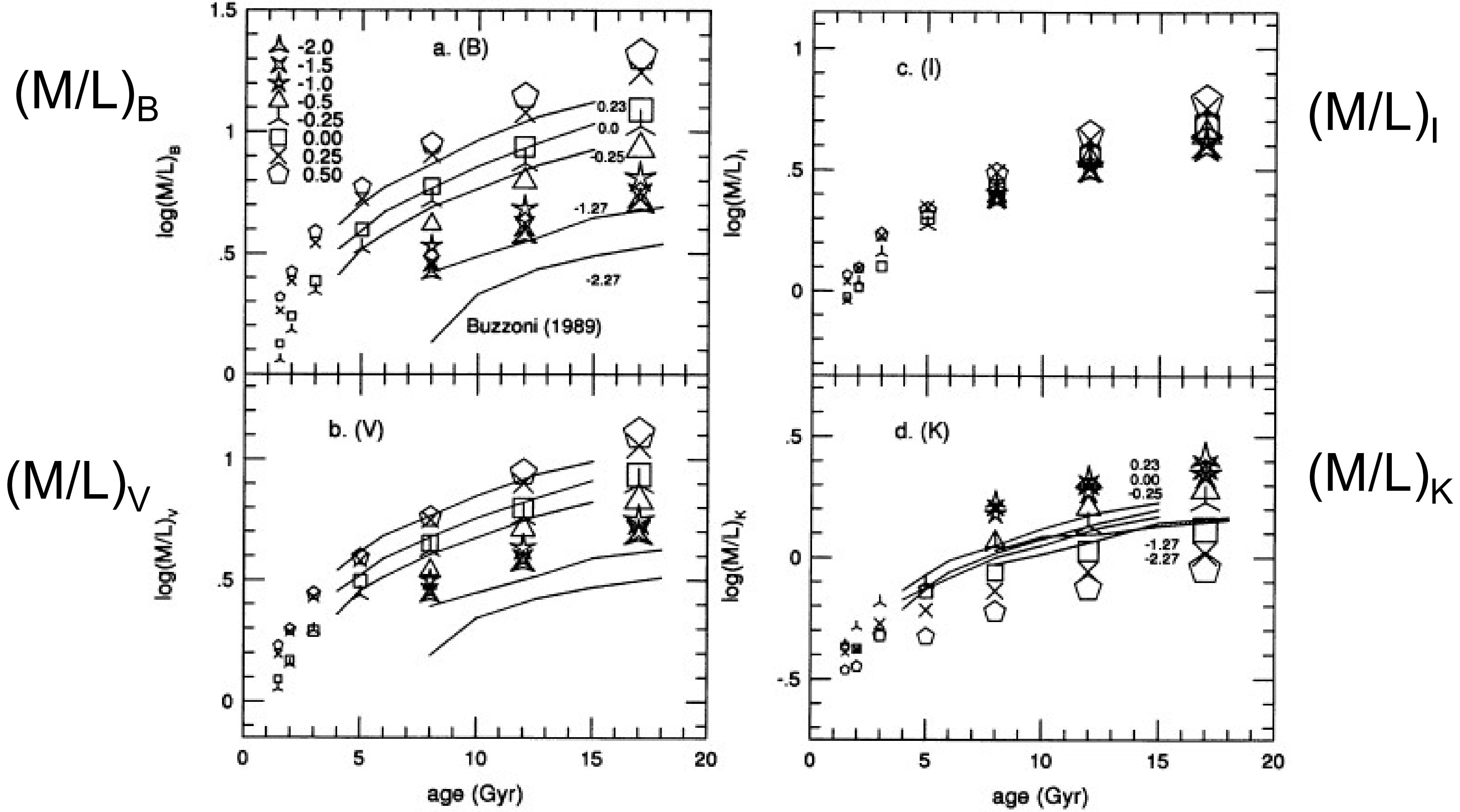

FIG. 32.—Mass-to-light (M/L) ratios as a function of age, for all metallicities for four passbands. [Fe/H] is coded by symbol in (a). All panels show the same vertical span. Except for the I_C band, predictions from the red clump models of Buzzoni (1989) are also shown as solid lines, labeled by [Fe/H] in (a) and (d). The dependence of M/L on metallicity *reverses* in sense around the *I*-band. That is, more metal-rich populations are dimmer in *UBV* but brighter in *JHK*, and there is a passband a little redward of I_C which has a luminosity *approximately independent of metallicity.*

楕円銀河の進化モデル
(Worthey 1994)

年齢固定

金属量固定

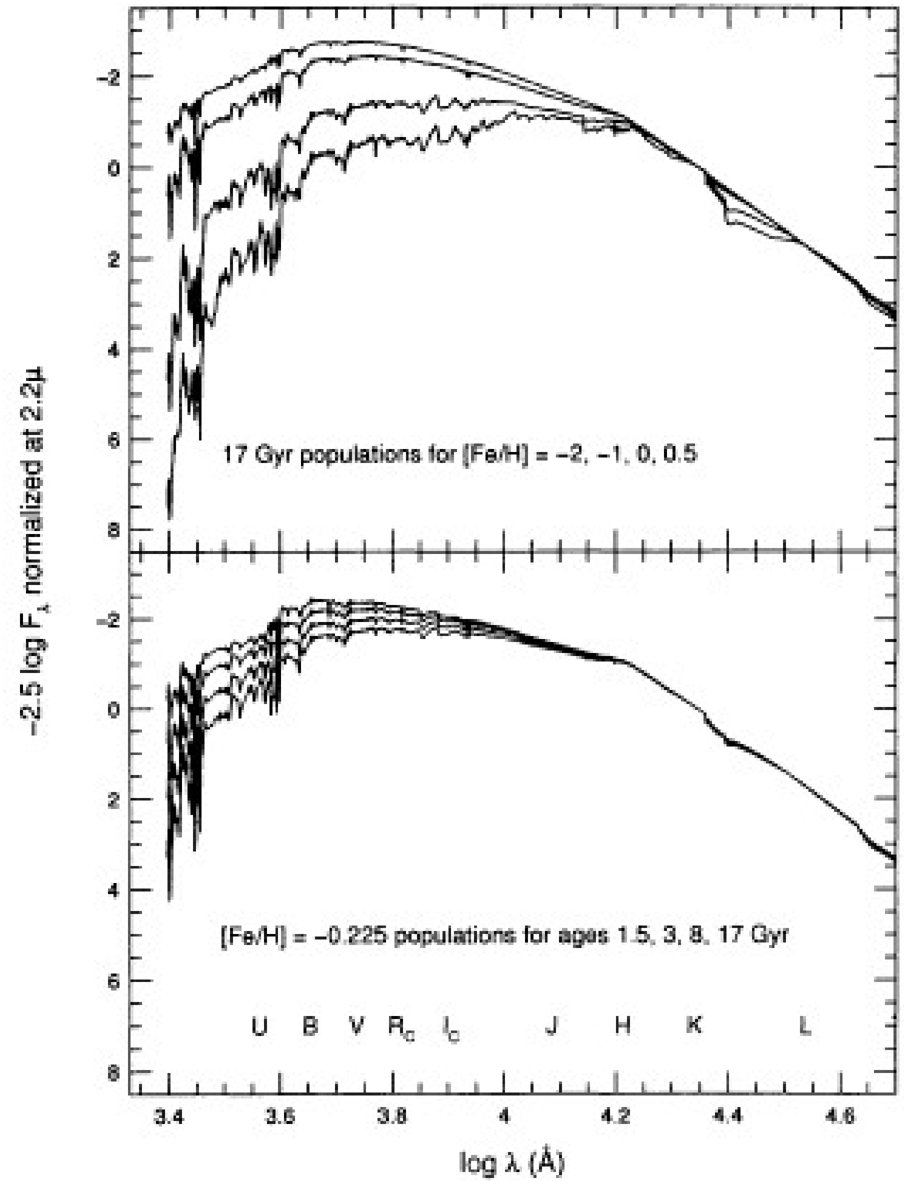

FIG. 38.—(*a*) Spectral energy distributions (SEDs) for 17 Gyr populations of [Fe/H] = −2, −1, 0, and 0.5 dex. Note that the presence of M stars leaves a strong signature in the optical red. (*b*) SEDs for [Fe/H] = −0.225 populations of ages 1.5, 3, 8, and 17 Gyr. The vertical scale is in magnitudes of F_λ, normalized to zero at 2.2 μm. Approximate locations of broadband filters are marked in (*b*).

スペクトルに対する恒星種類の寄与

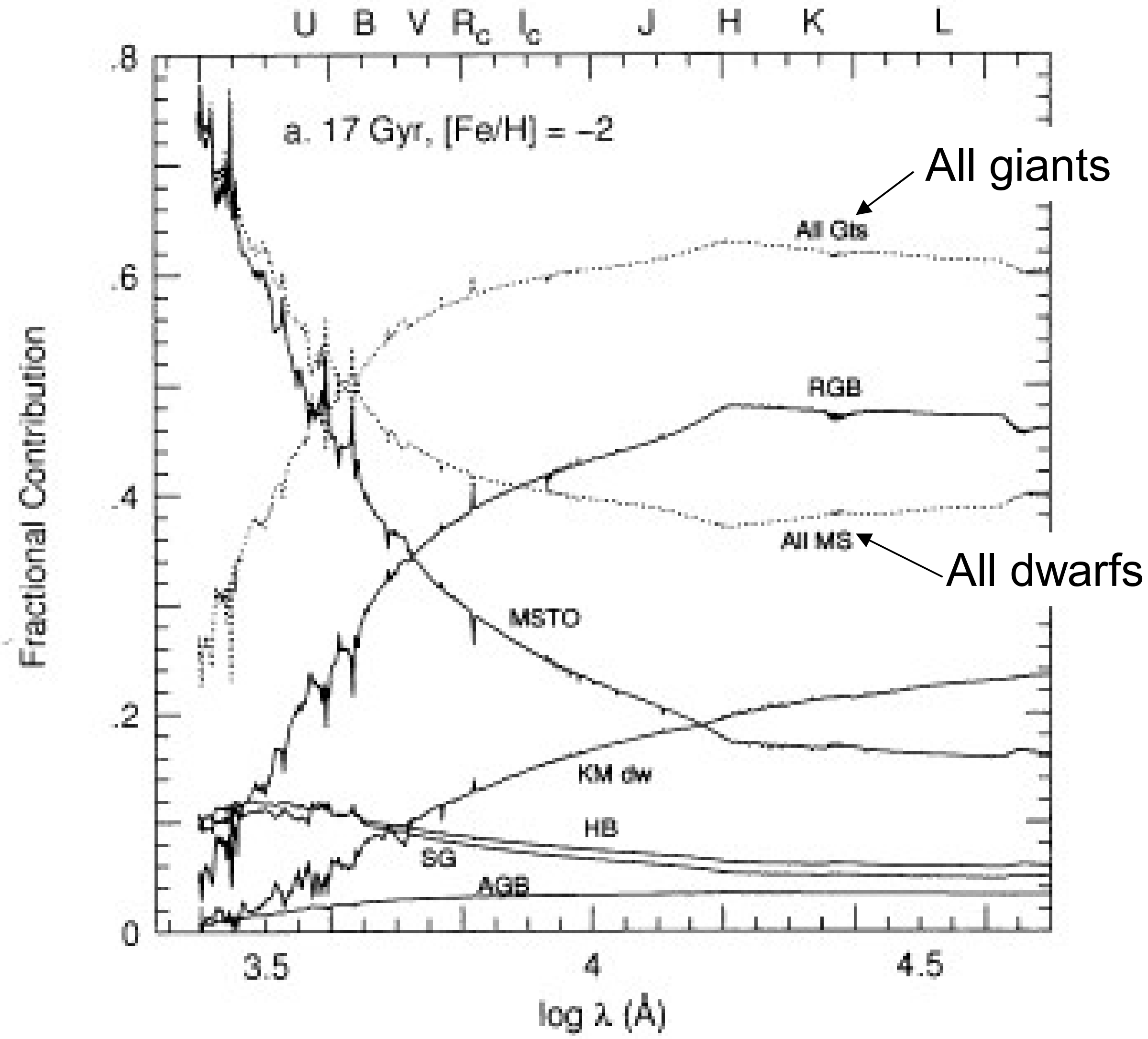

最新の（E銀河の）SEDモデル
（Bruzual & Charlot 2003, MN, 344, 1000）

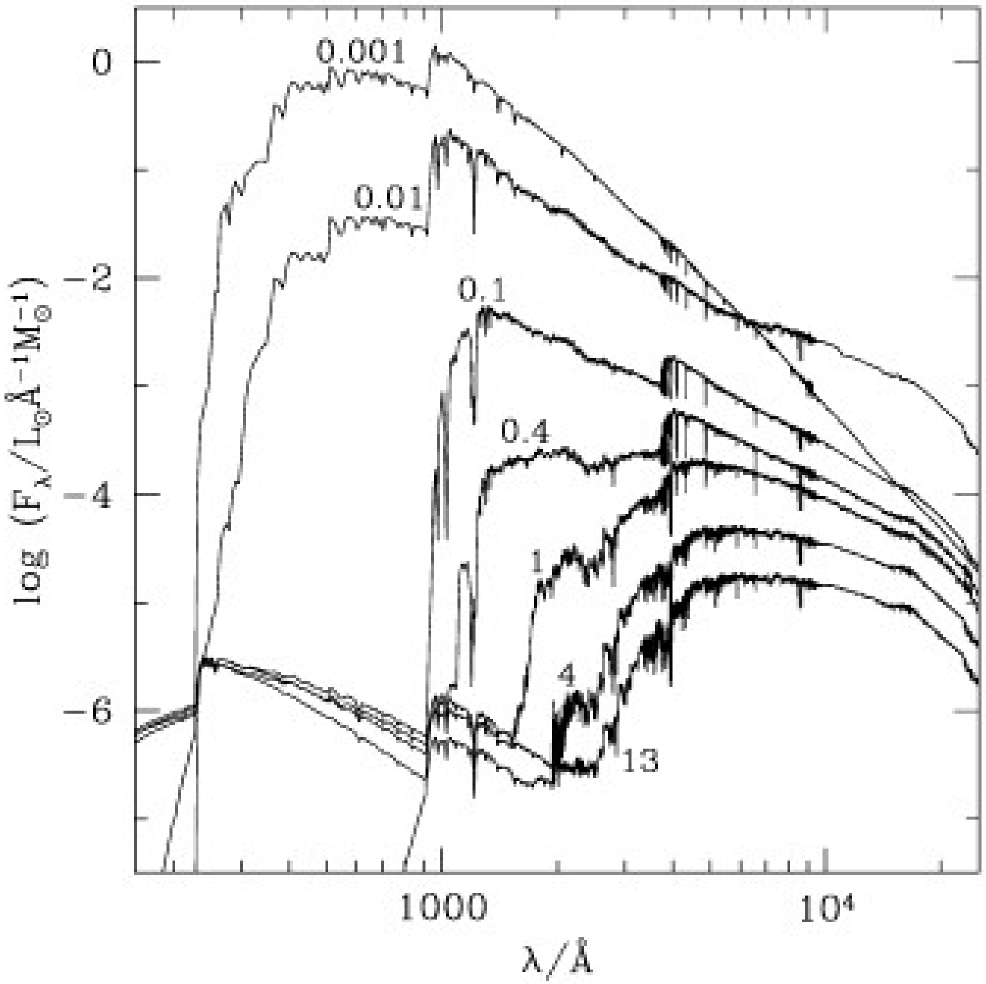

Figure 9. Spectral evolution of the standard SSP model of Section 3 for the solar metallicity. The STELIB/BaSeL 3.1 spectra have been extended blueward of 3200 Å and redward of 9500 Å using the Pickles medium-resolution library. Ages are indicated next to the spectra (in Gyr).

Galactic Wind Model (Yoshii & Arimoto 1987, AA, 188, 13)

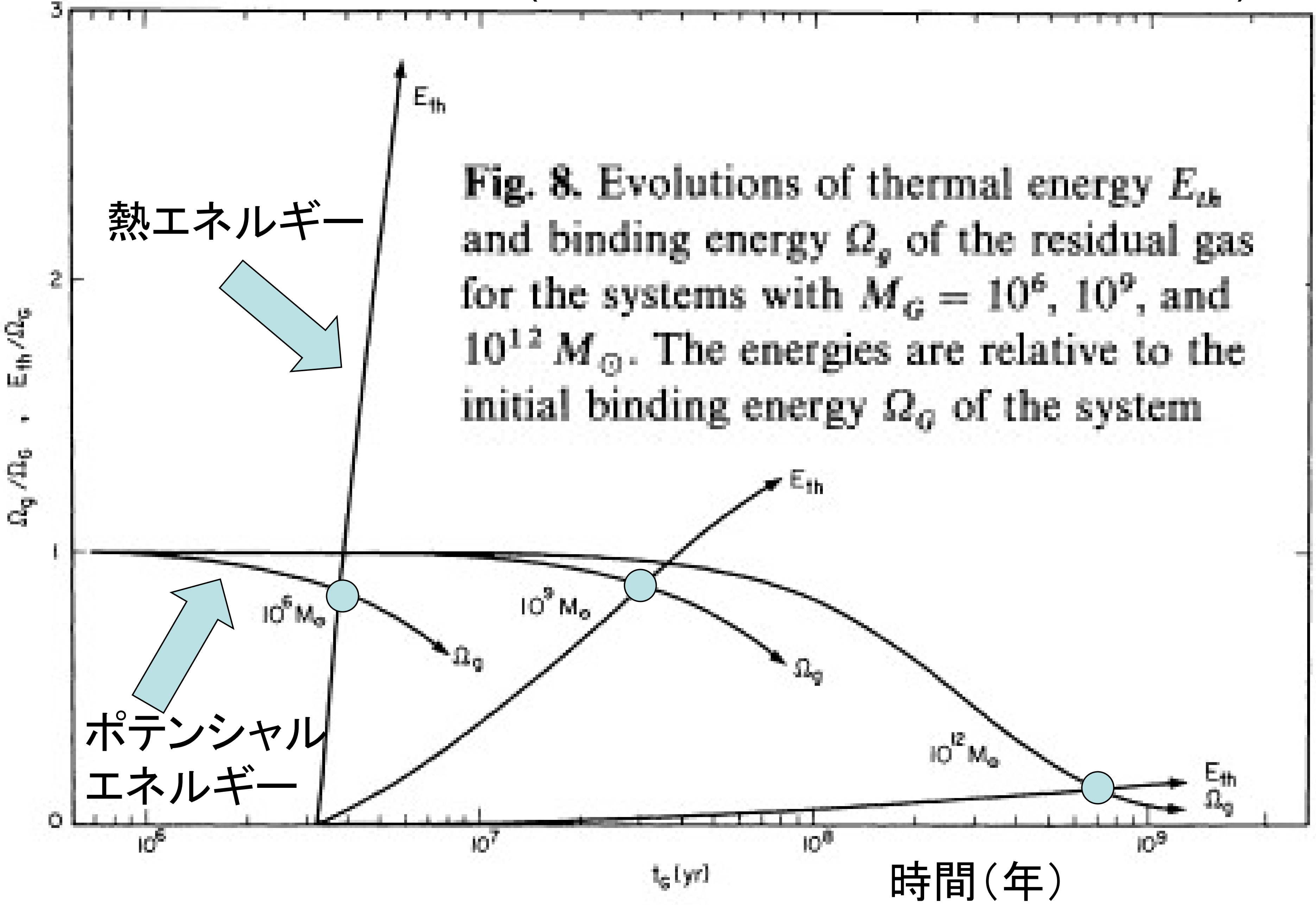

Fig. 8. Evolutions of thermal energy E_{th} and binding energy Ω_g of the residual gas for the systems with $M_G = 10^6$, 10^9, and $10^{12}\ M_\odot$. The energies are relative to the initial binding energy Ω_G of the system

流出する
ガスの割合

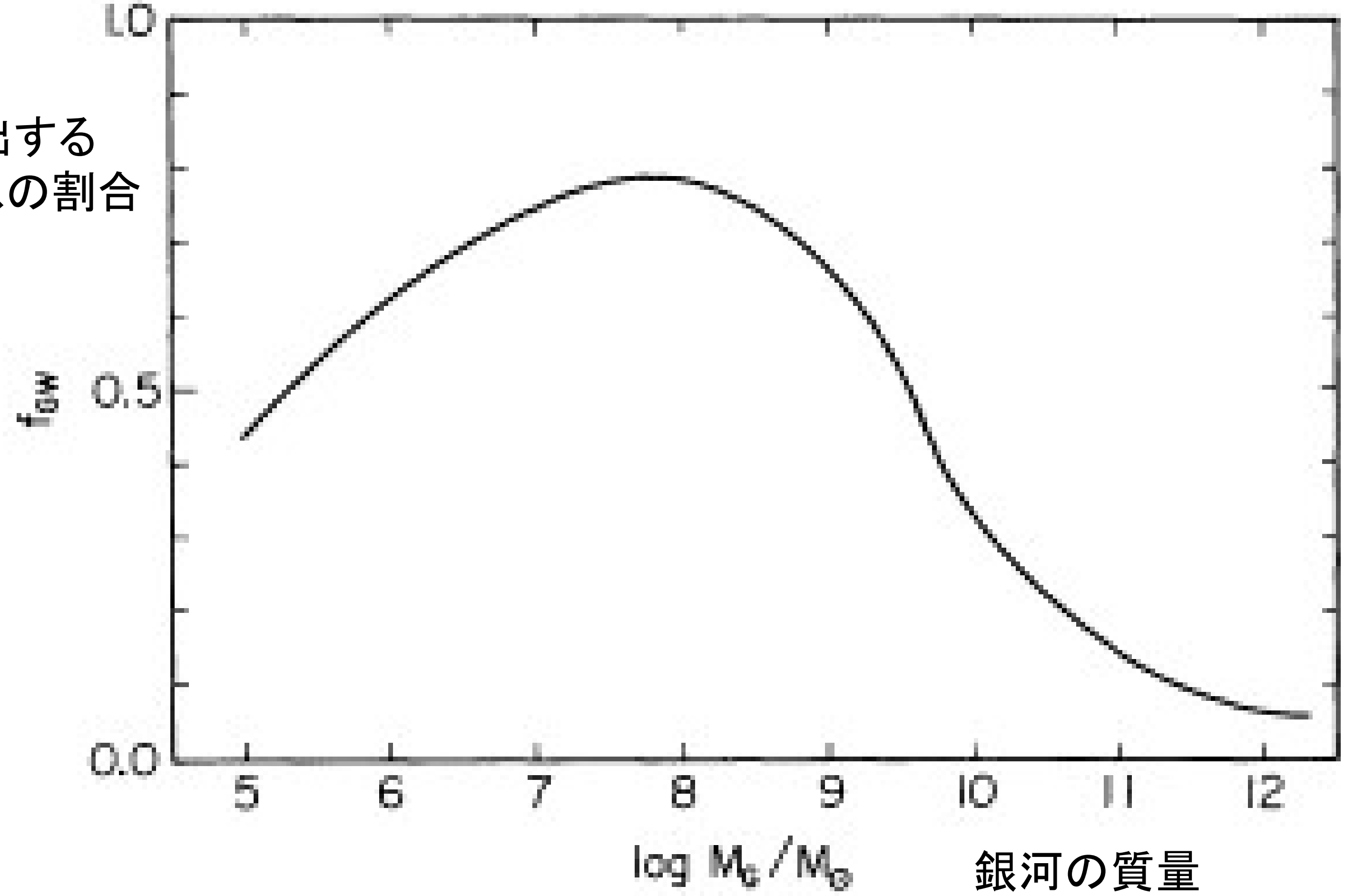

銀河の質量

Fig. 7. Fractional mass of the residual gas f_{GW} at the epoch of occurrence of a galactic wind t_{GW} plotted against the initial mass M_G of the system

銀河風が
吹く時刻
（年）

流出するガス
の金属量

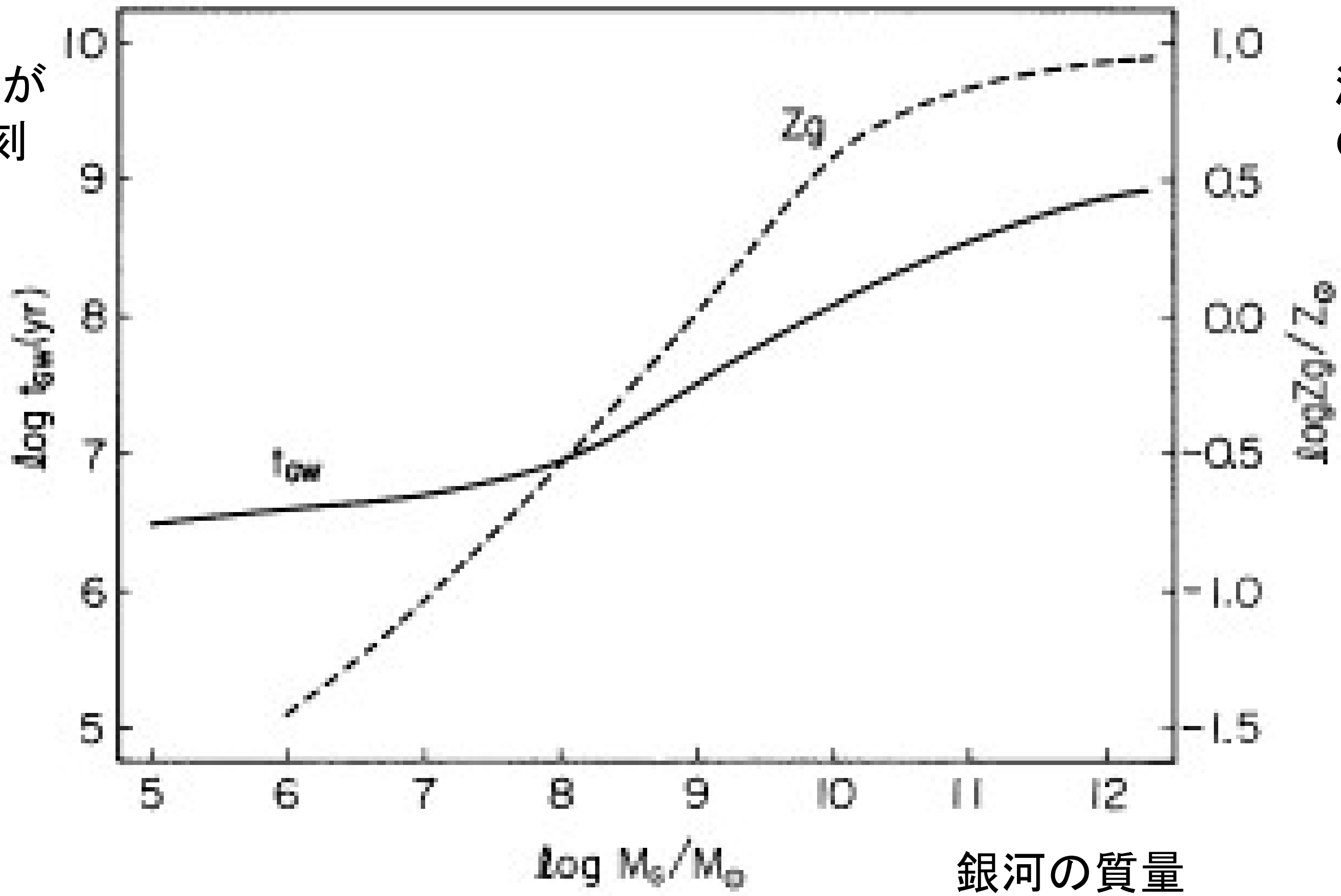

銀河の質量

Fig. 1. Epoch of occurrence of a galactic wind t_{GW} and metallicity of the residual gas Z_g plotted against the initial mass M_G of the system

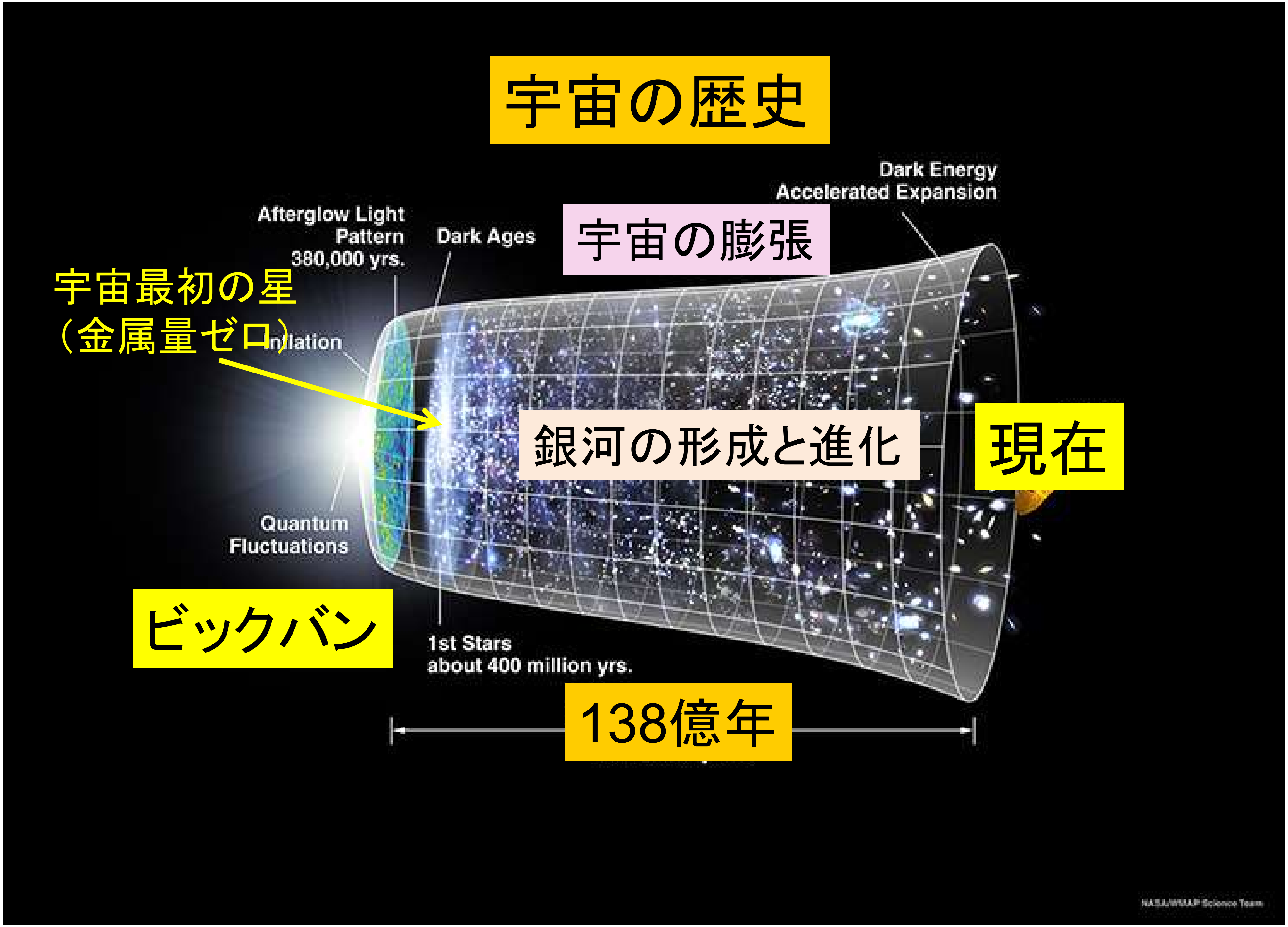

宇宙の歴史
Dark Energy
Accelerated Expansion
宇宙の膨張
Afterglow Light
Pattern
380,000 yrs.
Dark Ages
宇宙最初の星
（金属量ゼロ）
Inflation
銀河の形成と進化
現在
Quantum
Fluctuations
ビックバン
1st Stars
about 400 million yrs.
138億年
NASA/WMAP Science Team

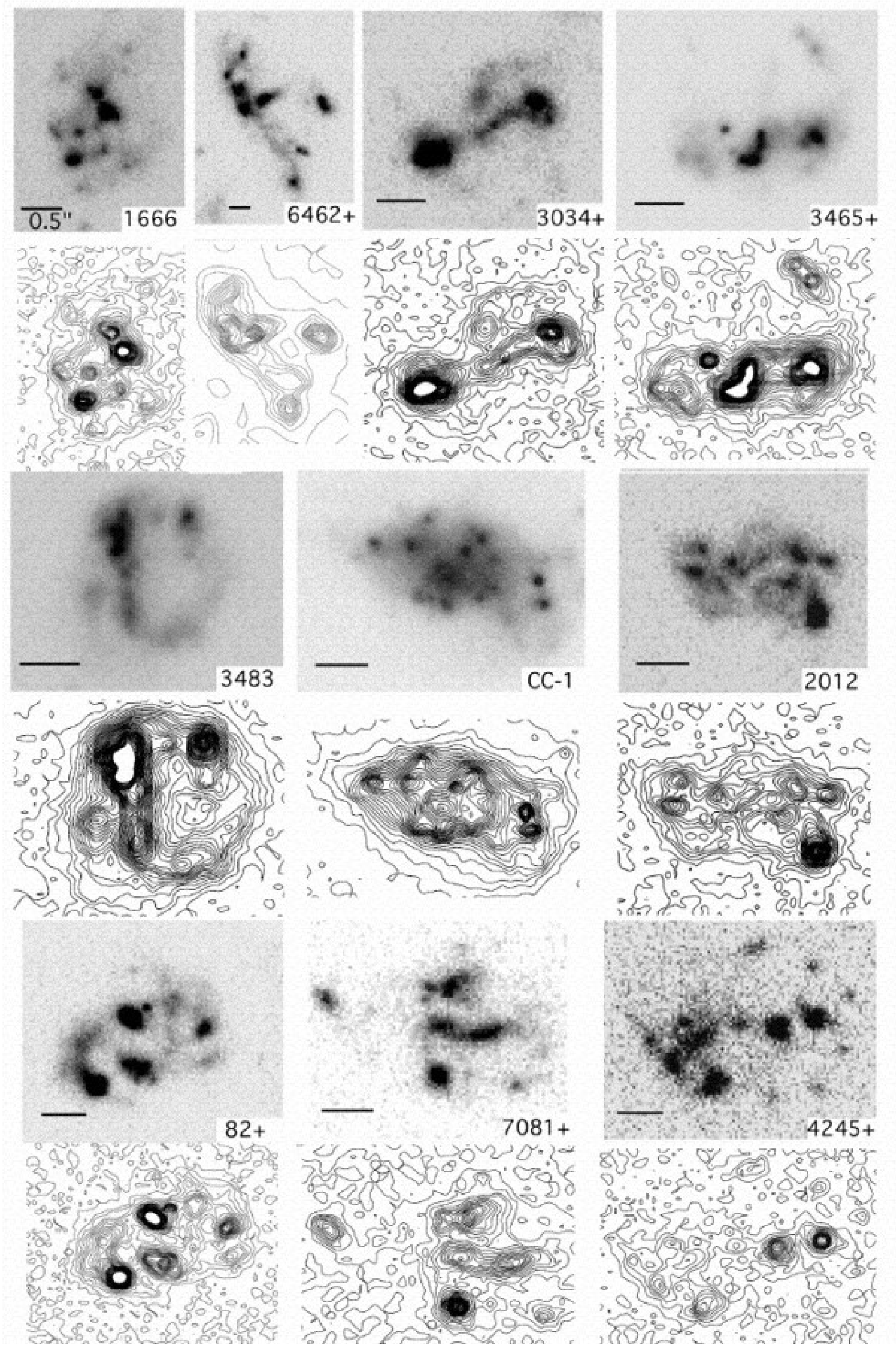

赤方偏移が1.6から3の遠方にある銀河の画像

不規則な形、クランプ状の小さな銀河の集まりが多い
⇒銀河の形成途中

Elmegreen & Elmegreen 2005

様々な観測から求められた宇宙における星形成史

Madau & Dickinson (2014)

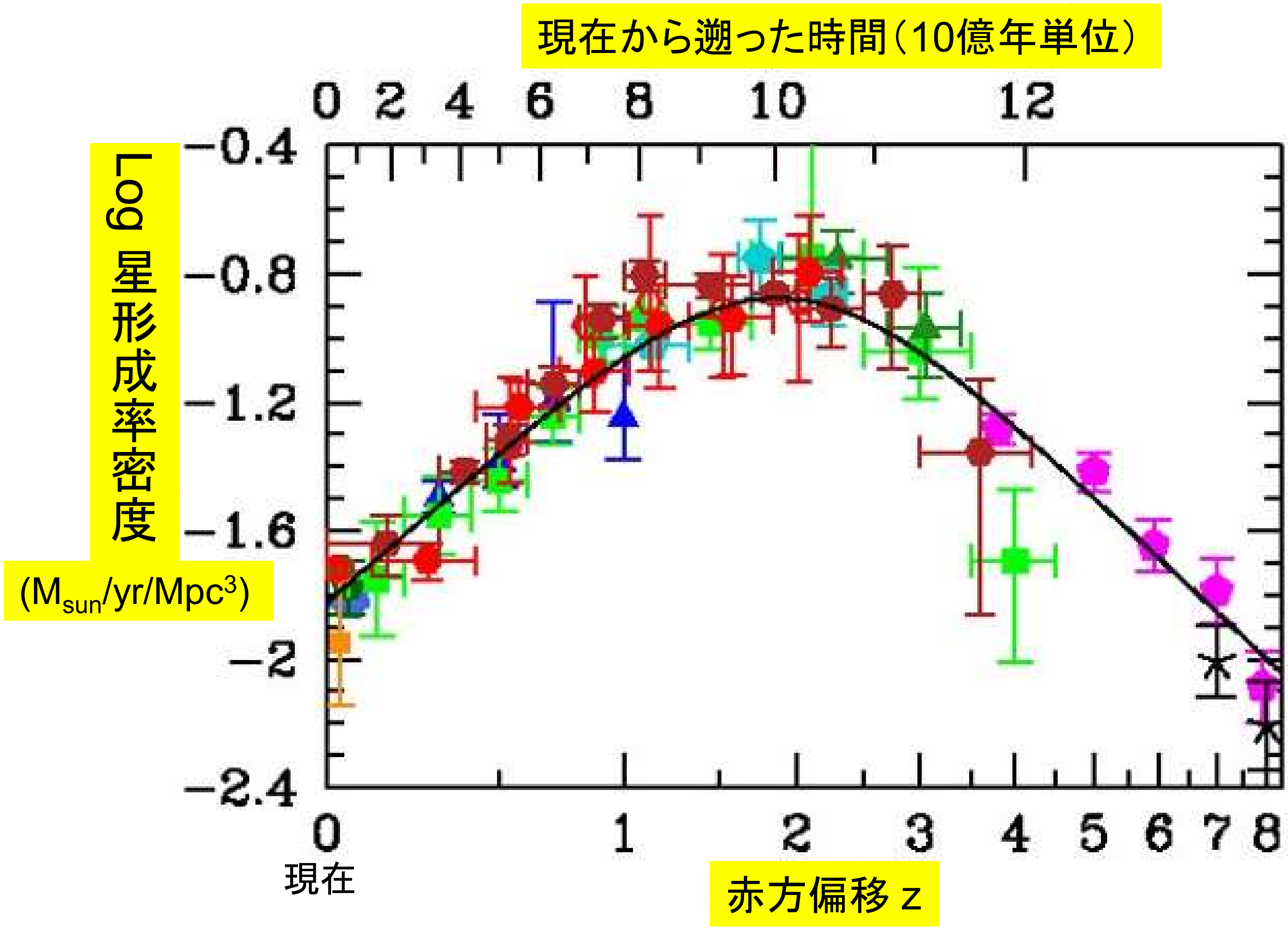

銀河形成のダウンサイジング

重い銀河ほど早く形成される証拠

z=0の銀河の年齢(SDSS)
Kauffnann et al. (2005)

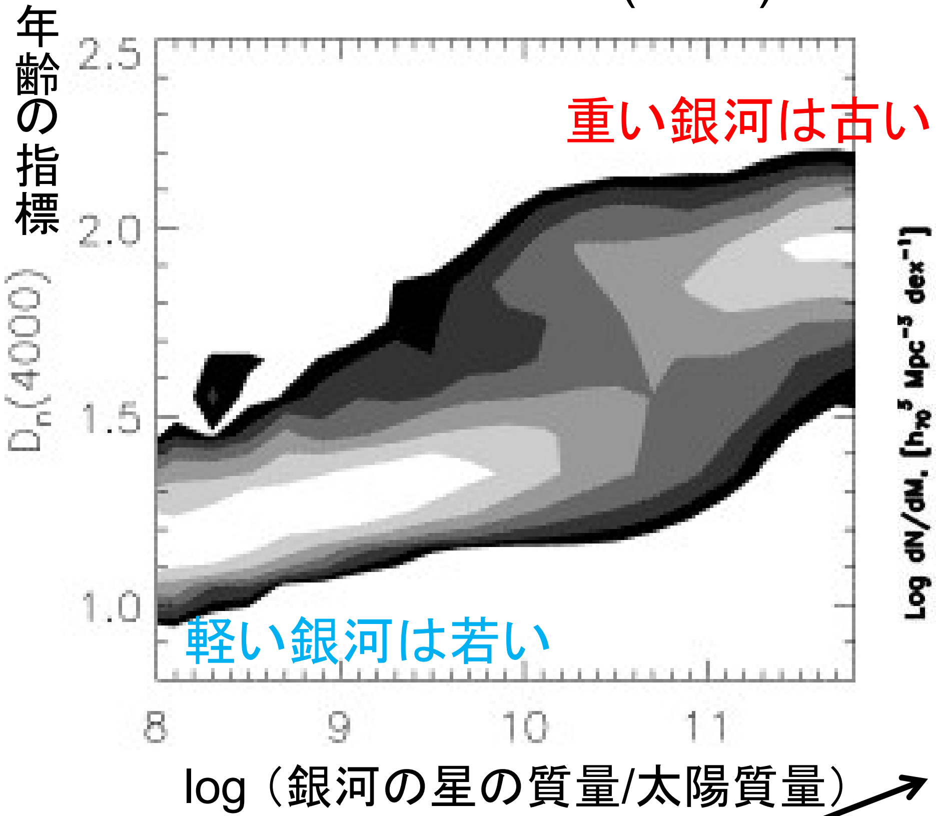

0.4<z<1.4の銀河の質量関数(DEEP2)
Bundy et al. (2006)

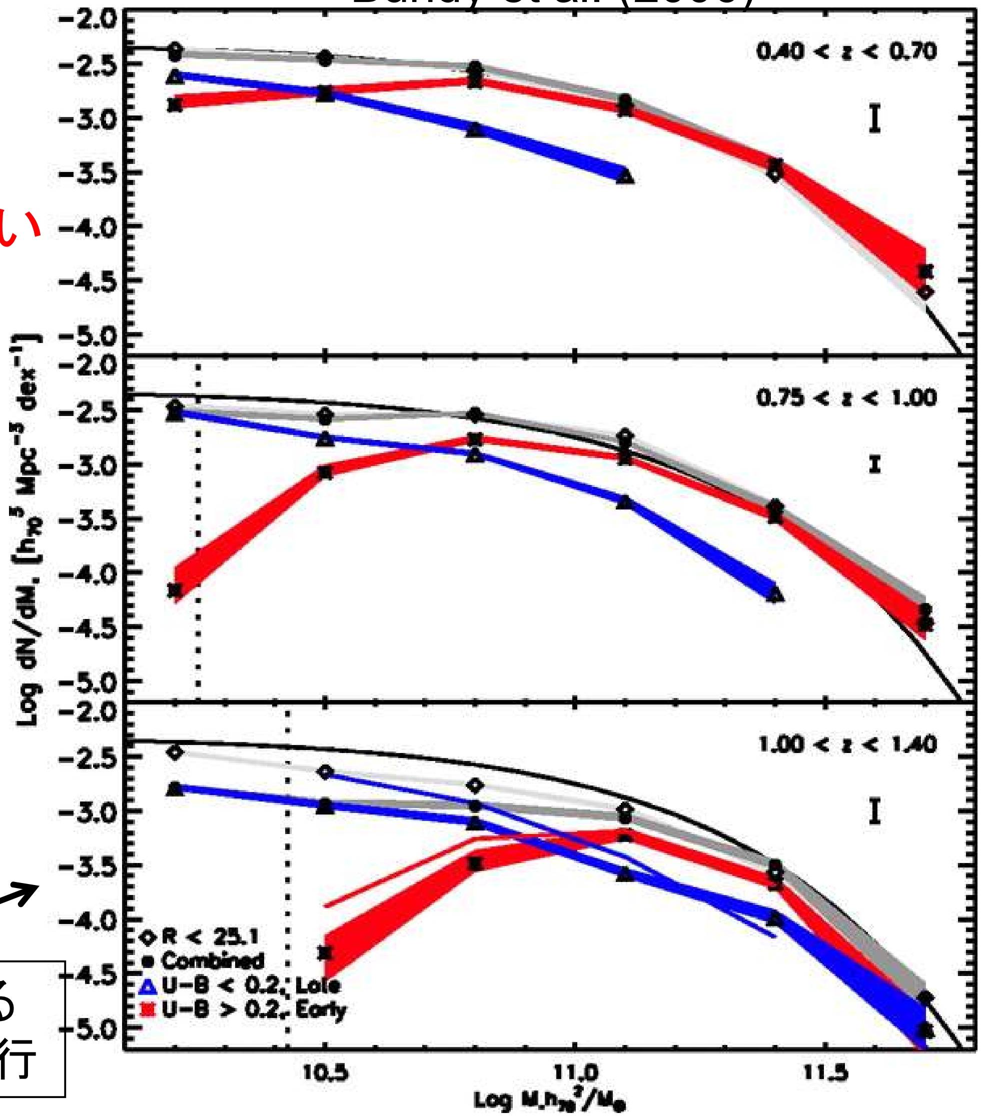

赤い銀河と青い銀河の切り替わる
質量が時間と共に低質量側へ移行

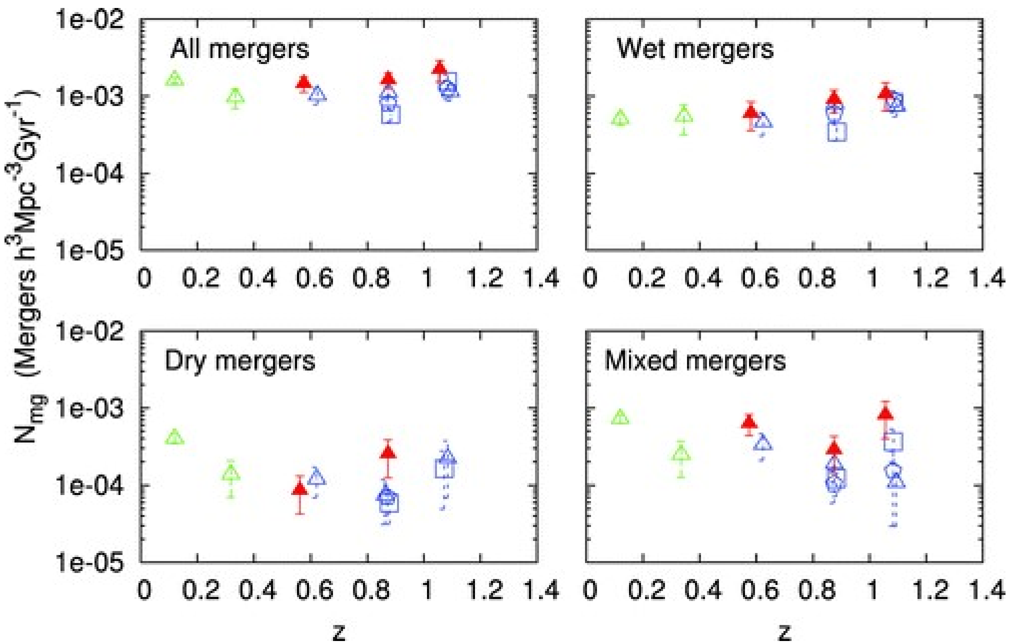

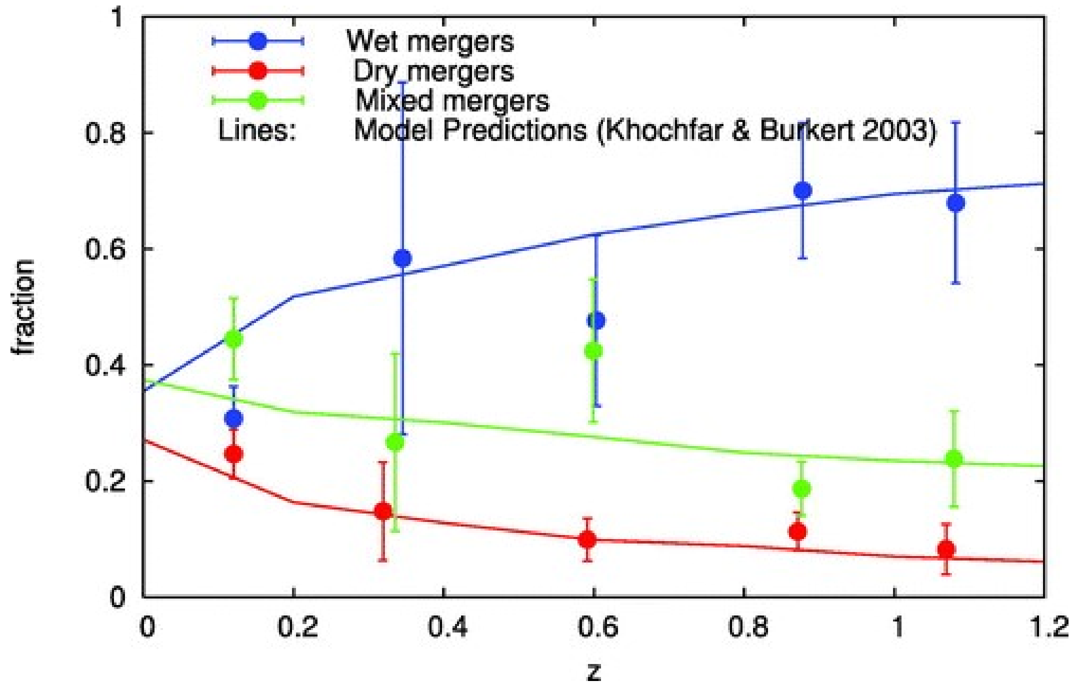

観測から求めた
銀河合体の割合
Lin et al. (2008)

高赤方偏移銀河の回転運動

z=2.38にある若い円盤銀河のHα線観測　Genzel et al. (2006)

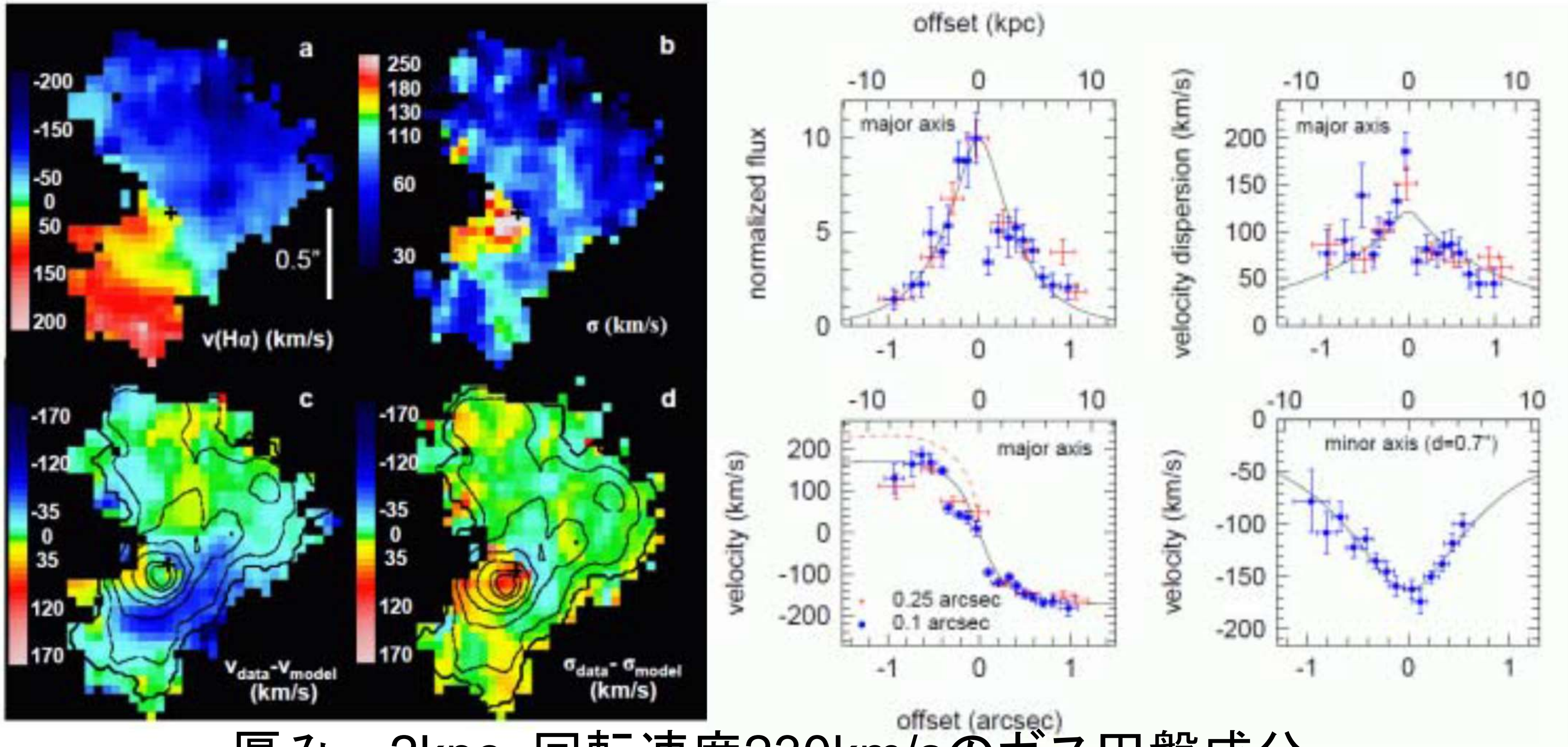

厚み～2kpc, 回転速度230km/sのガス円盤成分

⇒厚い恒星円盤の形成？

冷たいガス流（cold stream）による銀河形成
Dekel et al. (2009)

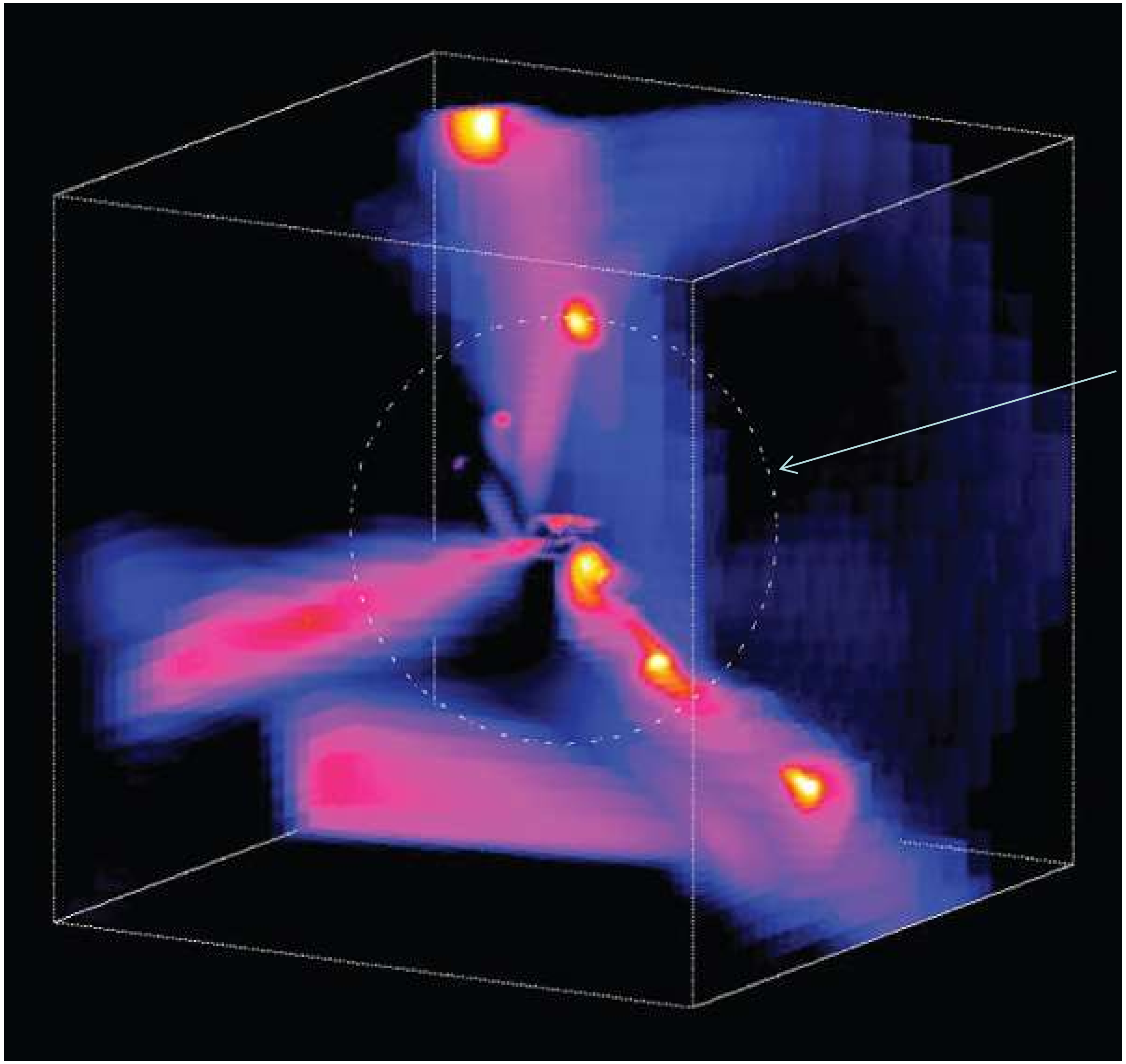

ダークハローの
ビリアル半径

Drop-out method for hunting high-z galaxies

Lyman-break technique

（星形成）銀河に含まれる
豊富な中性水素により
λ < 912 (1+z) Å
の光が遮断

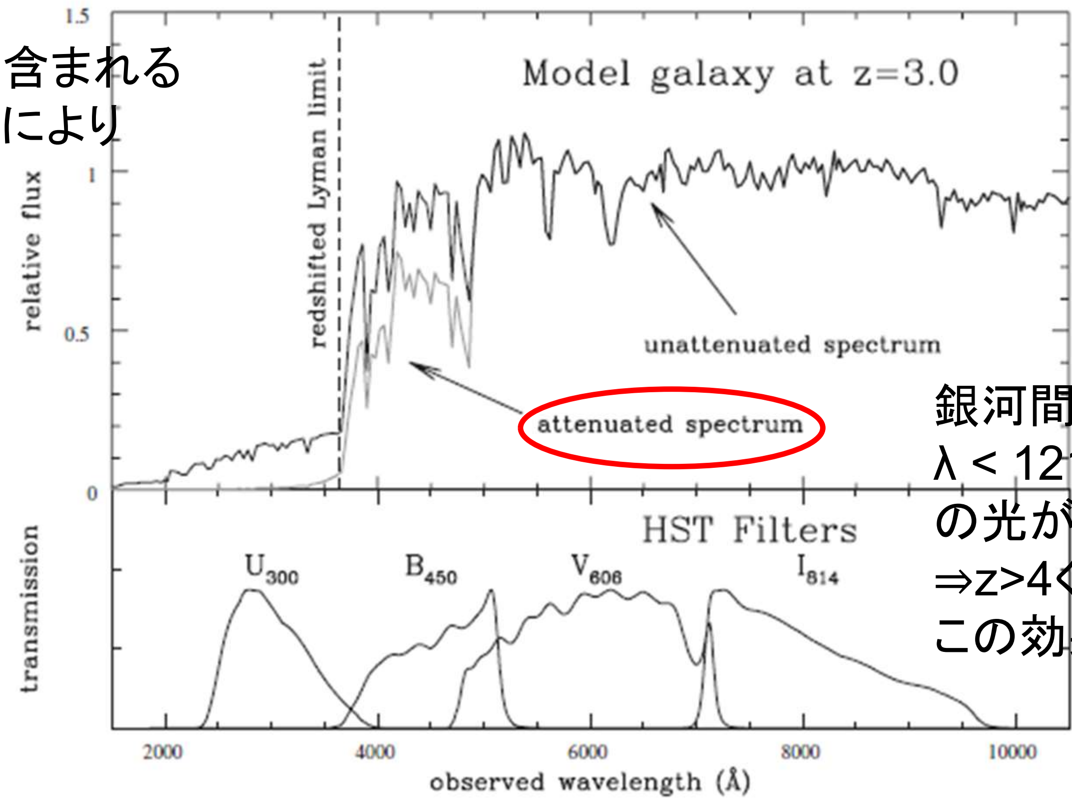

銀河間ガスの存在により
λ < 1216 (1+z) Å
の光が吸収されて弱くなる
⇒z>4ぐらいになると、
この効果が支配的

Fig. 2.34. An illustration of how the ‘Lyman-break’ or ‘drop-out’ technique can be used to select star-forming galaxies at redshifts $z \sim 3$. The spectrum of a typical star-forming galaxy has a break at the Lyman limit (912 Å), which is redshifted to a wavelength $\lambda \sim 4000$ Å if the galaxy is at $z \sim 3$. As a result, the galaxy appears very faint (or may even be undetectable) in the U band, but bright in the redder bands. [Courtesy of M. Dickinson; see Dickinson (1998)]

Lyman-α forest

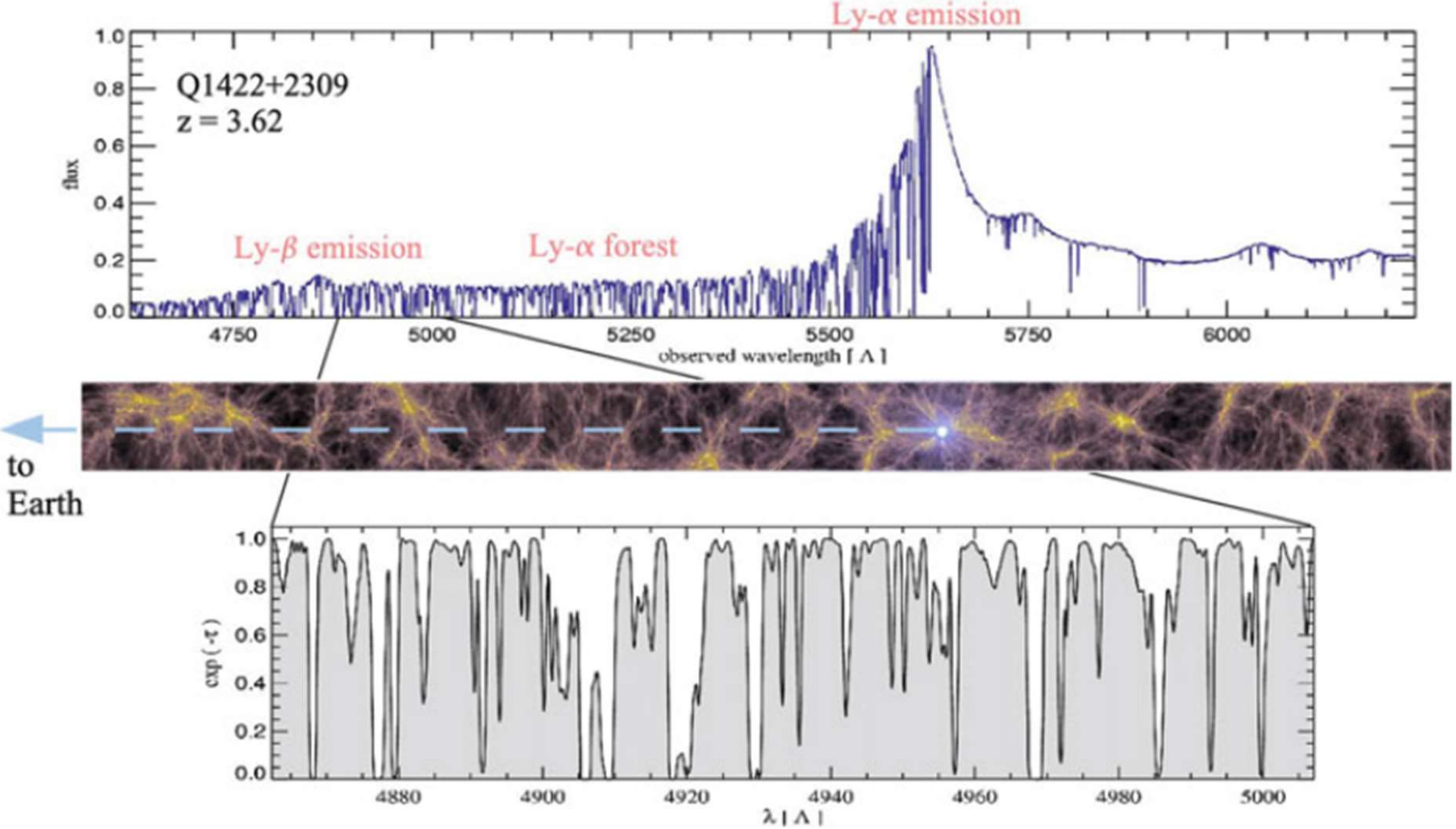

銀河間にある中性水素を含む雲の存在により、λ = 1216 Åの光が吸収

Recent JWST results on z~10 galaxies

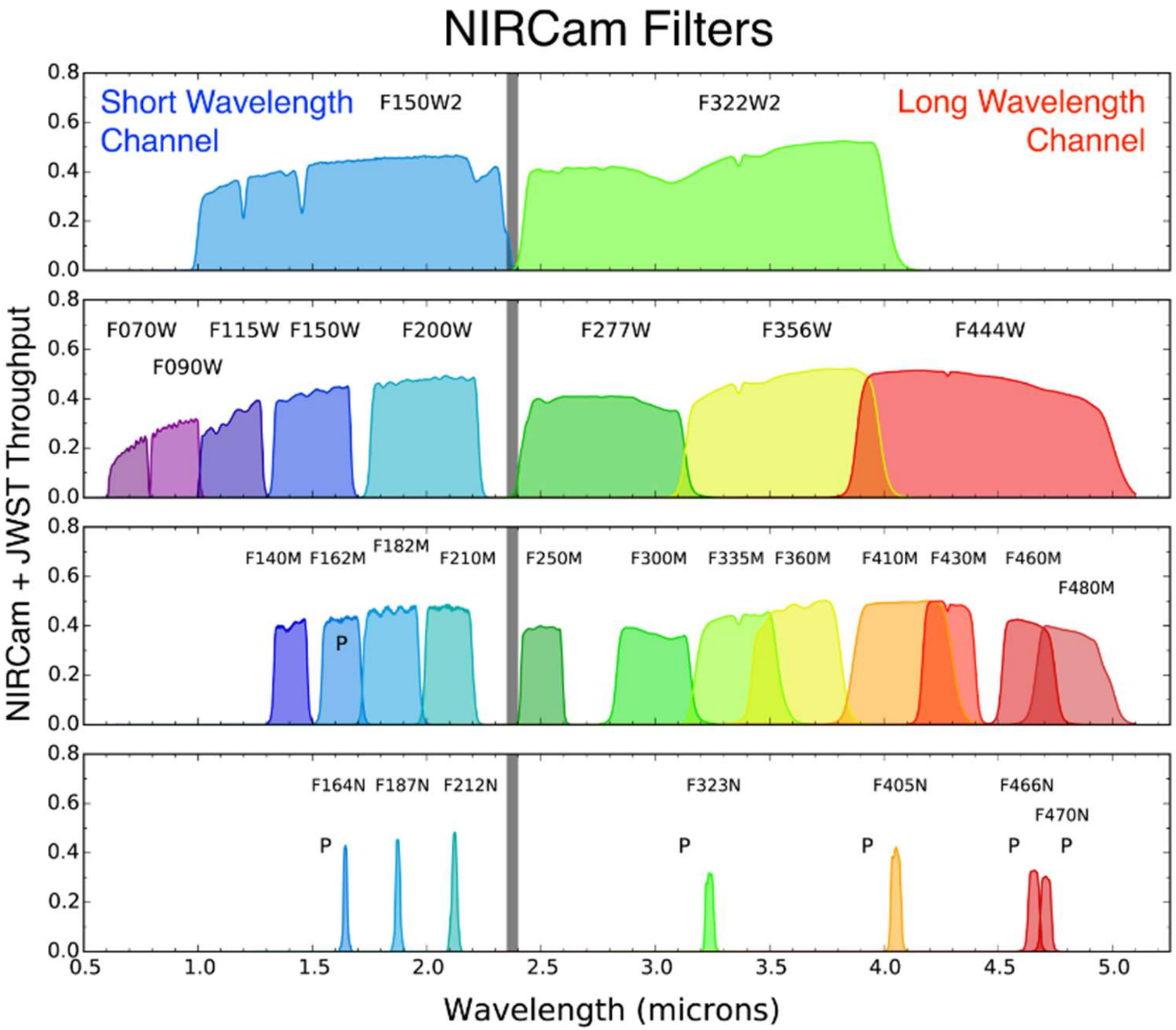

Labbe+ 2022: Discovery of M* > 10^10 Msun galaxies at 7<z<11 (two with >10^11Msun)

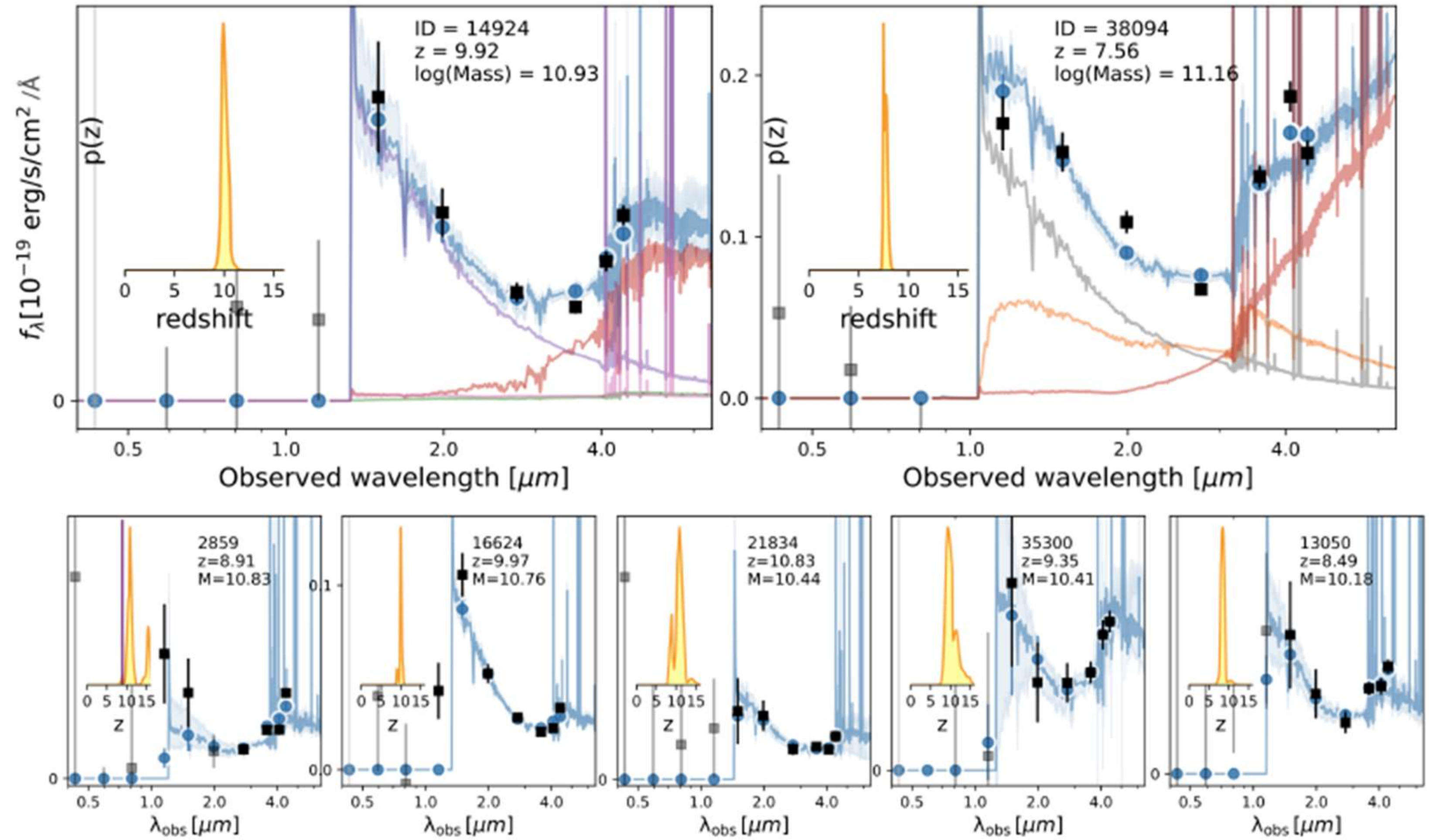

Figure 3: Spectral energy distributions (SEDs) and photometric redshift probability distributions $P(z)$ of the 7 galaxies with $\log(M_*/\mathrm{M}_\odot) > 10.0$. The flux density units are in $F\lambda$ versus wavelength in μm. All galaxies show characteristic V-shaped SEDs, with a clear upturn at $3-4\,\mu$m and a double break. The redshifts are well-constrained owing to the presence of two breaks. The two most massive galaxies are highlighted on the top row. Shown are the contribution of each template in the fit, where the fit produces a prominent contribution of an older stellar population (left) or dusty stellar population (right) shown in red. Emission lines clearly contribute to the F356W and F444W bands, but the emission-line sensitive F410M medium band providing a powerful diagnostic, improving both the redshift and the SED fit. The two brightest, most massive galaxies (top panels) were previously detected with $Hubble$, but misidentified as low mass galaxies at $z\sim 1$.[23]

z~16 galaxies? (Atek et al. 2022)

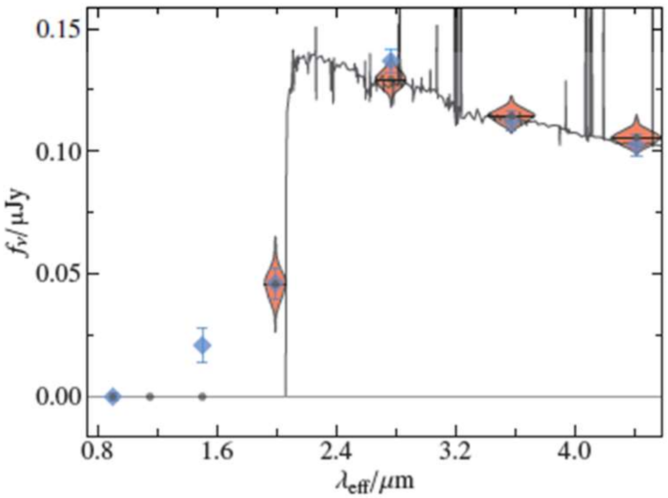

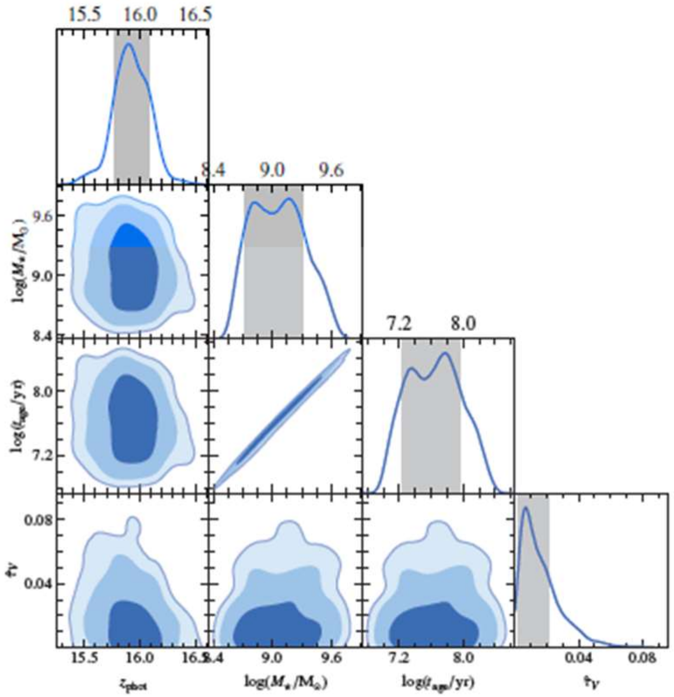

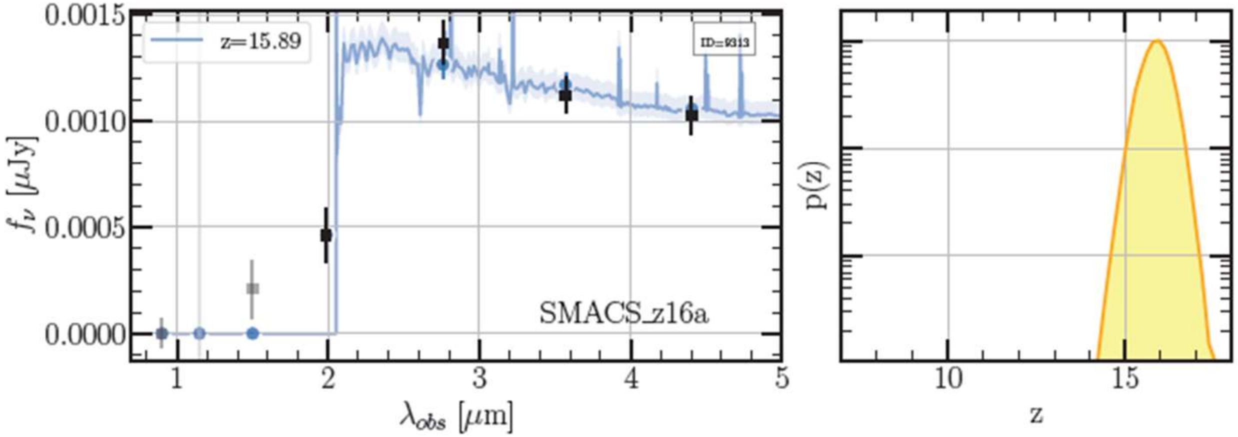

Figure 7. Best-fit solution for the SED and photometric redshift of SMACS_z16a. **Upper row:** Best-fit SED using the BEAGLE code. *Left:* Best-fit SED (black solid curve) with the observed photometric data (blue points) and expected model photometric points (black points) and associated uncertainties (pink areas). *Right:* Triangle plot of the posterior probability distribution of the four fitted galaxy parameters: redshift, stellar mass, stellar age and attenuation. **Bottom row:** Best-fit SED using the EAZY code. *Left panel:* The best-fit SED over-plotted over the observed flux densities (in dark squares). Model flux densities are shown in blue circles. The Lyman-break of the SED of this galaxy is estimated at z = 15.88 and the redshift probability distribution function is shown in the *right* panel. Both codes agree on a high-redshift solution with a relatively narrow posterior distribution and which does not show a secondary peak at lower redshift.

Boylan-Kolchin 2023

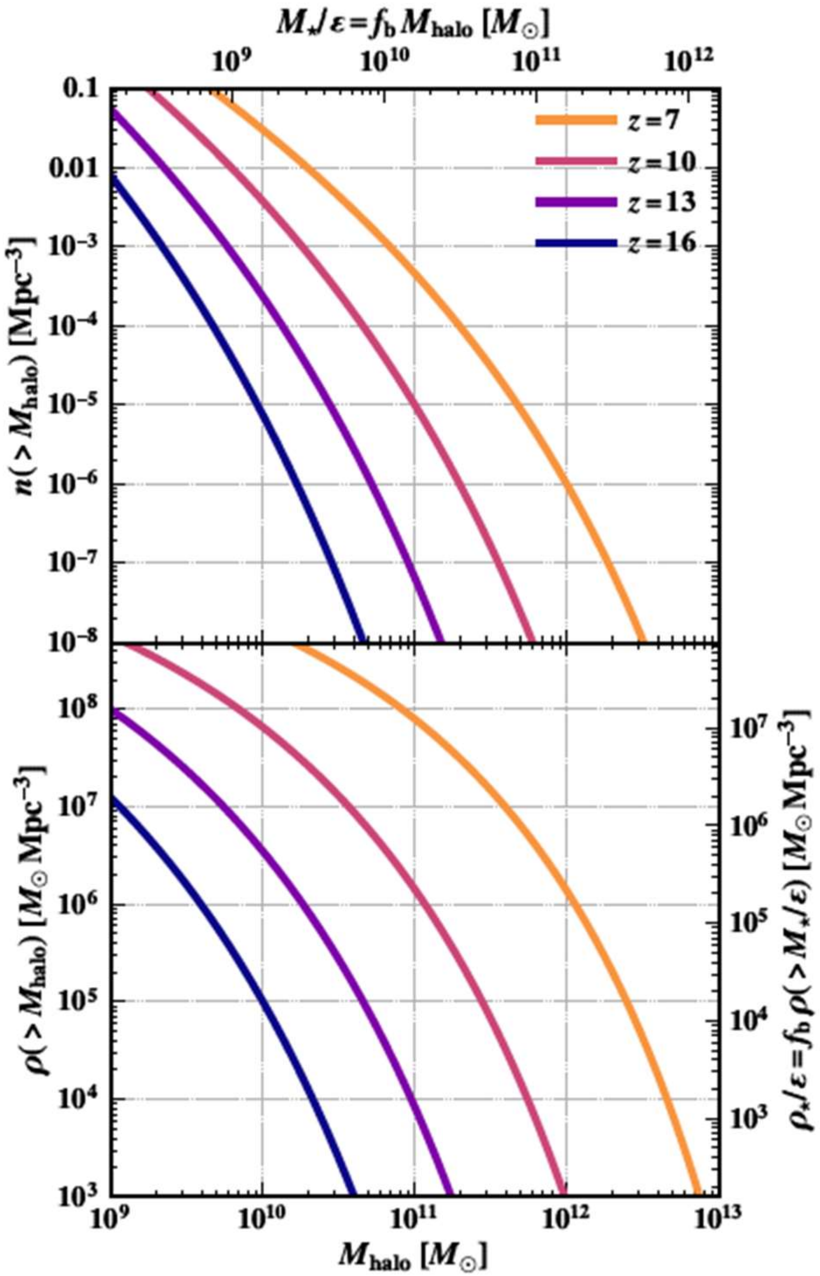

Dark Matter Power Spectrum

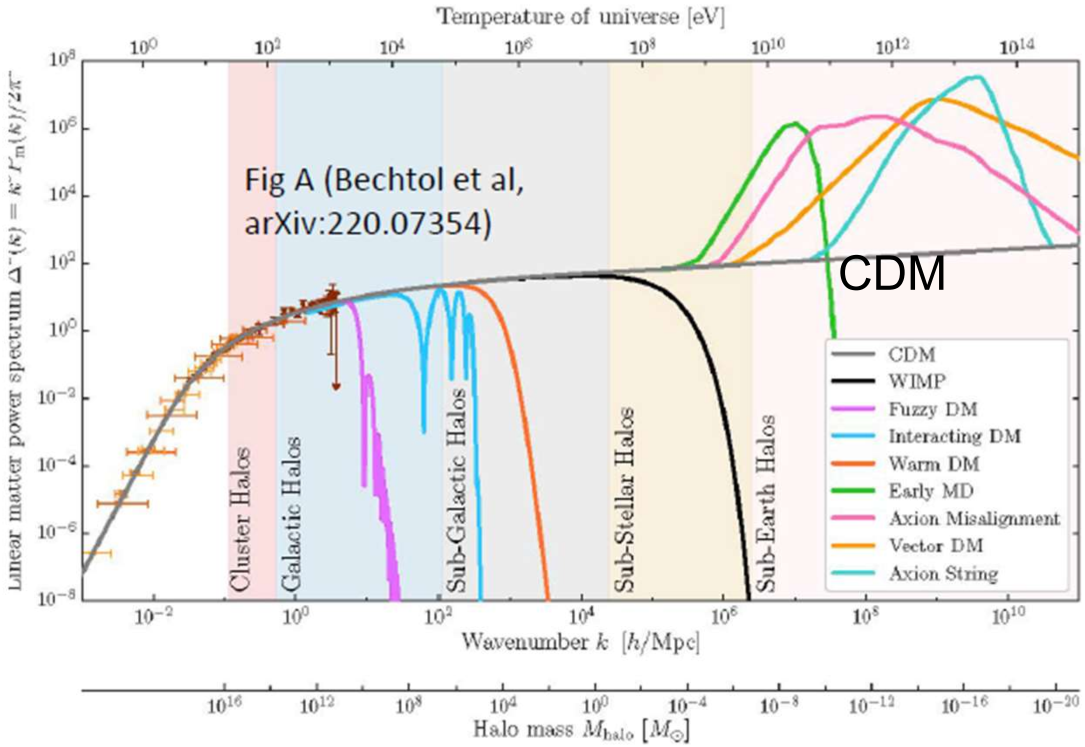

Figure 1. The cumulative comoving number density (top) and mass density (bottom) of halos more massive than M_{halo} at various redshifts. The secondary x-axis (top) shows the maximal stellar mass given M_{halo}, $M_{\star,max} = f_b M_{halo}$, while the secondary y-axis on the bottom plot shows the upper limit to the comoving stellar mass density contained in galaxies more massive than $M_{\star,max}$. Galaxies, or populations of galaxies, at a given redshift must lie below the curves for that redshift in both the upper and lower plots, modulo observational errors and sample variance considerations, in ΛCDM. Detection of a galaxy or population of galaxies at redshift z lying above the curve corresponding to that redshift in either panel indicates potential tension with ΛCDM predictions.

Boylan-Kolchin 2023

Presence of high M* galaxies at z=7~10 is in tension with ΛCDM theory

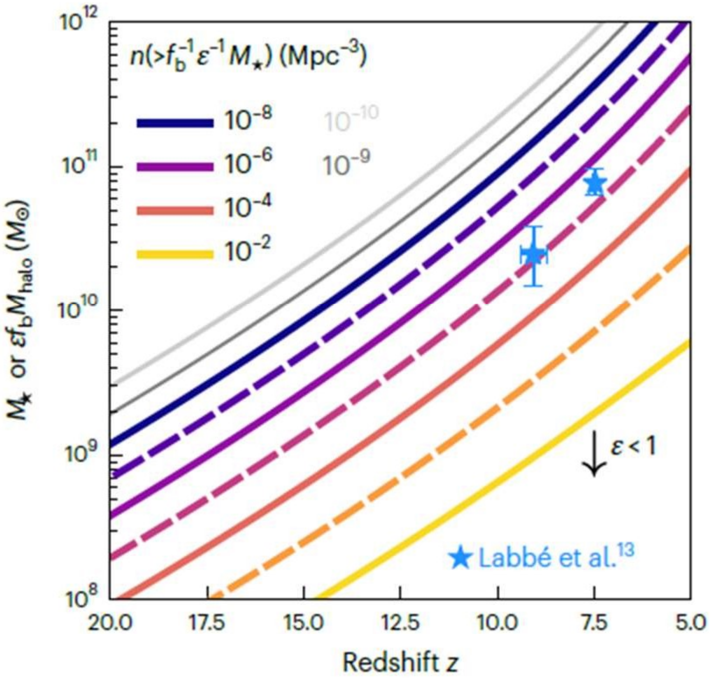

1 | **Limits on the abundance of galaxies as a function of redshift.** Curves
w the relationship between $M_\star$ and z at fixed cumulative halo abundance (left)
fixed ρ_b ($>M_{halo}$), or equivalently fixed peak height ν (right). The most extreme
galaxy candidates are shown as blue stars, with uncertainties indicating 68%
rvals (symmetric about the median) of the posterior probability distribution.
existence of a galaxy with $M_\star$ at redshift z requires that such galaxies have a
ulative co-moving number density that is, at most, the number density shown
e left panel, as those galaxies must reside in host halo of mass $M_{halo} = M_\star/(f_b\varepsilon)$.

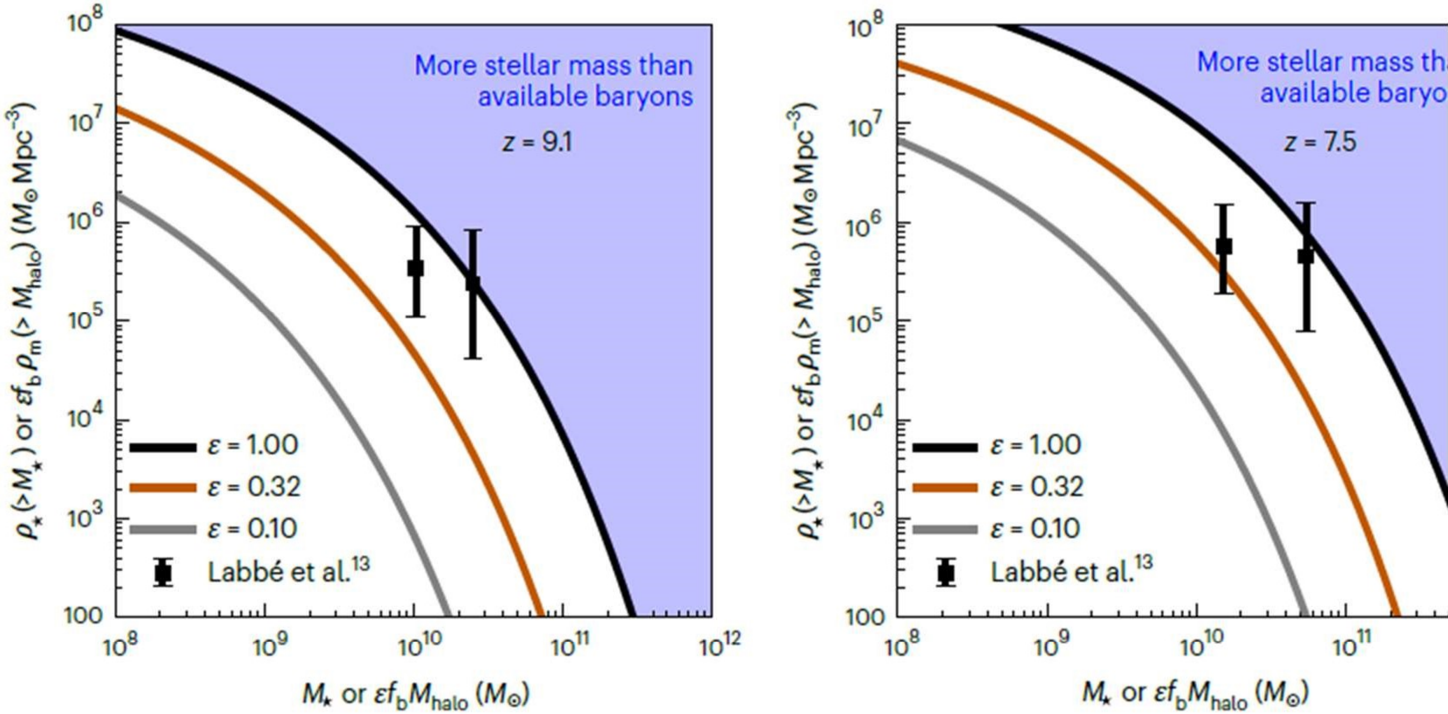

Fig. 2 | Stellar mass density limits. The co-moving stellar mass density contained within galaxies more massive than $M_\star$ at $z \approx 9.1$ (left) and $z \approx 7.5$ (right) for three values of the assumed conversion efficiency ε of a halo's cosmic allotment of baryons into stars. Only if all available baryons in all haloes with enough baryons to form the galaxies reported by L23 have indeed been converted into stars by that point—an unrealistic limit—is it possible to produce the stellar mass density in the highest $M_\star$ bin at $z \approx 9$ measured by L23 in a

typical volume of a ΛCDM Universe with the Planck 2020 cosmology
are similar at $z \approx 7.5$. For more realistic values of ε, the required baryo
is substantially larger than the theoretical maximum in this cosmolo
considering 1 σ shot noise and sample variance errors added in quad
(which comprise the uncertainties on the L23 data points in each pa
measurements are consistent with the base ΛCDM model if $\varepsilon > 0.57$, v
still imply incredibly efficient star formation in the high-redshift Uni

Harikane+2023
Large number of UV-bright galaxies at z=12~16

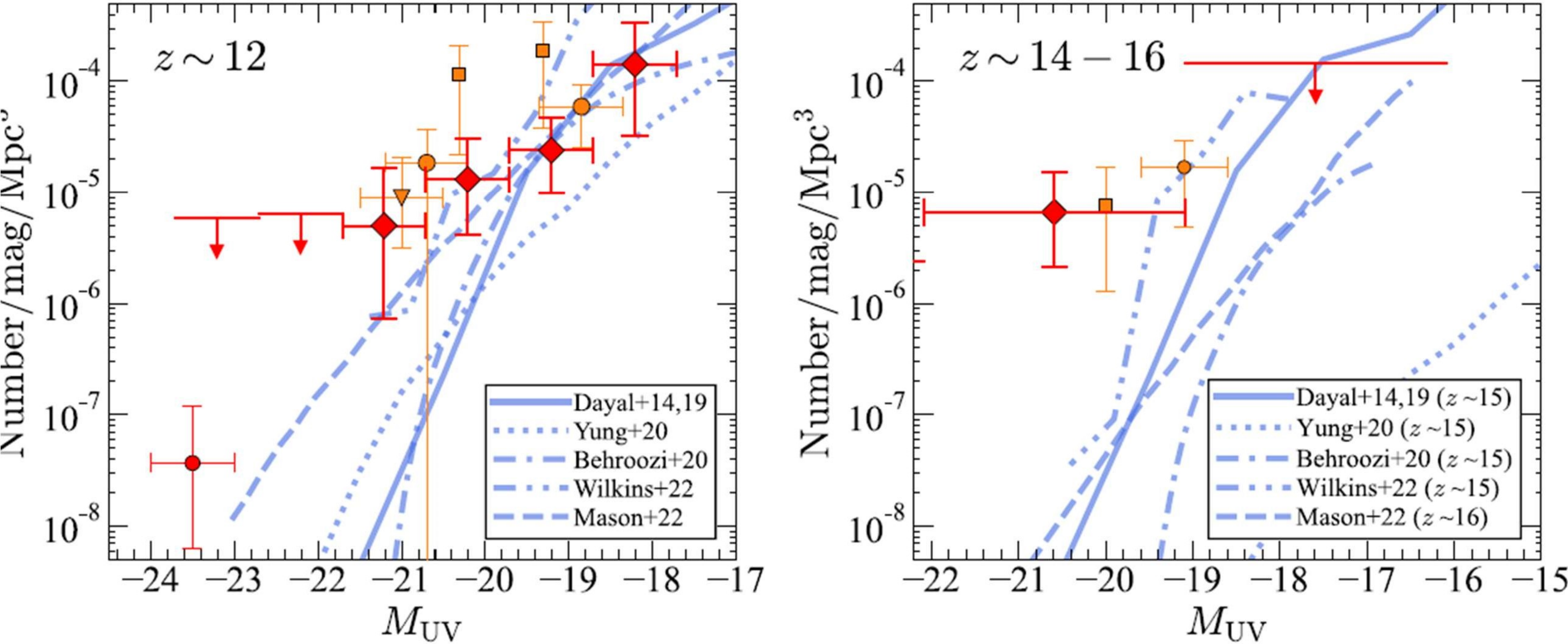

re 16. Comparison of the luminosity function measurements with theoretical predictions and the empirical models at $z \sim 12$ (left) and $z \sim 16$ (right). The show the theoretical and empirical models obtained by Dayal et al. (2014, 2019; solid line), Yung et al. (2020; dotted line), Behroozi et al. (2020; dotted–d Wilkins et al. (2023; double-dotted–dashed line), and Mason et al. (2023, their no dust model; dashed line). The red and orange symbols show observa s in the same manner as Figures 12 and 13. The red diamonds and arrows represent the measurements and upper limits obtained by this study. The orange c ed circle, the down-pointing orange triangle, and the orange square in the left (right) panel indicate the number densities reported by Donnan et al. (ane et al. (2022a), Naidu et al. (2022b), and Bouwens et al. (2022b) and Finkelstein et al. (2022b), respectively.

Harikane+2023
Large number of UV-bright galaxies
at z=12~16

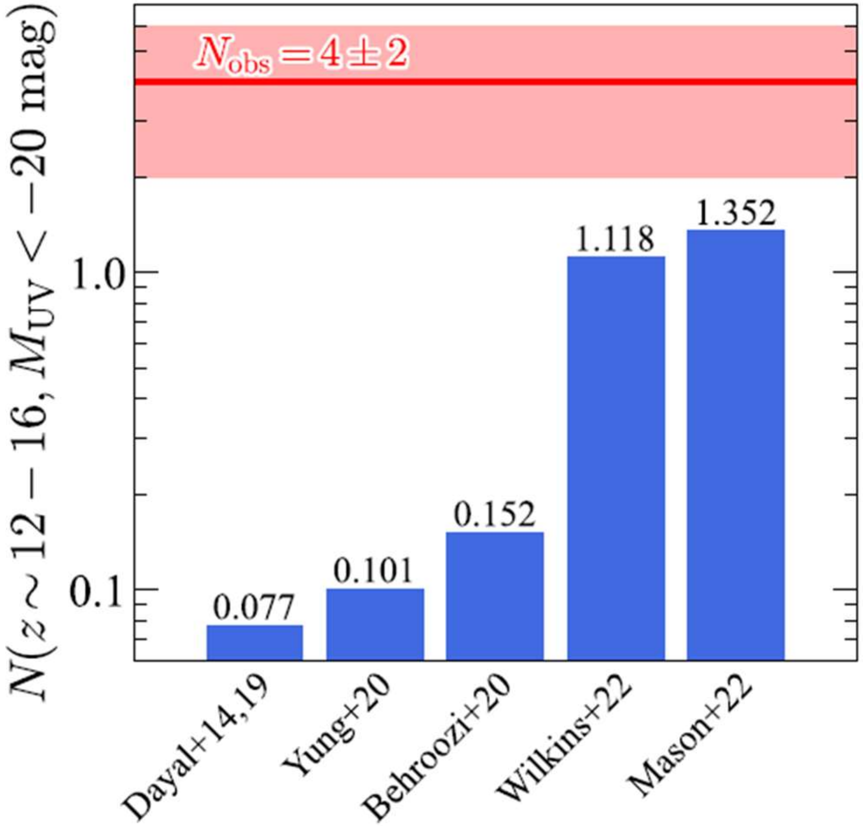

Figure 17. Theoretical predictions for the number of bright galaxies at $z \sim 12$–16 with $M_{UV} < -20$ mag detected in our survey area of ~ 90 arcmin^2. These numbers are based on the theoretical models of Dayal et al. (2014, 2019), Yung et al. (2020), Behroozi et al. (2020), Wilkins et al. (2023), and Mason et al. (2023). The red horizontal line with the shaded region indicates the number of observed galaxies at $z \sim 12$–16 with $M_{UV} < -20$ mag ($N_{obs} = 4 \pm 2$), which is higher than these model predictions.

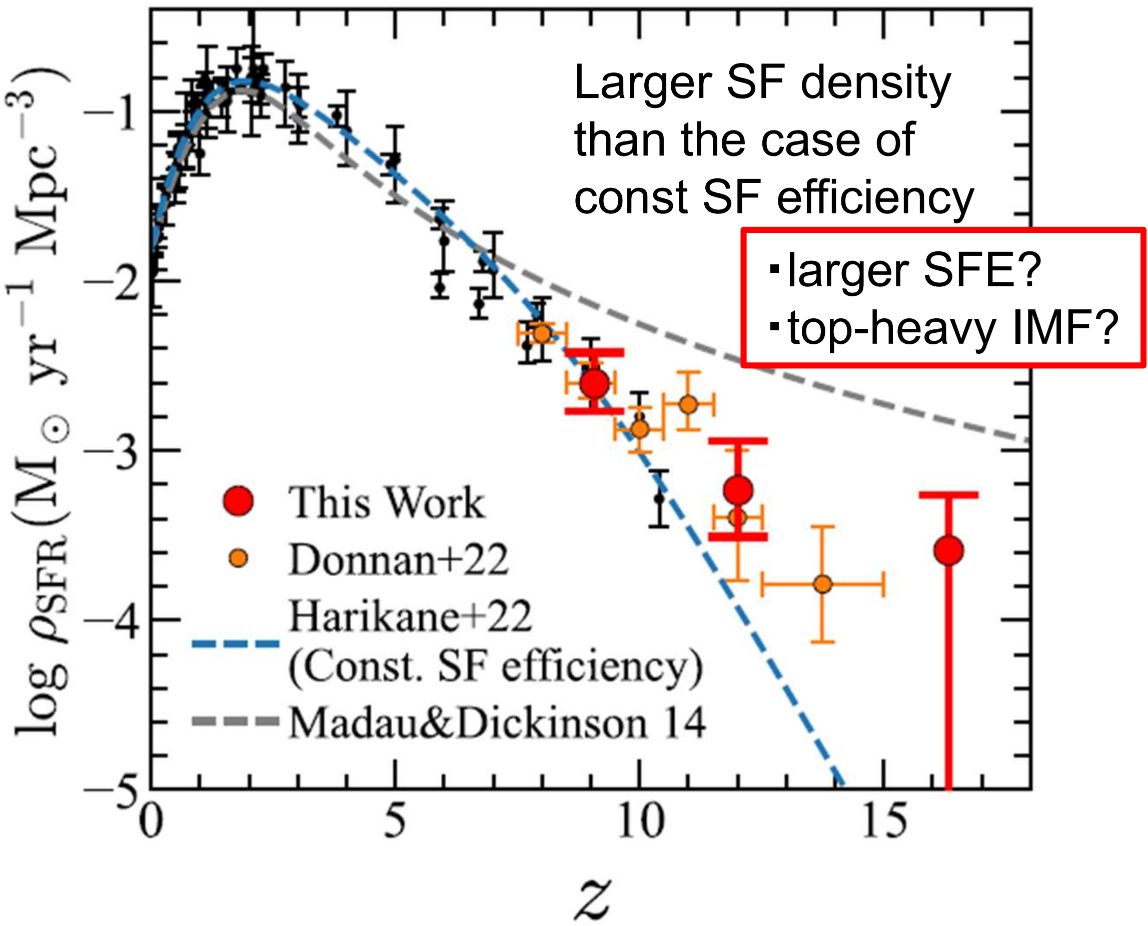

Figure 18. Cosmic SFR density evolution. The red circles represent the cosmic SFR densities obtained by our study, with the double-power-law luminosity functions integrated down to $M_{UV} = -17$ mag. The black circles indicate the cosmic SFR densities derived by Madau & Dickinson (2014), Finkelstein et al. (2015a), McLeod et al. (2016), Bhatawdekar et al. (2019), and Bouwens et al. (2020). The orange circles are results by Donnan et al. (2023). The blue dashed curve is the best-fit function of the cosmic SFR densities in Harikane et al. (2022b, their Equation (60)). In Harikane et al. (2022b), they assume a constant star formation efficiency at $z > 10$, resulting in the power-law decline with $\rho_{SFR} \propto 10^{-0.5(1+z)}$. The gray dashed curve shows the best-fit function at $z \lesssim 8$ determined by Madau & Dickinson (2014) extrapolated to $z > 8$. All results are converted to those of the Salpeter (1955) IMF.